Short-Focus Lens Design for Terahertz Ray

Keita Miyazawa[1*], Atsushi Kanno[2], Shingo Saito[2], Keizo Inagaki[2,1], Tetsuya Kawanishi[1,2]
[1]Waseda University, Tokyo,169-8555, Japan
[2]National Institute of Information and Communications Technology, Tokyo, 184-8795, Japan
[*]Email: keita.m@toki.waseda.jp

Abstract – Polyethylene and polypropylene, which have high transmittance in the terahertz band, are commonly used for terahertz lens systems. However, it is rather difficult to provide small lens systems, because the refractive indexes of polyethylene and polypropylene are small. In this research, we designed a small terahertz lens system by using a thin lens with a high-refractive index material, in addition to polyethylene or polypropylene.

Keywords – Terahertz Time Domain Spectroscopy; thin lens; lens design; sapphire; polypropylene

1. Introduction

Compact lens systems for terahertz array sensors are desired for high resolution imaging [1]. Polyethylene (PE) and polypropylene (PP) are known to have very high transmittance in the terahertz band and are used as lens materials for terahertz system. However, since the refractive index is low, it is difficult to miniaturize the optical system using only PE and PP. In general, the refractive index of optical materials such as germanium and sapphire used in the infrared communication band is higher than that of PE, but there is a problem that the transmittance in the terahertz band is low. In this research, a compact doublet lens with high transmittance and high refractive index in the terahertz band is designed by combining a thick lens using PP and PE with a thin lens using germanium, sapphire, etc.

2. THz condenser lens design

Figs. 1 and 2 shows the refractive indices and transmittance of samples (details are shown in Table 1), measured using terahertz time domain spectroscopy (TDS). The dispersion of each material is small in the terahertz band, and a terahertz system is less affected by the chromatic aberration. From the viewpoint of the reliability of the measurement data, we used the data in the frequency region of 0.5 to 2 THz to design terahertz lens systems.

To provide a compact condenser lens, we designed doublet lens systems with the materials shown in Table 1, by using the CODE V optical system design software. Geometrical optical analysis was used to estimate which combination of materials is effective. The lens parameters are optimized to achieve the minimum root-mean-square (RMS) of the spot diameter, where the parameters shown in Table 2 is fixed to design a compact lens system. The material for the lens 1 is PE or PP. The thickness of the lens 2 is much smaller than that of the lens 1, to reduce the total insertion loss of the lens systems.

The RMS spot diameters for various lens materials are shown in Table 3. We also approximately estimated the average transmittances of the lens systems, by using the measured transmittance shown in Fig. 2, where the incident light was assumed to be parallel ray, and the beam diameter was set to 30 mm. Table 4 shows he estimated average loss for the frequency region of 0.5 to 2 THz.

Table 1. Material list measured by THz-TDS.

Material	Abbr.	t [mm]
polyethylene	PE	1.010
polypropylene	PP	1.038
silica	SiO_2	3.015
calcium fluoride	CaF_2	2.041
Sapphire	Sap	2.038
Silicon	Si	3.011
Germanium	Ge	3.009

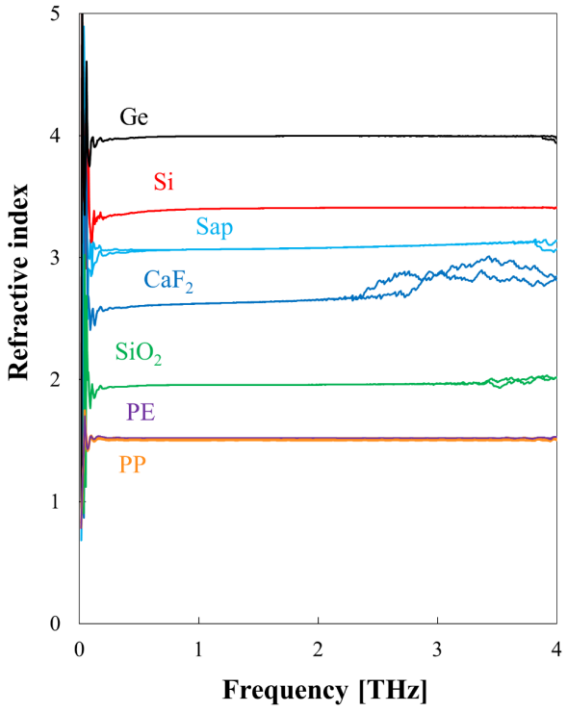

Figure 1. Frequency characteristics of refractive index.

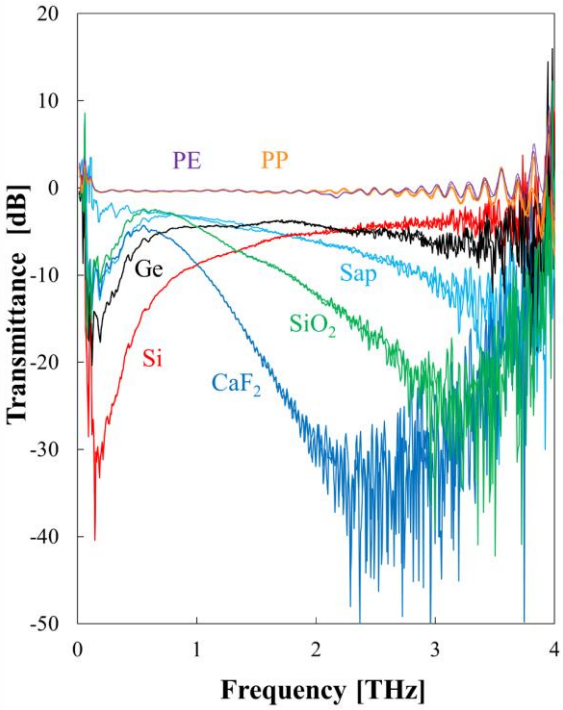

Figure 2. Frequency characteristics of transmittance.

Table 2. Fixed design parameters of the THz lens.

Items	Value [mm]
center thickness of lens 1	20
center thickness of lens 2	3
back focus	20
beam diameter	30

3. Analysis of designed lens systems

As shown in Table 3, the RMS spot diameter can be reduced by using combination of various materials. On the other hand, the loss would be larger than in the conventional lens systems with PE or PP, due to the small transmittance in the materials. We roughly estimated the peak power of the terahertz wave in the focused spots by using a figure of merit defined by $(T/T_0)(R_0/R)^2$. T/T_0 and R/R_0 are the transmittance and RMS spot diameter of a doublet lens system, normalized by those in the reference lens system, consisting of PP (lens 1) and PE (lens 2). R_0 and T_0 are shown in the first rows in Tables 3 and 4. As shown in Fig. 3, the doublet with PP and sapphire (PP-Sap) would provide the largest peak power at the center of the spot, while the total insertion loss of the lens system is larger than in the reference lens system (PP-PE). Figs. 4 and 5 show configurations of the lens systems. The thickness of the lens 2 is set to be much smaller than that of the lens 1 to suppress the loss in sapphire. Point spread functions (PSF) are shown in Figs. 6 and 7, where the 3-dB diameters for PP-PE and PP-Sap are 0.28mm and 0.23mm, respectively.

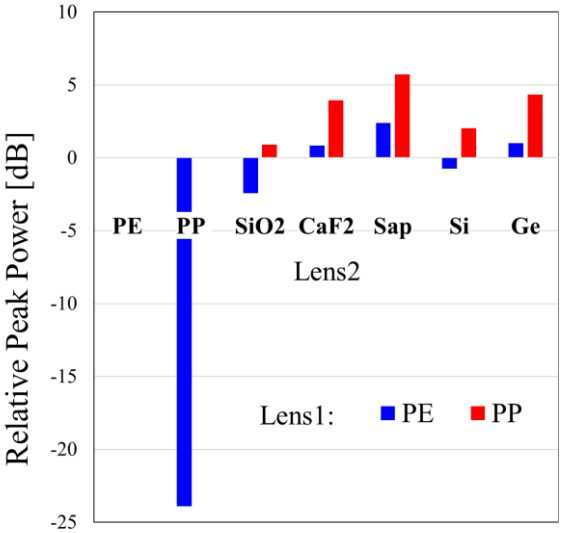

Figure 3. Peak power for various lens material.

Table 3. RMS spot diameter for various lens materials.

lens2 \ lens1	PE	PP
PE	–	1.0046
PP	10.5964	–
SiO_2	0.5544	0.5475
CaF_2	0.1656	0.1648
Sap	0.2872	0.2867
Si	0.2237	0.2506
Ge	0.4052	0.4120

Table 4. Average loss in dB for various lens materials at optimum design.

lens2 \ lens1	PE	PP
PE	–	4.92
PP	8.37	–
SiO_2	12.51	9.30
CaF_2	19.75	16.69
Sap	13.42	10.10
Si	18.70	14.96
Ge	11.80	8.32

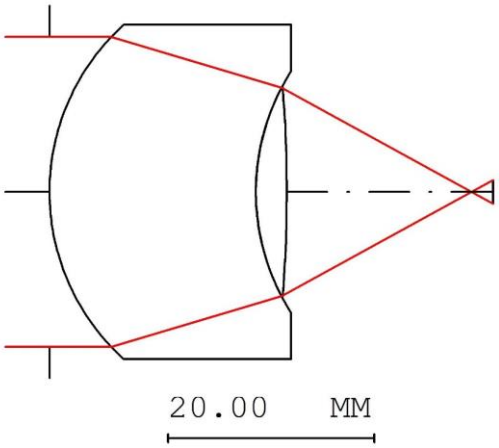

Figure 4. Doublet Lens for THz band. lens1: PP, lens2: PE

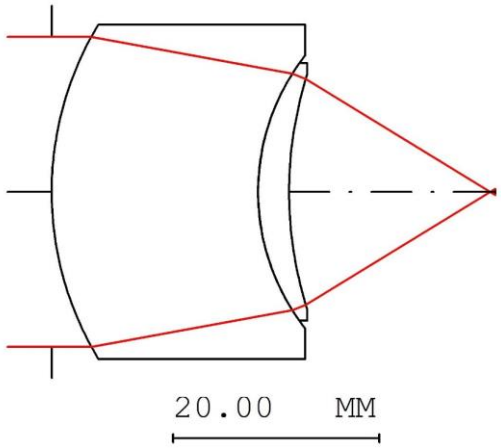

Figure 5. Doublet Lens for THz band. lens1: PP, lens2: Sapphire

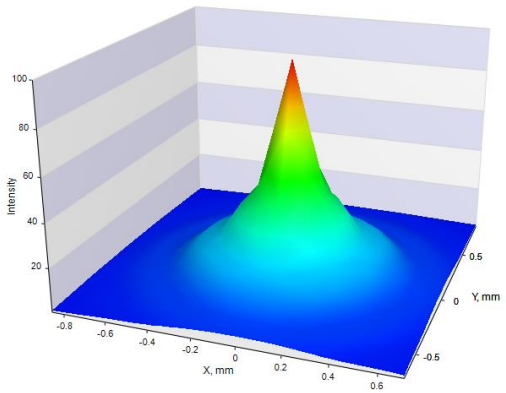

Figure 6. The point spread function. lens1: PP, lens2: PE

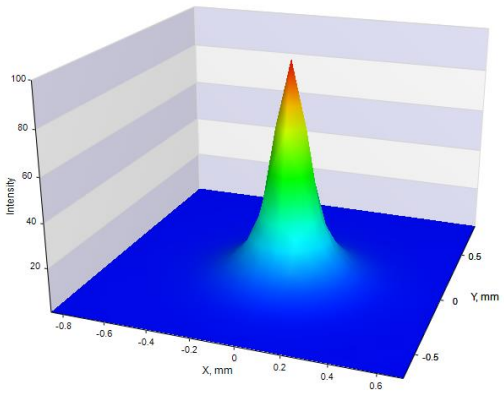

Figure 7. Point spread function. lens1: PP, lens2: Sapphire

4. Conclusion

Doublet terahertz lens systems are designed by using measured transmittance and refractive index of various materials. The material dispersion is small enough in the terahertz band, to design lens systems for wideband operation.

By combining a thick lens using low refractive index and high transmittance material and a thin lens using high refractive and low transmittance material, the compact optical system for the terahertz band could be designed, where the peak terahertz power would be enhanced.

Acknowledgment

This paper includes research results from works funded by Horizon 2020, the European Union's Framework Program for Research and Innovation, under grant agreement No. 814523, and by the Commissioned Research (No. 196) of National Institute of Information and Communications Technology (NICT), Japan. This work was also partially supported by Waseda Research Institute for Science and Engineering. The refractive index and transmittance data in terahertz band are measured with NICT advanced ICT device lab.

References

[1] Georgios C.Trichopoulos, H.Lee Mosbacker, Don Burdette, Kubilay Sertel. A Broadband Focal Plane Array Camera for Real-time THz Imaging Applications. IEEE Transaction on Antennas and Propagation. 2013; 61(4): 1733-1740.

[2] Christian Jansen, Steffen Wietzke, Ole Peters, Maik Scheller, Nico Vieweg, Mohammed Salhi, Norman Krumbholz, Christian Jördens, Thomas Hochrein, and Martin Koch. Terahertz imaging: applications and perspectives. Applied Opttics. 2010; Vol.49, No.19, E48-E57.

[3] Atsushi Yamaguchi. Development of Terahertz Imaging Systems. Pioneer R&D. 2014; 1-7.

[4] Kiyomi Sakai, Masanori Hangyo. Terahertz Time Domain Spectroscopy and Imaging. レーザー研究. 2002; 376-384

[5] M Usami, T Iwamoto, R Fukasawa, M Tani, M Watanabe, K Sakai. Development of a THz spectroscopic imaging system. IPEM. 2002; 47 3749-3753

Evaluation of antenna radiation characteristics at terahertz frequency band based on an electrooptic near-field measurement

Yusuke Tanaka[1], Shintaro Hisatake[1*]
[1]Graduate School of Natural Science and Technology, Gifu University, 501-1193, Yanagido 1-1, Gifu, Japan
*Corresponding author: hisatake@gifu-u.ac.jp

Abstract – The near-field of a horn antenna at 288 GHz was measured based on the non-polarimetric EO frequency down conversion technique and self-heterodyne technique. The measured near-field was converted to the far-field and compared with the simulated characteristic to examine the fidelity of our results. The measured radiation characteristics roughly agreed with the simulated results.

Keywords – Terahertz; Antenna measurement; EO sensing; Near-field;

1. Introduction

In the terahertz (THz: 0.1 - 10 THz) band, many applications have been considered in these days such as wireless communication [1], non-destructive inspection [2], etc. In these applications, antennas are one of the important components to determine the system performance, therefore many antennas operating in the THz frequency band have been studied [3, 4]. In order to optimize the performance of the applications, it is necessary to accurately determine the antenna radiation pattern. However, the evaluation method has not been established in the THz wave band.

We have developed an electrooptic (EO) sensing system, which is based on a non-polarimetric frequency down conversion technique and self-heterodyne techniques, to reveal the spatial and temporal evolution of freely propagating continuous THz waves [5, 6]. This system enabled us to measure near-field of the THz wave radiated from the antenna.

In this paper, we visualize the near-field of the THz wave (288 GHz) and calculate the far-field radiation pattern from the measured near-field. We also compare the far-field with the simulated results and evaluate the quality of our measurement.

2. System configuration

Figure 1 shows the experimental set up for the antenna near-field measurement using an electrooptic (EO) probe. The size of the EO crystal is 1×1×1 mm^3. The frequencies of the LDs were set to be f_1 and f_2 and combined to generate a beat note at a frequency of 288 GHz (λ = 1.04 mm) for the RF signal. The optical beat signal was converted to the THz signal by uni-traveling-carrier photodiode (UTC-PD). The generated THz wave was emitted from a horn antenna. The optical

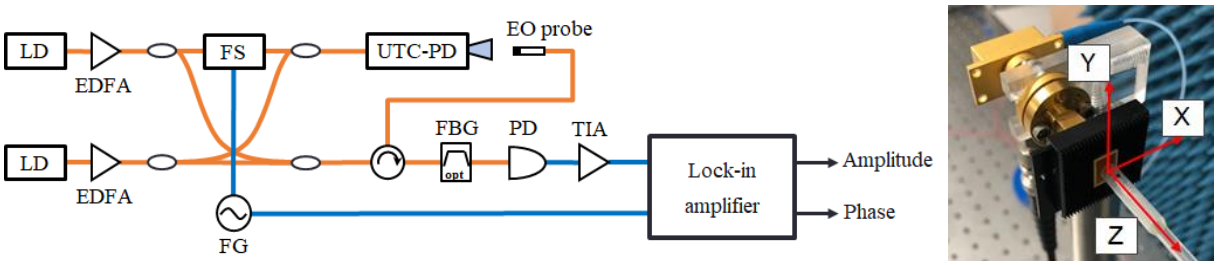

Figure 1. Experimental setup for the antenna near-field measurement. The system is based on a non-polarimetric EO frequency down conversion technique and self-heterodyne technique. UTC-PD: Uni-traveling-carrier photodiode, FS: frequency shifter, LD: laser diode, EDFA: Erbium doped optical fiber amplifier, TIA: transimpedance amplifier, FG: function generator, FGB: fiber bragg grating.

beat signal was also sent to the EO probe to sense the amplitude and phase of the THz wave. The EO probe was moved to map the near-field distribution on the antenna surface. As shown in Figure 1, the antenna was surrounded by an absorber.

3. Experimental result and discussion

Figure 3 shows the amplitude and phase distribution. The measured surface was at Z=2 mm from the antenna surface. The EO probe was moved by 0.1 mm pitch. The time constant of the lock-in detection was 30 ms. The maximum signal-to-ratio (SNR) was about 37 dB at the center of the surface.

Figure 4 shows the far-field patterns. The simulation was conducted using CST studio suite. The measured near-field was converted to the far-field. Measured far-fields roughly agreed with the simulated results. However, the measured results have asymmetric pattern in both of E-plane and H-plane. Also, the position of the sidelobes did not coincide with the simulated values.

Table 1 summarizes the radiation pattern characteristics. The deviation between the simulated and measured values for the 3-dB beam width were 0.3 deg. and 0.7 deg. for the H-plane and E-plane, respectively. The deviation for the sidelobe position was about 1 deg. and 2.5 deg. for the first and second sidelobe in the E-plane, respectively. We believe that those discrepancies were due to the EO probe characteristics. It is presumed that the characteristics of the probe are determined by the size of the EO crystal with respect to the wavelength. The sensitivity characteristics also depend on the incident direction of the signal to the EO crystal. The probe correction should be conducted to improve the measurement accuracy.

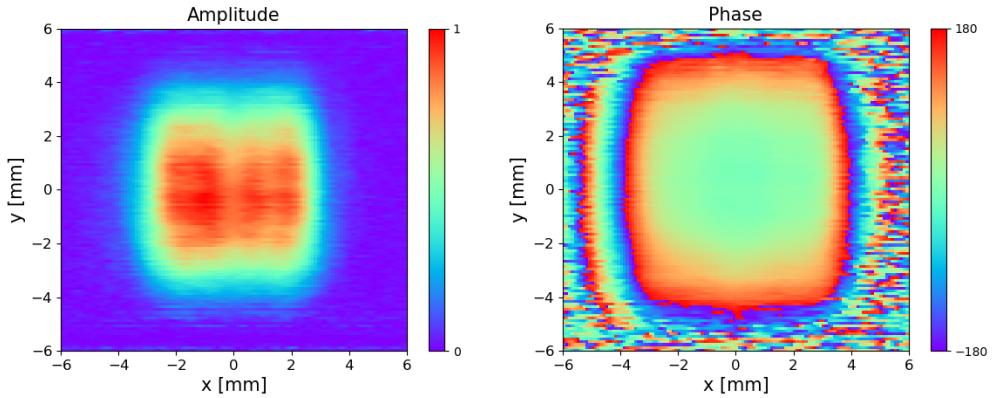

Figure 3. The measured amplitude and phase distribution. The amplitude is normalized to the maximum value.

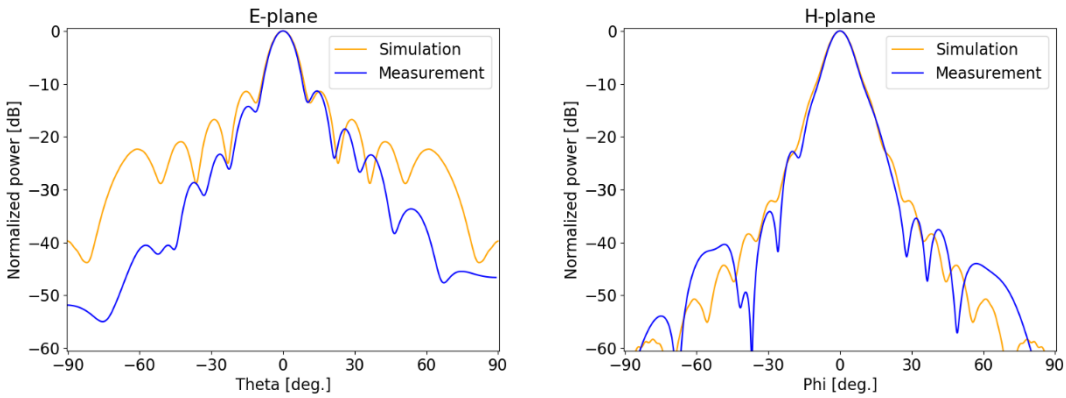

Figure 4. Measured and simulated far-field pattern. The measured near-field was converted to the far-field.

Table 1. Characteristics of the radiation pattern.

			Measurement	Simulation
H-plane 3dB beam width [deg.]			9.4	9.7
E-plane 3dB beam width [deg.]			9.5	10.2
E-plane	$+1^{st}$ sidelobe	Position [deg.]	14.22	15.42
		Main lobe ratio [dB]	-11.36	-11.43
	-1^{st} sidelobe	Position [deg.]	-14.55	-15.42
		Main lobe ratio [dB]	-14.28	-11.43
	$+2^{nd}$ sidelobe	Position [deg.]	25.94	28.76
		Main lobe ratio [dB]	-18.54	-16.74
	-2^{nd} sidelobe	Position [deg.]	-26.41	-28.76
		Main lobe ratio [dB]	-23.30	-16.74

4. Conclusion

We demonstrated far-field characterization of a horn antenna in the THz frequency band based on the near-field EO sensing. The measured radiation characteristics roughly agreed with the simulated results. Small discrepancy between the measurement and the simulation is due to the probe characteristics at this frequency band. The probe correction may be conducted to improve the fidelity of the measurements.

Acknowledgements

This research is partially supported by funding from Horizon 2020, the European Union's Framework Program for Research and Innovation, under grant agreement No. 814523. ThoR has also received funding from the National Institute of Information and Communications Technology in Japan.

References

[1] Oshima N, Hashimoto K, Horikawa D, Suzuki S, Asada M. Wireless data transmission of 30 Gbps at a 500-GHz range using resonant-tunneling-diode terahertz oscillator. 2016 IEEE MTT-S International Microwave Symposium (IMS) May 22-27, 2016, San Francisco, CA, USA.

[2] Zhang H, Sfarra S, Saluja K, Peeters J, Fleuret J, Duan Y, et al. Non-destructive Investigation of Paintings on Canvas by Continuous Wave Terahertz Imaging and Flash Thermography. J Nondestruct Eval. 2017; 36:34.

[3] Deng X, Li Y, Liu C, Wu W, Xiong Y. 340 GHz on-chip 3-D antenna with 10 dBi gain and 80% radiation efficiency. IEEE Trans. Terahertz Sci. Technol, 2015; vol.5, pp.619-627.

[4] Li L, Li Y, Yeo T, Mosig J, Martin O A. Broadband and High-Gain Metamaterial Microstrip Antenna. Appl. Phys. Lett. 2010; vol.96, 164101.

[5] Hisatake S, Nagatsuma T. Nonpolarimetric Technique for Homodyne-type Electrooptic Field Detection. Appl. Phys. Express 2012; vol. 5, 012701.

[6] Hisatake S, Nguyen Pham H H, Nagatsuma T. Visualization of the spatial temporal evolution of continuous electromagnetic waves in the terahertz range base d on photonics technology. Optica, 2014; vol.1, no.6, pp.365-371.

[7] Hisatake S, Kitahara G, Ajito K, Fukada Y, Yoshimoto N, Nagatsuma T. Phase-Sensitive Terahertz Self-Heterodyne System Based on Photodiode and Low-Temperature-Grown GaAs Photoconductor at 1.55 μm. IEEE Sensors Journal. 2013; vol. 13, pp.31-36.

Output Power Enhancement in Photonic-Based RF Generation by Optical Pulse Compression with a Dispersion Managed Fiber

— Simplified Compression Fiber —

Keisuke Oda Kohei Kudomi Ryogo Katagiri Masayuki Suzuki and Hiroyuki Toda
Doshisha University 1-3 Tatara-Miyakodani, Kyotanabe, Kyoto 610-0321 Japan
*Corresponding author: ctwc0346@mail4.doshisha.ac.jp, htoda@mail.doshisha.ac.jp

Abstract – In photonic-based RF generation, output power can be enhanced by compressing optical pulse width before photo diode. In this presentation, we describe the results of numerical simulation for using two-sectioned dispersion managed fiber (DMF) with a highly nonlinear fiber (HNLF) and a standard single mode fiber (SMF) for simplified compression fiber.

Keywords – Microwave photonics; microwave/millimeter-wave generation; self-phase modulation; optical fiber dispersion; optical pulse compression.

1. Introduction

Microwave and millimeter-wave generation based on photonic techniques [1-3] has proved to be useful as an alternative technique for generations of high frequency signal for many applications, such as opto-electronic (microwave) oscillator [4], W-band radar [5], Terahertz generation [6], and so on. In photonic-based Radio Frequency (RF) generation method, if the average optical power to the photodiode (PD) is kept constant and the optical pulse width is narrow, RF output power is enhanced [7-9]. So far [10, 11], we have demonstrated that narrow optical pulse can be obtained by the use of a constant anomalous dispersion fiber. However, if the linewidth of the light source is not zero, the quality of RF output such as phase-noise characteristic is reduced because of dispersion and/or combination of dispersion and optical nonlinearity [12, 13]. Recently, we have presented the use of dispersion managed fiber (DMF), achieved by connecting a normal dispersion fiber and an anomalous dispersion fiber, for optical pulse compression in order to reduce the quality degradation of 100-GHz RF output [14]. In this presentation, we describe the result of numerical simulation for using two-sectioned DMF with a highly nonlinear fiber (HNLF) and a standard single mode fiber (SMF) for simplified compression fiber.

2. Numerical simulation

2.1 Simulation model

Fig. 1 shows the simulation model. Two continuous wave lasers (wavelength: 1550 nm, linewidth: 0) with frequency separation of f_{RF} are combined with initial peak power denoted as P_0 and transmitted through a DMF. After transmitting DMF, a variable optical attenuator (VOA) was used so that average optical power to the PD becomes constant irrespective of DMF length. The RF output is generated after the PD. If the optical pulse is compressed by the DMF propagation, RF output power is enhanced. The electric field of the transmitted optical pulse in the DMF was calculated by using RSoft OptSim™. In the simulation, we considered second and third order dispersion, loss and Kerr nonlinearity and ignored stimulated Brillouin scattering, Raman scattering and

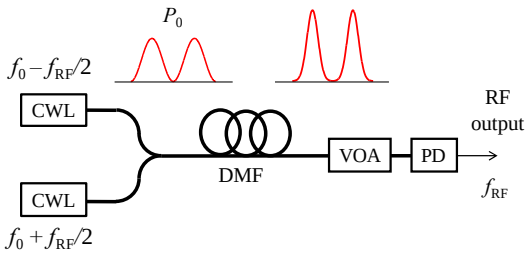

CWL: CW laser, DMF: Dispersion managed fiber, VOA: Variable optical attenuator, PD: Photo detector.

Fig. 1 Simulation model.

higher-order effects. After the electric field of the transmitted optical pulse is obtained, the generated RF output power is obtained by taking Fourier transformation of the optical intensity waveform to the PD. Then, we calculated RF gain due to optical pulse compression, which is defined as the ratio of RF power obtained from the compressed optical pulse to the RF power without fiber transmission. The theoretical limit of the RF gain obtained by this method is 6 dB [8].

2.2 Simplified compression fiber

We have investigated the RF power enhancement by the use of 2-sectioned DMF as shown in Fig. 2 constructed by two HNLFs [14]. Simulation parameters of the HNLF are loss of 1.0 dB/km, dispersion slope of 0.02 ps/nm^2/km and nonlinear coefficient of 12 W^{-1}km^{-1}, respectively. Fig. 3 shows the simulated RF gain versus the the DMF length L and P_0. 5.0 dB RF gain was obtained when P_0 is 27.0 dBm and L is 2.4 km. It is known that a linear anomalous dispersion fiber can be used for compensating frequency chirp generated by propagating in normal dispersion fiber with Kerr nonlinearity [15]. Therefore, we made a simulation, when f_{RF} is 100 GHz, using 2-sectioned DMF with a HNLF and a SMF for simplified compression fiber as shown in Fig. 4. The length of the HNLF L_1 is set to 1.0 km. Simulation parameters of the SMF with the length of L_2 are loss of 0.2 dB/km, dispersion slope of 0.06 ps/nm^2/km and nonlinear coefficient of 1.1 W^{-1}km^{-1}, respectively. Simulation parameters of the HNLF are the same as used in the DMF in the previous section. We inserted a VOA between HNLF and SMF in order to reduce the influence of Kerr nonlinearity in the SMF. Fig. 5 shows the simulated RF gain versus L_2 and P_0. The RF gain was maximized to be 5.8 dB when P_0 is 31.1 dBm and L_2 is 53 m. The RF gain of 5.0 dB was obtained when P_0 is 25.9 dBm and L_2 is 90 m. Using the DMF proposed here, the same RF gain (5.0 dB) is obtained with lower P_0 and shorter fiber length, even when compared in the length of the HNLF used in the first half of the DMF. Therefore, we can conclude that the DMF proposed here is more effective to enhance the RF output power than the previous DMF. The red dashed line in Fig. 5 shows the SMF length L_2 where the average dispersion of the DMF is zero. It should be noted that high RF gain is obtained when the SMF dispersion is over compensating the HNLF dispersion. In future, we will investigate the influence of the average dispersion of the DMF on RF output quality when the linewidth of the light sources is not zero.

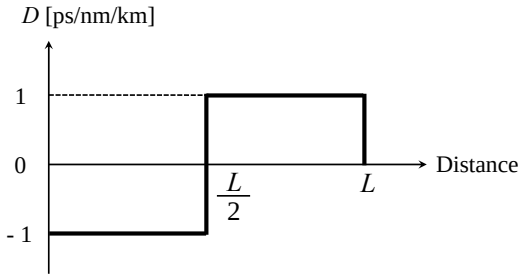

Fig. 2 Dispersion map of two sectioned DMF with two HNLFs.

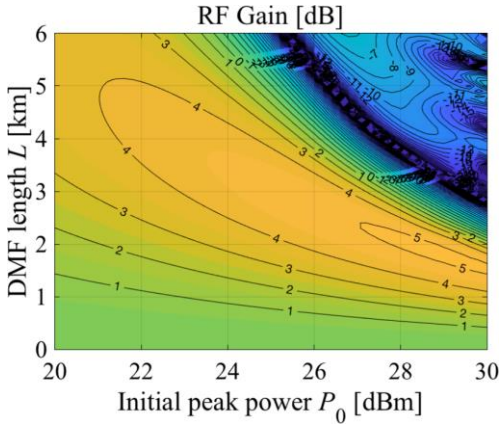

Fig. 3 Simulated RF gain versus L and P_0 using the DMF shown in Fig. 2.

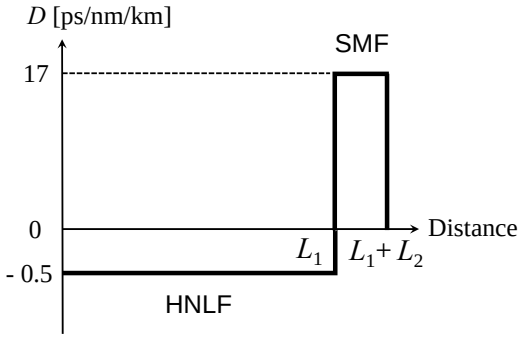

Fig. 4 Dispersion map of two sectioned DMF with a HNLF and a SMF.

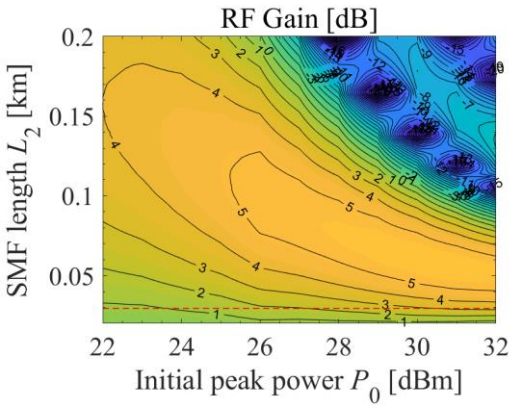

Fig.5 Simulated RF gain versus L and P_0 using two sectioned DMF with a HNLF and a SMF.

3. Conclusion

In photonic-based RF generation, the output power can be enhanced by compressing optical pulse width before PD. In this presentation, we proposed to use simplified DMF with a HNLF and a SMF. The RF gain of 5.0 dB was obtained when P_0 is 25.9 dBm with a 1 km HNLF and a 90 m SMF at 100 GHz RF generation. We believe that this technique is useful when a little more RF power is required in photonic-based RF generation.

References

[1] J. Yao, "Microwave photonics," *J. Lightwave Technol.*, vol. 27, no. 3, pp. 314-335, Feb. 2009.

[2] . J. A. Nanzer, P. T. Callahan, M. L. Dennis and T. R. Clark Jr., "Photonic signal generation for millimeter-wave communications," *Johns Hopkins APL Tech. Digest*, vol. 30, no. 4, pp. 299-308, Jan. 2012.

[3] K. Jung and J. Kim, "All-fibre photonic signal generator for attosecond timing and ultralow-noise microwave," *Scientific Reports*, vol. 5, no. 16250, pp. 1-7, Nov. 2015.

[4] X. S. Yao and L. Maleki, "Optoelectronic microwave oscillator," *J. Opt. Soc. Amer. B*, vol. 13, no. 8, pp. 1725-1735, Aug. 1996.

[5] Y. Li, A. Rashidinejad, J. -M. Wun, D. E. Leaird, J. –W. Shi and A. M. Weiner, "Photonic generation of W-band arbitrary waveforms with high time-bandwidth products enabling 3.9 mm range resolution," *Optica*, vol. 1, no. 6, pp. 446-454, Dec. 2014.

[6] T. Nagatsuma, S. Horiguchi, Y. Minamikata, Y. Yoshimizu, S. Hisatake, S. Kuwano, N. Yoshimoto, J. Terada and H. Takahashi, "Terahertz wireless communications based on photonics technologies," *Opt. Exp.*, vol. 21, no. 20, pp. 23736-23747, Oct. 2013.

[7] A. Hirata, M. Harada, T. Nagatsuma, "120-GHz wireless link using photonic techniques for generation, modulation, and emission of millimeter-wave signals," *J. Lightwave Technol.*, vol. 20, issue 10, pp. 2145-2153, Oct 2003.

[8] F.-M. Kuo, J.-W. Shi, H.-C. Chiang, H.-P. Chuang, H.-K. Chiou, C.-L. Pan, N.-W. Chen, H.-J. Tsai, C.-B. Huang, "Spectral power enhancement in a 100 GHz photonic millimeter-wave generator enabled by spectral line-by-line pulse shaping," *IEEE Photon. J.*, vol. 2, issue 5, pp. 719-727, Oct. 2010.

[9] J. -M. Wun, H. -Y. Liu, C. -H. Lai, Y. -S. Chen, S. -D. Yang, C. -L. Pan, J. E. Bowers, C. -B. Huang, J. -W. Shi, "Photonic high-power 160-GHz signal generation by using ultrafast photodiode and a high-repetition-rate femtosecond optical pulse train generator," *IEEE J. Sel. Topics Quantum Electron.*, vol. 20, issue 6, p. 3803507, Nov. 2014.

[10] T. Yamaguchi, H. Morimoto and H. Toda, "RF output power enhancement by optical pulse compression in photonic-based RF generation," *URSI J. Radio Science Bulletin*, no. 361, pp. 26-33, June 2017.

[11] T. Yamaguchi, S. Sakakibara, Y. Otagaki, H. Murata and H. Toda, "Output power enhancement in photonic-based 60-GHz generation by optical pulse compression with a dispersion shifted fiber," *International Topical Meeting on Microwave Photonics (MWP 2017)*, Wep.28, Beijing, Oct. 2017.

[12] K. Volyanskiy, Y. K. Chembo, L. Larger and E. Rubiola, "Contribution of laser frequency and power fluctuations to the microwave phase noise of optoelectronic oscillators," *J. Lightwave Technol.*, vol. 28, issue 18, pp.2730-2735, Sept. 2010.

[13] A. Cartaxo, B. Wedding and W. Idler, "Influence of fiber nonlinearity on the phase noise to intensity noise conversion in fiber transmission: theoretical and experimental analysis," *J Lightwave Technol.*, vol. 16, issue 7, pp.1187-1194, Jul 1998.

[14] R. Karembera, T. Yamaguchi, and H. Toda, "Output power enhancement in photonic-based RF generation by optical pulse compression with a dispersion managed highly-nonlinear fiber," *International Topical Meeting on Microwave Photonics (MWP 2018)*, Toulouse, Oct. 2018.

[15] S. Pitois, C. Finot, J. Fatome, B. Sinardet, and G. Millot, "Generation of 20-GHz picosecond pulse trains in the normal and anomalous dispersion regimes of optical fibers," *Opt. Commun.*, vol. 260, issue 1, pp.301-306, April 2006

InGaAs/InAlAs multiple quantum well Mach–Zehnder modulator integrated with planar antennas

Yusuke MIYAZEKI and Taro ARAKAWA
Yokohama National University, Graduate School of Engineering, 240-8501 Yokohama, Japan

*Corresponding author: miyazeki-yusuke-tf@ynu.jp

Abstract – We propose an InGaAs/InAlAs multiple quantum-well Mach–Zehnder modulator integrated with planar antennas. Wireless millimeter-wave (MMW) signals are received by the antennas and converted into light-wave signals without any cables and any external power supply. Since the modulator is based on InP, it can be fabricated monolithically with semiconductor light sources. By introducing the unique-multiple-quantum-well-core layer in arm waveguides, the modulator can be driven with low power consumption. The estimated extinction ratio of 10 dB was obtained when the MMW power density of 60 W/m^2 was incident on the modulator.

Keywords – multiple quantum well; Mach–Zehnder modulator; planar antenna;

1. Introduction

Wireless millimeter-wave (MMW) communication and sensing technology such as 5G and LIDAR have been attracting attention. In particular, sensing wireless MMW with highly sensitive and accuracy will be important to measure many MMW antennas for wireless MMW services. Phase modulators integrated with planar antennas are very effective for sensing wireless MMW. They enable us to directly convert wireless MMW signals into light-wave (LW) signals without any connection cables. Such modulators based on lithium-niobate (LN) [1] and nonlinear optical polymer [2] have been reported and performed high-sensitive-MMW sensing. However, electrorefractive index change Δn in the materials are relatively small, which results in the modulators to be as large as several centimeters. In this paper, we propose an InGaAs/InAlAs multiple quantum well (MQW) Mach–Zehnder (MZ) modulator integrated with planar antennas. Since the modulator is based on InP, it can be fabricated monolithically with laser diodes. In addition, a unique MQW exhibiting high electrorefractive index change Δn is adopted as a core layer in waveguides [3]. Therefore, the modulator can be compactness and achieve high-sensitive-MMW sensing with low power consumption.

2. Device Structure

Figure 1 shows the basic structure of the InGaAs/InAlAs MQW MZ modulator integrated with planar antennas. The modulator is composed of an InP-based MZ interferometer with two 3-dB multi-mode interference (MMI) couplers and an array of a two-element aluminum planar antenna. A gap-embedded patch antenna which has a micro gap in the center of itself is adopted as a planar antenna [4]. When wireless MMW signals with *x*-polarization are incident on the modulator, a displacement current is induced across the gap owing to the continuity of a current flow. As a result, strong electric fields in both positive and negative directions are induced across the gap. Arm waveguides of the MZ interferometer are placed under the micro gap since the induced electric field in the gap can be applied to the core layer effectively. By using the electric fields of both the directions induced in the gap, the modulator can be operated using push-pull driving. The arm waveguides are buried by benzocyclobutene (BCB) to separate the electric fields applied to each core layer. The BCB also can enhance the applied electric field. As a substrate, semi-insulating Fe-doped InP (Fe-InP) is adopted to enhance the antenna characteristics.

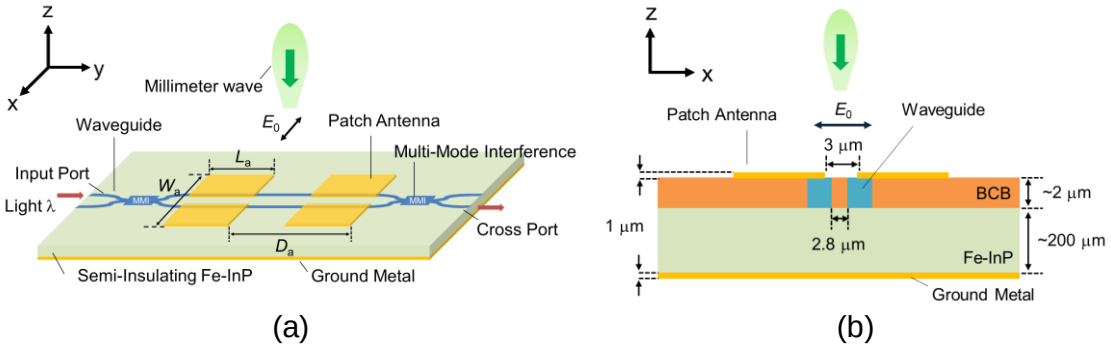

Figure 1. Schematic view of the proposed modulator. (a) Whole view and (b) cross-sectional view.

3. MQW Waveguide Structure

Figure 2 shows the band profile of the unique MQW, an InGaAs/InAlAs five-layer asymmetric coupled quantum well (FACQW). The operation principle of the FACQW is summarized in Ref. 3. It consists of a 23 Ml $In_{0.53}Ga_{0.47}As$ QW and a 17Ml $In_{0.53}Ga_{0.47}As$ QW. All the layers are lattice-matched to the InP substrate. The positive direction of the applied electric field is defined as showed in Fig. 2.

Figure 3 shows the calculated electrorefractive index change in the FACQW as a function of the electric field F for the TE mode at the wavelength λ of 1550 nm. The FACQW shows a large differential electrorefractive index change $|\Delta n/\Delta F|$ as large as approximately 4.0×10^{-4} cm kV^{-1} at the operation region of the electric field F between −8 and −16 kV cm^{-1} due to its unique quantum-confined Stark effect. The change in FACQW is several tens times larger than that in LN.

Figure 4 shows the schematic cross-sectional view of the waveguide. The core layer is composed of 12-set undoped InGaAs/InAlAs FACQWs and 10 nm InAlAs barrier layers between the FACQWs. To reduce the absorption loss resulting from the cladding layers, 50 nm undoped InGaAlAs (i-InGaAlAs) layers are inserted as separated-confinement-heterostructure (SCH) layers. The electric field applied to the core layer due to the built-in potential of the PIN structure is calculated to be as large as −12 kV cm^{-1}.

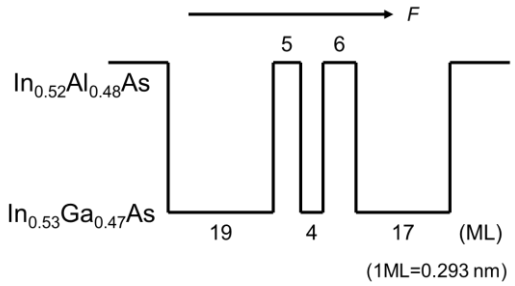

Figure 2. Band profile of the proposed FACQW.

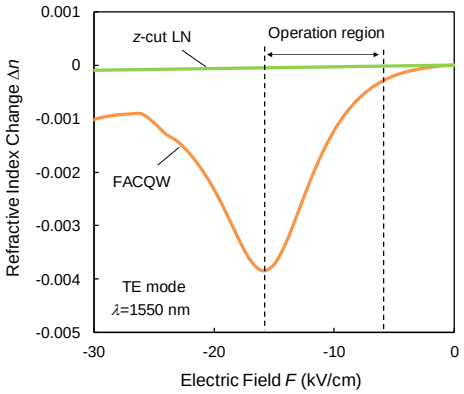

Figure 3. Calculated electrorefractive index change in the FACQW and z-cut LN as a function of the electric field for TE mode at the wavelength of 1550 nm.

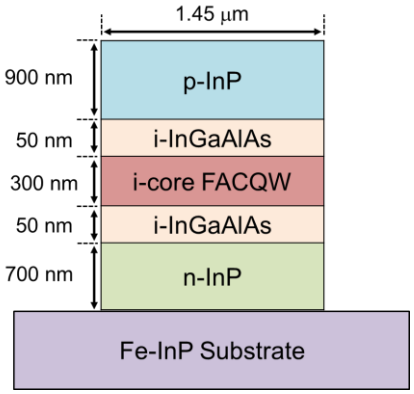

Figure 4. Schematic view of the waveguide.

4. MMW and Modulation Characteristics

Figure 5 shows the calculated distribution of the *z*-component of the electric field E_z on the upper surface of the antenna under the irradiation of 60 GHz band plane waves with *x*-polarization. The strong electric fields E_z in both positive and negative directions are induced in the micro gap. Consequently, the induced electric fields are applied to the core layer uniformly and intensively. The magnitude of the electric fields is 600 times larger than that of the incident waves E_0 of 1 V m^{-1}.

Figure 6 shows the static modulation characteristics of the proposed modulator. In this study, antenna length L_a and antenna width W_a were designed to be 714 μm and 900 μm. The antenna distance D_a was designed to be 2514 μm to achieve phase matching between the induced electric field and the optical filed propagating the core. Other parameters were designed to be as shown in fig. 1 (b). The extinction ratios of 10 and 20 dB were obtained when MMW power densities *P* of 60 and 85 W m^{-2} were incident on the modulator, respectively. Assuming that a horn antenna with a gain of 20 dB for the irradiation of wireless MMW signals is used from several tens of centimeters above the modulator, the input power for the antenna to obtain the extinction ratio of 10 dB is several tens of milliwatts.

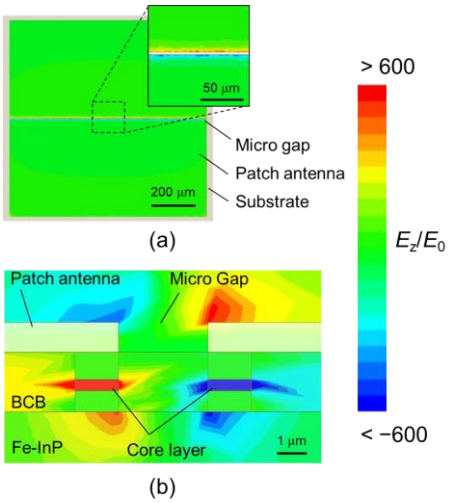

Figure 5. Calculated distribution of E_z/E_0 in (a) the upper surface of the antenna and (b) the cross-sectional view of the modulator.

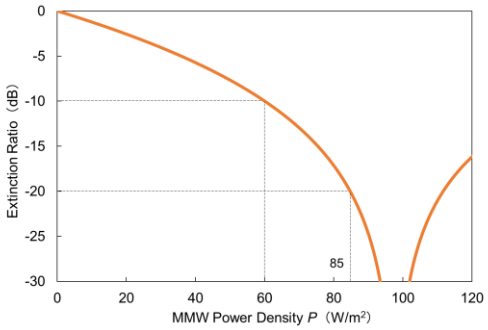

Figure 6. Static modulation characteristics as a function of the electric power density *P* which is incident on the modulator.

5. Conclusions

We proposed an InGaAs/InAlAs MQW MZ modulator integrated with an array of patch antennas for directly conversion from wireless MMW signals to LW signals with compactness and low power consumption. We believe that the proposed modulator is a promising candidate for measuring wireless MMW in the future.

Acknowledgements

The authors express sincere thanks to Prof. Joo-Hyong Noh at Kanto Gakuin University for supporting electromagnetic analysis using the FEM simulator. This work was partly supported by a Grant-in-Aid for Scientific Research B (No. 18H01897) from the Ministry of Education, Culture, Sports, Science and Technology.

References

[1] Y. Matsukawa, T. Inoue, H. Murata, A. Sanada Millimeter-wave band optical single-sideband modulator using array-antenna-electrode and polarization-reversed structures with asymmetric Mach–Zehnder waveguide Jpn. J. Appl. Phys. 2018; 57: 08PB04.

[2] D. H. Park, V. R. Pagan, T. E. Murphy, J. Luo, A. K.-Y. Jen, W. N. Herman Free space millimeter wave-coupled electro-optic high speed nonlinear polymer phase modulator with in-plane slotted patch antennas Opt. Express 2015; 23: 9464–9476.

[3] Y. Miyazeki, T. Arakawa Proposal of InGaAs/InAlAs multiple quantum well Mach–Zehnder modulator integrated with array of planar antennas Jpn. J. Appl. Phys. 2019; 58: SJJE05.

[4] Y. N. Wijayanto, H. Murata, Y. Okamura Electrooptic Millimeter-Wave–Lightwave Signal Converters Suspended to Gap-Embedded Patch Antennas on Low-kDielectric Materials IEEE J. Sel. Top. Quantum Electron. 2013; 19: 3400709.

Time-domain Analysis of Microwave Guided-Modes Propagating along FRPM Pipe Wall for Pipeline Inspection

Sayaka MATSUKAWA[1,2*], Kosuke YOSHIDA[2], Tadahiro OKUDA[3], Masaya HAZAMA[3], Satoru KUROKAWA[1], Hiroshi MURATA[2]

[1]National Metrology Institute of Japan, National Institute of Advanced Industrial Science and Technology, 305-8563 and Ibaraki, Japan

[2] Graduate School of Engineering, Mie University, 514-8507 and Mie, Japan

[3]Kurimoto Ltd, 527-0108 Shiga, Japan

*sayaka-matsukawa@aist.go.jp

Abstract –We have proposed a new nondestructive inspection technique for underground FRPM pipelines by using microwave guided-modes propagating along the pipe wall. In this paper, to investigate a detail of the transmission characteristics of the microwaves propagating along the pipe wall, time-domain analyses of measured and simulated microwave signals are discussed. The microwaves propagating along the FRPM pipe wall can be represented with a theoretical equation based on the propagating model along the FRPM slab with periodic boundary condition corresponding to the expanded pipe wall. The time-domain responses of the simulated microwave signals by using this equation were in good agreement with that of the measured results. The time-domain analysis of the microwave guided-modes enables us to have easy-to-use inspection methods for various buried pipelines.

Keywords – FRPM pipeline, microwave, nondestructive inspection, transmission coefficient, time-domain analysis.

1. Introduction

Fiberglass-reinforced plastic mortar (FRPM) pipelines are widely used for various underground infrastructures such as agriculture, sewerage, and power cable protection pipelines, which is due to FRPM's excellent characteristics of mechanical robustness and chemical stability [1]. These pipelines can have a long lifetime of several dozen years if appropriate inspections and maintenances would be applicable periodically. However, an excavating work for inspecting the underground FRPM pipeline requires a lot of costs and time. Therefore, it is required to develop a nondestructive inspection technique for the underground FRPM pipeline.

For the nondestructive inspection techniques of FRPM pipelines, the method using ultrasound, X-rays and MRI have been studied [2]–[4]. However, ultrasound has a low signal-to-noise ratio in the measurement. X-rays and MRI require specific measurement equipment unsuitable for underground operations, are unsuitable for the inspection of the underground FRPM pipelines.

On the other hand, we found that FRPM is a low-loss dielectric material (ε_r = 4 – 10, tan δ ~ 0.01) for microwaves in the frequency range of 1–10 GHz, and proposed a new nondestructive inspection method using a guided-mode propagation of microwave [5]–[7]. In our previous studies, by installing a dipole antenna on the end faces of the FRPM pipe and by measuring microwaves propagated along the FRPM pipe wall, the microwave transmission signals were measured, the possibility of non-destructive inspection of buried FRPM pipelines (with/without a crack/foreign object in/on the pipe wall) has been demonstrated [5]–[7].

In this paper, to investigate a detail of the transmission characteristic of the microwaves propagating along the wall of an FRPM pipe, time-domain analyses of measured and simulated microwave signals are discussed.

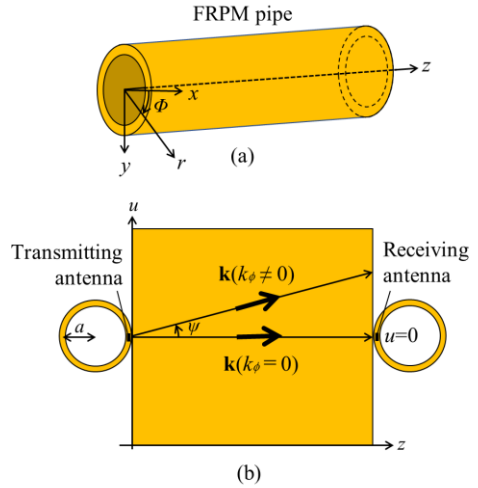

Figure 1. Theoretical model of FRPM pipe: (a) cylindrical model, (b) expansion view model of the FRPM pipe.

2. Theoretical analysis of microwaves propagating along FRPM pipe wall

Figure 1(a) shows a model of the FRPM pipe to perform a theoretical analysis of microwaves propagating along a FRPM pipe wall. It is assumed that the FRPM is linear, isotropic and homogeneous. In our previous study, we confirmed the microwave TE guided modes (TE_{0n}) with well-confined in the pipe wall region can be excited easily and propagated along the pipe wall when appropriate line antennas are installed on the end of the FRPM pipe along the circumferential direction [5]–[7]. Therefore, we suppose the microwaves of TE guided modes propagate along the FRPM pipe wall as shown in Fig. 1(a).

The electric field of the microwave of the TE guided modes propagating along the FRPM pipe wall can be represented by the following equation

$$\mathbf{E} = \hat{\boldsymbol{\phi}}\, E_{mn}(\omega) {f_d}^m(r) {g_d}^n(\phi) * \exp[j(\omega t - \mathbf{k}\cdot\mathbf{r})] \quad (1)$$

$\hat{\boldsymbol{\phi}}$ is the unit vector for the ϕ axis in the cylindrical coordinate system, $E_{mn}(\omega)$ is an amplitude of the electric field, and ${f_d}^m(r)$ and ${g_d}^n(\phi)$ represent the mode distribution functions for the TE guided modes. m and n represent mode order. k is the wave number vector of the TE guided modes in the ϕ-z cylindrical plane for $r = a$, where a is the radius of the FRPM pipe. Therefore, k can be expressed by the following equation.

$$\mathbf{k} = \hat{\mathbf{z}} k_z + \hat{\boldsymbol{\phi}} k_\phi \quad (2)$$

$$k^2(\omega) = {k_z}^2 + {k_\phi}^2 \quad (3)$$

To discuss the microwave propagations along the FRPM pipe wall in detail, we can consider the simplified theoretical equation based on the propagating model along the FRPM slab with periodic boundary condition corresponding to the expanded pipe wall as shown in Fig. 1(b). In Fig. 1(b), the microwaves propagating along the FRPM pipe can be represented as the waves propagating with an angle of ψ to the z axis. A wave propagates toward the positive z direction when an angle of ψ is zero. With the assumption of the closely confinement of the microwave fields in the FRPM core region as the TE_{00} mode, the electric field can be represented by the following equations.

$$E(u,z,\omega) = E_\psi(\omega) {f_d}^0(r) \exp[j(\omega t - \mathbf{k}\cdot\mathbf{r})] \quad (4)$$

$$\exp[j(\mathbf{k}\cdot\mathbf{r})] = \exp(\alpha r)\exp(j\beta(\omega) r) = \exp(\alpha r)\exp[j\omega\{r(n_{\text{eff}}/c_0)\}] = \exp(\alpha r)\exp(j\varphi) \quad (5)$$

$$r = u\sin\psi + L\cos\psi \quad (6)$$

$$\beta(\omega) = n_{\text{eff}}\, k_0 = n_{\text{eff}}(\omega/c_0) \quad (7)$$

$$n_{\text{eff}} = n_{\text{eff0}} + (\mathrm{d}n_{\text{eff}}/\mathrm{d}f)(f - f_0) + (1/2!)(\mathrm{d}{n_{\text{eff}}}^{(2)}/\mathrm{d}f^{(2)})(f - f_0)^2 + (1/3!)(\mathrm{d}{n_{\text{eff}}}^{(3)}/\mathrm{d}f^{(3)})(f - f_0)^3 \cdots \quad (8)$$

$$\varphi = \omega r[\{n_{\text{eff0}} + (\mathrm{d}n_{\text{eff}}/\mathrm{d}f)(f - f_0)\}/c_0] \quad (9)$$

$$e_{\psi\_t_d}(t) = (1/2\pi)\int_{-\infty}^{\infty} E_\psi(\omega) {f_d}^0(r) * \exp(-\alpha r)\exp(-j\varphi)\exp(j\omega t)\mathrm{d}\omega \quad (10)$$

Where α is an attenuation constant, r is a propagation distance. L is a total length of FRPM. $\beta(\omega)$ is a phase constant. n_{eff} is an effective index of the guided mode, and depends on frequency. n_{eff0} is a group index. $e_\psi(t)$ represents a time-domain response of a microwave transmission signal.

Since an FRPM pipe has a cylindrical structure, a train of the multiple microwave signals with different delay times (corresponding to different propagation

paths) will be observed when a receiving antenna is set at an appropriate position at the other end of the pipe to the input antenna. Therefore, the observed microwave transmission signal from the receiving antenna can be represented by the superposition of time-domain responses of (10) as shown in the following.

$$e_{\psi_{receive}} = e_{\psi 1\_t_1} + e_{\psi 2\_t_2} + e_{\psi 3\_t_3} + e_{\psi 4\_t_4} + e_{\psi 5\_t_5} \quad (11)$$

3. Measurement method

A commercially available sleeve-dipole antennas were used as the transmitting and receiving antennas. These antennas were installed on both end faces of the FRPM pipe (Fig. 2). Then, by adjusting the position of the transmitting antenna, the input microwave signal was mainly coupled to the fundamental microwave guided mode of the TE_{00} mode. Microwave signals ranging from 1 GHz to 6 GHz were supplied from a vector network analyzer (VNA) to the transmitting antenna. The position of the receiving antenna was changed to bring it along the circumferential direction of the FRPM pipe with a step length. When the two antennas were on the straight line with the shortest path each other, the receiving antenna position was defined as u = 0 as shown in Fig. 1(b). The transmission coefficients $S_{21}(\omega)$ were measured by using the VNA. For the time-domain analysis, the connection point to the two antennas were used as the reference planes.

In our preliminary experiments, the group velocity of the microwave propagated by TE_{00} guided mode along this FRPM wall was 1.31×10^8 m/s.

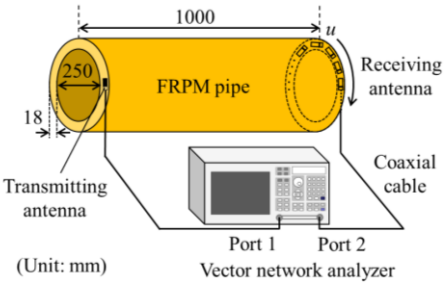

Figure 2. Measurement setup.

4. Time-domain analysis of microwaves propagating along FRPM pipe

A. *Measurement results*

The measured transmission coefficient S_{21} in frequency-domain for u = 0 is shown in Fig. 3. Then, the measured S_{21} was transformed into the time-domain response by using the inverse Fourier transform as shown in Fig. 4.

Several wave packets can be clearly observed in the figure. The first wave in Fig. 4 is considered to be a wave that directly propagated from the transmitting antenna to the receiving antenna along the shortest path. The time required for the microwave propagating along the shortest path was calculated as 7.6 ns when the FRPM pipe had a length of 1 m, and the group velocity was 1.31×10^8 m/s. This calculated value agreed well with the measured delay time of the (A) wave.

The second and third waves are considered as propagating in the clockwise direction or in the counterclockwise direction along the circumferential direction along the FRPM pipe wall. To check this

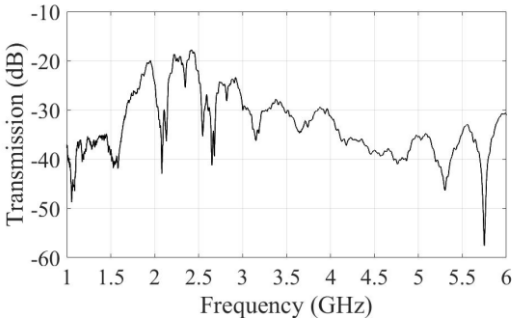

Figure 3. Measured frequency response of transmission coefficient S_{21}.

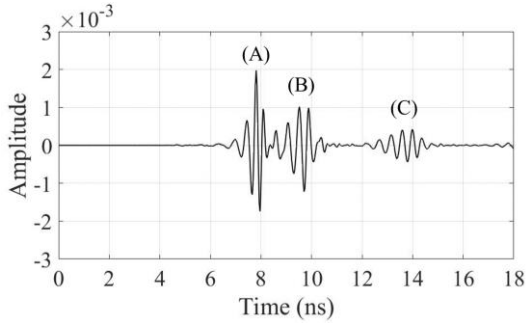

Figure 4. Microwave signal transformed to the time-domain (u = 0 mm).

hypothesis, the time-domain responses of the microwaves propagating along the FRPM pipe wall were simulated in next section.

B. Simulation results

In this section, we present the simulated results of the time-domain responses of microwaves propagating along FRPM pipe wall. Based on measured results, we can expect the microwave propagation paths corresponding to the observed pulse-like signals by using the model along the FRPM slab with periodic boundary condition as shown in Fig. 5. Therefore, the time-domain responses of the microwaves can be simulated using the models of Fig. 5 and (11) of Section 2. We also took into account of a microwave loss using preliminary experimental calculated results.

Fig. 6 is the calculated time-domain response of the microwaves with the receiving antenna position at u = 0 mm. These are in good agreement with those of the measured microwave signal in Fig. 4. By considering other parameters such as a tilted angle effect and a directivity of the antenna, more accurate calculation results can be obtained, we believe.

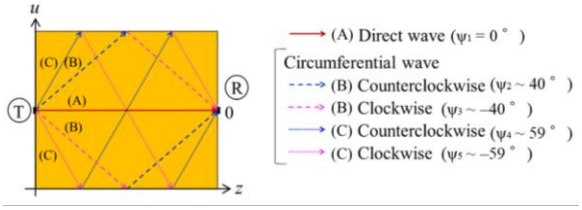

Figure 5. Propagation paths of the microwaves (u = 0 mm).

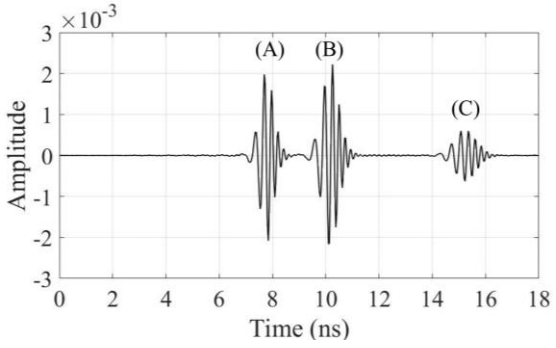

Figure 6. Simulation results of microwaves propagation (u = 0 mm).

5. Conclusion

In this paper, we investigated a detail of the transmission characteristics of microwaves propagating along the wall of an FRPM pipe by time-domain analyses of measured and simulated microwave signals. A train of the microwave pulse-like signals were observed in the measured results. The time-domain responses of the microwaves were also simulated using the model and theoretical equation. The time-domain responses of the simulated microwave signals by using this equation were in good agreement with that of the measured results. The time-domain analysis of the microwave guided-modes enables us to have easy-to-use inspection methods for various buried pipelines using both the experimental and theoretical methods.

References

[1] A. Cataldo, G. Cannazza, E De Benedetto, and N. Giaquito, “A TDR-based system for the localization of leaks in newly installed, underground pipes made of any material”, *Meas. Sci. Technol*. Vol. 23, pp. 1-9, 2012.

[2] E. Marfisi, C. J. Burgoyne, M. H. G. Amin and L. D. Hall, “Use of the MRI technique to study concrete and FRP reinforced concrete behavior,” *Research Leading to the Development of Design Guideline for the Use of FRP in Concrete Structure -2nd Con Fiber Crete Young Researcher Conference*, Corfu, Greece, June 2002.

[3] Y. Yokono, S. Matsubara, S. Matsui, M. Kitajima, H. Yabushita, S. Utoyama, N. Wakita, “Air-coupled Ultrasonic Inspection Technique for FRP Structure,” *Asia-Pacific Conference on NDT*, 2006.

[4] M. J. S. Lowe, D. N. Alleyne, P. Cawley, “Defect detection in pipes using guided wave,” *Ultrasonics*, Vol. 36, Issues 1–5, pp. 147-154, Feb. 1998.

[5] H. Murata, T. Okuda and M. Hazama, "Microwave Guided-Mode Propagation and Reflection along Fiber-Reinforced Plastic Mortal Pipe Walls and their Applications to Nondestructive Measurement," *PIERS 2018*, 2A5, p.375, August 2018, Toyama, Japan.

[6] F. Ueno, Y. Azuma, H. Murata, T. Okuda, M. Hazama, and Y. Okamura, “Nondestructive Inspection and Crack Detection of FRPM Pipe Using Electro-Optic Sensor and Microwave Guided-Mode Propagation,” *PEM 2015-12*, 2015.

[7] F. Ueno, H. Murata, T. Okuda, M. Hazama, and Y. Okamura, “New Nondestructive Measurement for Microwave and Photonic Techniques,” MWP/APMP 2014, TuED-2, 2014.

Experimental evaluation of spatial resolution for optical electric field sensor with dipole element

Kimihiro TAJIMA, Yoshiharu AKIYAMA
EMC Center,
NTT Advanced Technology Corp.
Musashino-shi, 180-0012 Tokyo, Japan

*Corresponding author: kimihiro.tajima@ntt-at.co.jp

Abstract –This paper presents a method for evaluating the spatial resolution of an optical electric field sensor with a dipole element by measurement. The electromagnetic wave radiated from a standard horn antenna was applied perpendicularly to a flat metal surface, and the electric field distribution of the generated standing wave was measured while moving the optical electric field sensor with a step width smaller than the element length. It evaluated by calculating the theoretical value of ideal dipole element length dependence by 0.1mm step. As a result, it was found that a spatial resolution equivalent to the element length can be expected with a deviation within 2.2 dB when the element length is 1 cm and the frequency is 2.5 GHz.

Keywords – spatial resolution**,** optical electric field sensor, dipole element, electric field distribution

1. Introduction

An electric field sensor having a high spatial resolution of measuring a change in electric field strength depending on a position with high accuracy is required for evaluating electric fields in the vicinity of a wireless device or an electronic device and evaluating characteristics of an EMC test facility [1].

The several kinds of optical electric field sensors with dipole element have been developed for measuring electromagnetic field distributions in EMC evaluation for the purpose of not disturbing them [2]-[5]. However, the indicators of spatial resolution performance have been rarely researched quantitatively.

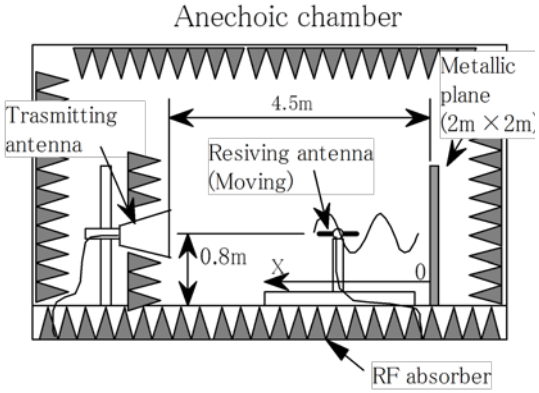

Figure 1. The setup for measuring spatial standing wave ratio.

In this paper the experimental evaluation results of the spatial resolution for an optical electric field sensor with a dipole element is reported.

2. Measurement setup

The spatial resolution of the electric field sensor was evaluated by measuring the spatial standing wave ratio using a measurement system as shown in Figure 1.

For measurement, vertically polarized electromagnetic waves were applied from a transmitting antenna to a metallic plane (2m × 2m) installed in a front position 4.5m away in a anechoic chamber with 6m length, and then a standing wave was generated. Next, an FRP moving base was installed at the center of the metal plane, and the moving base on rail was arranged to move in the direction perpendicular to the plane. Furthermore, a polystyrene stand was installed on the moving base so that the height was 80 cm, and an optical electric field sensor or a dipole antenna tuned to 2.5 GHz was fixed on the base so that the element was parallel to the moving axis X. Here, the element of the optical electric field sensor or the dipole antenna was made

horizontal, and moved parallel to the movement axis X in spite of applying the vertically polarized electromagnetic wave, so that the element was made perpendicular to the metal plane. This is because that it is possible to obtain a resolution difference due to the difference in element length.

The optical electric field sensor or dipole antenna was moved every 1 cm in the range of 40 cm with a separation distance x from the metal plane surface of 1 m to 1.4 m. Assuming that the change in electric field strength at this time is a standing wave distribution and the applied electromagnetic wave $E_i = A \exp(j\beta x)$ is totally reflected on the metal plate surface, the electric field strength E (x) at the distance x is expressed as following equation (1),

$$|E(x)| = |2A\cos(-\beta x + \theta_0)|. \quad (1)$$

Where A is the amplitude of the incident wave, β (= 2π / λ , λ : wavelength) is the phase constant, θ_0 is the phase angle of the reflected wave, and $\theta_0 = \pi$ in the case of total reflection. In the measurement, only the electric field strength and distance were measured, and θ0 was not measured.

As the optical electric field sensor, a sensor with very small element and a tuning dipole antenna were used. Figure 2 shows the structure of the optical electric field sensor [6].

The optical modulator is a Mach-Zehnder type optical modulator formed on a Z-cut LiNbO3 substrate having a length of 55 mm, a width of 1 mm, and a thickness of 0.5 mm

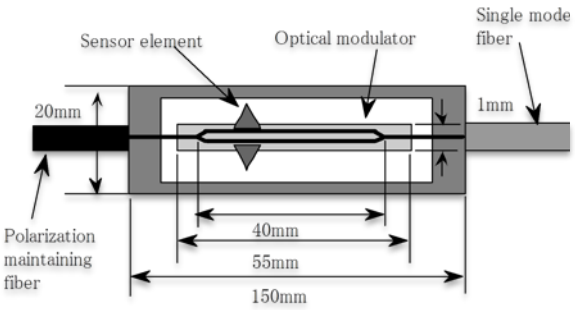

Figure 2. The electric field sensor module.

by an optical waveguide in which titanium is diffused. The length of the waveguide is 40 mm and the interval is 26 μm.

Two elements, 5 mm long, 2 mm bottom, 150 Å thick triangular nichrome film deposited on a 0.5 mm thick glass substrate, are bonded to the substrate so that the waveguide is sandwiched on the optical modulator.

3. Measurement result and estimation

Figure 3 shows the measurement results at 2.5 GHz. In the figure, the vertical axis is the relative voltage value when the value at x=1 m is 0, the horizontal axis is the movement distance, the solid line is the optical electric field sensor, the wavy line is the measured value with the tuned dipole antenna, and the dashed line is the theoretical value.

The cross-polarization characteristics of the tuned dipole antenna and the optical electric field sensor are about 40 dB and about 35 dB respectively, and the deviation between the measured values of the vertical polarization component and the horizontal polarization component is about 13 dB. The value is considered to be the traveling direction component (X-axis direction component in Figure 1) of the electromagnetic field.

From the figure, the measured value of the electric field sensor is close to the theoretical value, and it can be seen that the

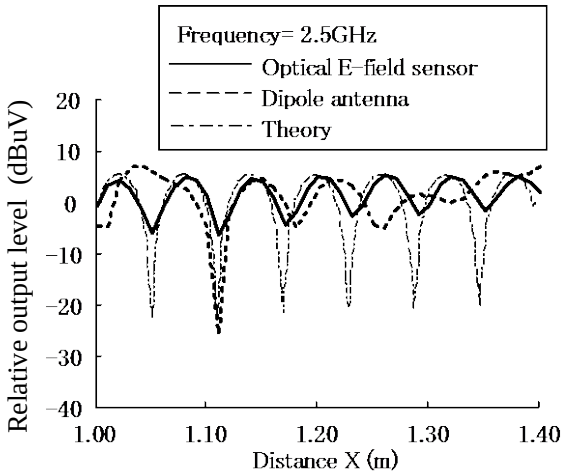

Figure 3. The measuring result of Spatial VSWR

standing wave distribution can be tracked almost accurately. On the other hand, the measured value of the dipole antenna is significantly different from the theoretical value, and the electric field distribution is considered to be disturbed by the size of the element and the metal cable.

Figure 4 shows the results of numerical evaluation of the spatial resolution of two peaks (120mm) in which the measured values and the theoretical values match relatively well. In the figure, the horizontal axis is the step width obtained by dividing the section distance X (= 120 mm) to be evaluated, and the vertical axis is the deviation from the voltage value E (x) obtained by equation (1) when the step width is 0.1 mm.

$$\Delta E(x) = E(x) - E_{mean}(x), \quad (2)$$

$$E_{mean}(x) = \sum_{n=1}^{N} E(x) / N, \quad (3)$$

where N is the number of divisions of the step width at each point X. The deviation ΔE (x) from the average value E_{mean} (x) at the step width at each point X was obtained by the equation (2), and the average value at the evaluated section was plotted in Figure 4.

From the measured values in the figure, it can be seen that an optical electric field sensor having a 10 mm dipole element can expect a resolution of about 10 mm if the deviation is 2.2 dB, which is the value at 20 mm in theoretical calculation and smaller than the theoretical value of 29.5 mm when

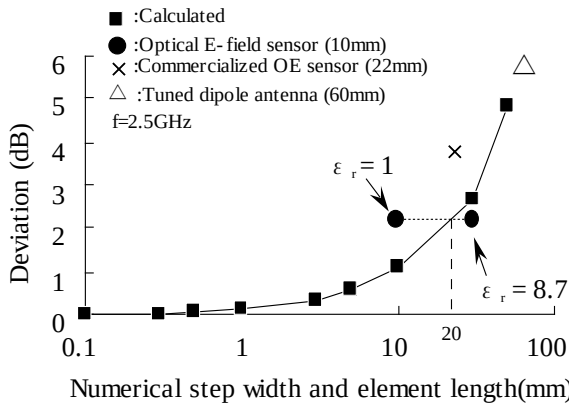

Figure 4. Numerical evaluation of the spatial resolution

the influence of the wavelength shortening rate due to the relative permittivity of the sensor casing is taken into consideration.

A commercial optical electric field sensor (element length 22 mm) measured for comparison had the spatial resolution of about 20 mm in the deviation 3.8 dB, and the tuning dipole antenna (element length 60 mm) had in the deviation of 5.7 dB.

4. Conclusion

In this paper, the method for evaluating the spatial resolution of an optical electric field sensor with a dipole element has been studied by measurement and calculation. For optical electric field sensor, it was found that a spatial resolution equivalent to the element length can be expected with a deviation within 2.2 dB when the element length is 10 mm and the frequency is 2.5 GHz.

References

[1] M. Kanda, and L.D.Driver, "An isotropic electric-field probe with tapered resistive dipoles for broadband use, 100kHz to 18GHz",IEEE Trans.Microwave Theory Tech.,Vol.MTT-35, no.2, pp.124-130, Feb.1987.

[2] K.D.Masterson, L.D.Driver, and M.Kanda, "Photonic probes for the measurement of electro-magnetic fields over broad bandwidths", IEEE. National Symp. on EMC, Denver, The U.S.A., pp.1-6, Aug.1989.

[3] N. Kuwabara, K. Tajima, R. Kobayashi, and F. Amemiya, “Development and analysis of electric field sensor using LiNbO3 optical modulator,” IEEE Trans. Electromag. Compat., vol.34, no.4, pp.391–396, Nov. 1992.

[4] K. Tajima, R. Kobayashi, N. Kuwabara, and M. Tokuda, “Development of optical isotropic E-field sensor operating more than 10 GHz using machzehnder interferometers,” IEICE Trans. Electron., vol.E85-C, no.4, pp.961–968, April 2002.

[5] Y. Toba, M. Sato, J.Ichijo, R.Osawa, and K.Haeiwa, “Development of an Evolutional Micro Isotropy Optical Electric Field Sensor,” IEICE Trans. C, vol. J91-C, No.1, pp.84–92, 2008.

[6] K. Tajima, R. Kobayashi, N. Kuwabara, and M. Tokuda, “Evaluation of Electric Field Sensor with Very Small Element using Mach-Zehnder Interfermeter,” IEICE Trans. B-II., Vol.J79-B-II, No.11, pp.744–753, Nov. 1996.

Time Domain Analysis of Reflected Microwave Signal for FRPM Pipeline Inspection to Detect Foreign Objects

Kosuke Yoshida[1*], Sayaka Matsukawa[1,2], Yoshihiro Nishimura[1], Satoru Kurokawa[2],

Tadahiro Okuda[3], Masaya Hazama[3], Hiroshi Murata[1]

[1]Electrical and Electronic Engineering, Graduate School of Engineering, Mie University, Japan
[2]National Institute of Advanced Industrial Science Technology (AIST), Japan
[3]Kurimoto Ltd., Japan

*419M241@m.mie-u.ac.jp

Abstract –We have proposed a new non-destructive inspection method for FRPM (Fiberglass Reinforced Plastics Mortar) pipelines using microwave guided-modes, which can propagate along FRPM pipe walls with relatively low loss. In addition, this signal is reflected by foreign objects. In this paper, the time domain analysis of the reflected signal is reported. Changes in the response time of the reflected signal were observed according to the foreign object position or materials. We believe that it can be used for non-destructive inspection of buried FRPM pipelines.

Keywords –non-destructive inspection; microwave guide-mode; FRPM pipeline; time domain analysis; reflected signal

1. Introduction

FRPM pipes are made of mechanically and chemically stable materials. However, at present, there is no practiced method for non-destructive inspection of the FRPM buried pipelines under-ground, although the total length of underground pipeline is said to be about 40,000 kilometers in Japan [1]. Therefore, there is a need for a method to perform inspection and diagnosis in a simple and short time by non-destructive inspection.

Currently, candidates of for a non-destructive inspection method for FRPM pipelines may be to use MRI, X-rays and ultrasound [2]-[4]. However, MRI and X-ray examinations are not suitable for under-ground pipelines because of the large equipment necessary. In addition, in the case of ultrasonic waves, the energy of the acoustic waves is stored in the space of the inner air or water, and it is not easy to obtain detailed information at the inside of the pipe wall or at the outside of the pipe wall which are actually required.

We focused on the fact that microwaves propagate along the FRPM pipe walls with relatively low loss. Based on that, we proposed a non-destructive inspection method using microwaves [5]. It has also been confirmed that microwave signals are reflected by a foreign object or crack.

In this paper, we report time-domain analysis of microwave reflected signals. By moving the receiving antenna in the circumferential direction of the pipe and repeating the analysis, the signal strength with respect to time is represented by a two-dimensional distribution map. By using this map the position of the foreign object can be specified.

2. Measurement Method

A schematic diagram of the experimental system is shown in Fig.1. 50 mm long dipole antennas were used as transmitting and receiving antennas. These antennas were installed on one end face of an FRPM pipe (the length of 1000 mm, inner diameter of 250 mm, and thickness of 18 mm). The positions of the receiving antenna and the transmitting antenna were changed, and the S parameter $S_{21}(\omega)$ was measured. The position of the antenna was changed along the circumferential direction clockwise from

x = -420 mm to +420 mm where x = 0 mm corresponds to the top of the pipe.

The microwave signal from 1 MHz to 9 GHz was supplied from the vector network analyzer (VNA) to the transmit antenna and the reflected microwave signal was received by the receive antenna. As the foreign objects, a concrete block (the length of 160 mm, width of 40 mm, and height of 40 mm) and a copper foil (the length of 160 mm, width of 40 mm) as shown in Fig.3 were used.

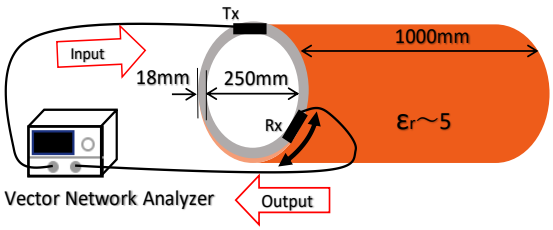

Figure 1. Experiment System.

Figure 2. Development view of the measured FRPM pipe.

(a)

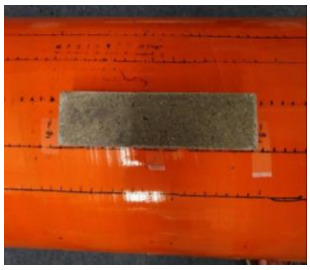

(b)

Figure 3. Foreign Objects.
(a)Concrete block. (b) Copper foil.

3. Result

3.1. Reflected signal from dielectric

A concrete block was placed at a position of x = 0, z = 500 mm. The measurement results when the receiving antenna was set at x = 150 mm and x = 250 mm are shown in Fig.4.

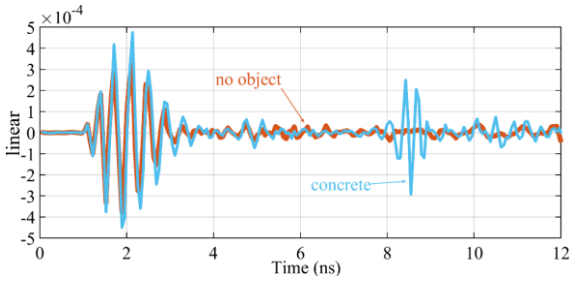

(a) x = 150 mm

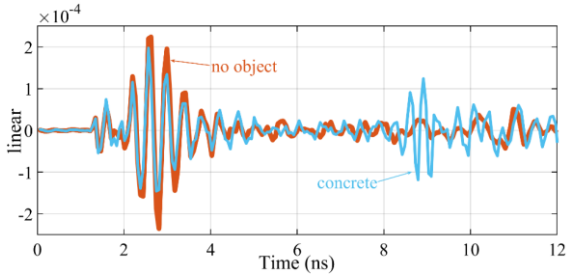

(b) x = 250 mm

Figure 4. Response time of reflected signal.

From these results, we can see that the clear reflected signals by the foreign object are observed.

Next, the transmission antenna was fixed, and the reception antenna was moved in the circumferential direction to repeating measurements. The results are shown in Fig.5.

In Fig.5, we can see that the reflected signals by the concrete are observed from 8.5 ns to 9.0 ns. Since the signal is appeared at 8.5 ns when the position x = 0, it can be said that the foreign object would be on the line at x = 0.

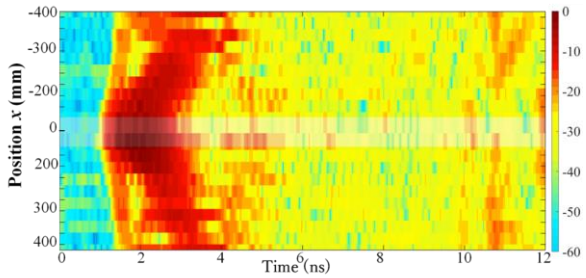

(a) No object.

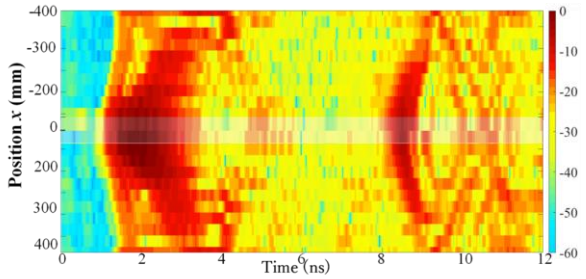

(b) Concrete.

Figure 5. Response time of reflected signal at each position (x = 0, z = 500).

Next, the result when moving the concrete block to the position of z = 600 mm on the line of x = 0 is shown in Fig.6.

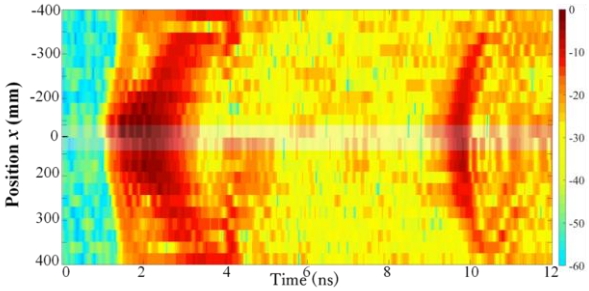

Figure 6. Response time of reflected signal at each position (x = 0, z = 600).

From Fig.6, the reflected signals were observed from 9.8 ns to 10.5 ns. This is about 1.2 times of the observed time in Fig.5 (z = 500 mm). Therefore, the correlation between the foreign object position and the reflected signal time was confirmed.

Next, Fig.7 shows the results when the foreign object was moved in the circumferential direction (x = 275 mm, z = 500 mm).

From this figure, it was confirmed that the first reflected signal was obtained at not the position of x = 0, but the position of x = 275 mm according to the shift of the foreign object position. This is appropriate as the position between the transmitting antenna and the foreign object has changed. From this result, the position can be specified even when the foreign object was located at arbitrary position the circumferential direction.

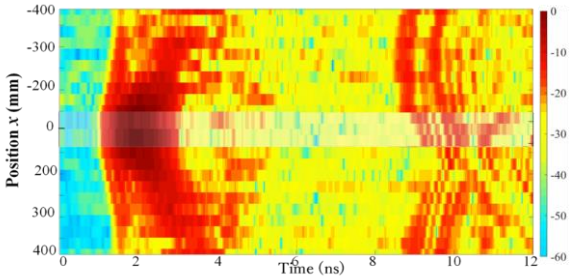

Figure 7. Response time of reflected signal at each position (x = -275, z = 500).

3.2. Reflected signal from metal

In the same way as the concrete block, a copper foil was placed at a position of x = 0, z = 500 mm. The measurement results with the receiving antenna at x = 150 mm and x = 250 mm are shown in Fig.8.

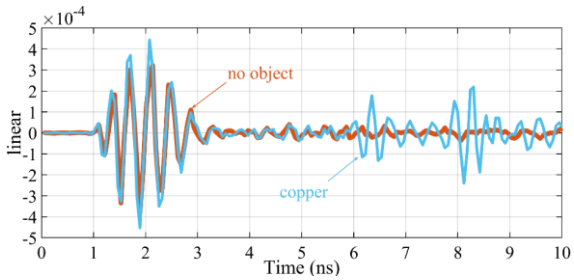

(a) x = 150 mm

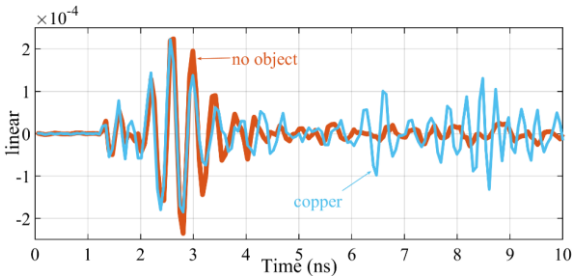

(b) x = 250 mm

Figure 8. Response time of reflected signal.

The transmission antenna was fixed at x = 0, and the reception antenna was moved in the circumferential direction to repeat measurements. The results are shown in Fig.9.

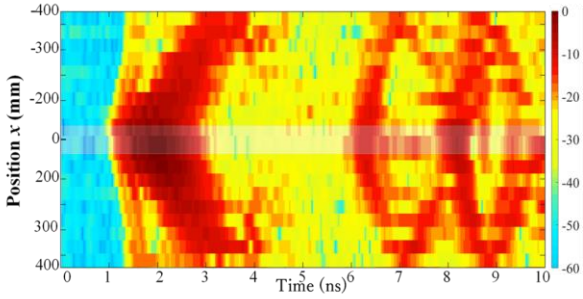

Figure 9. Response time of reflected signal at each position (x = 0, z = 500).

From this result, the reflected signals by the copper foil are observed from 6.5 ns to 7.0 ns. Despite being at the same position, the reflected signal is observed at the near side compared to the dielectric.

Next, the result when moving the copper foil to the position of z = 700 mm on the line of x = 0 is shown in Fig.10.

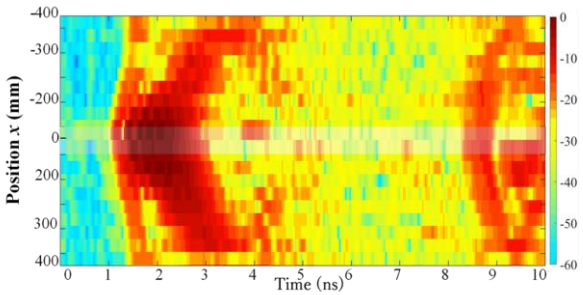

Figure 10. Response time of reflected signal at each position (x = 0, z = 700).

From Fig.10, the reflected signals were observed from 8.8 ns to 9.5 ns. This is about 1.4 times of the observed time in Fig.9 (z = 500 mm).

Next, Fig.11 shows the results when the copper was moved in the circumferential direction (x = 650 mm, z = 500 mm).

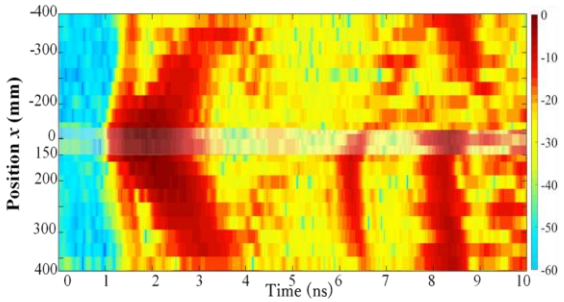

Figure 11. Response time of reflected signal at each position (x = 150, z = 500).

From Fig.11, the first reflected signal was confirmed to be obtained at x = 650 mm according to the foreign object position shift of the copper position.

4. Conclusion

In this paper, we reported on time domain analysis using microwave reflection signal of FRPM pipes. Using this technique, it is possible to identify the position of foreign objects outside the FRPM pipe. In the future, we believe that using EO sensors for diagnostics will reduce the extra signal from the antenna and/or metal cables and allow more accurate diagnostics in the buried pipelines.

References

[1] Y. Azuma, F. Ueno, H. Murata, Y. Okamura, T. Okuda, M. Hazama, "Precise Measurement of Microwave Evanescent Fields along Fiberglass-Reinforced Plastic Mortar Pipe Using Electro-Optic Sensor for Nondestructive Inspection," *Proceedings of the 21st Optoelectronics and Communications Conference / International Conference on Photonics in Switching 2016 (OECC/PS 2016)*, WA2-73, July 2016, Niigata, Japan.

[2] E. Marfisi, C. J. Burgoyne, M. H. G. Amin and L. D. Hall, "Use of the MRI technique to study concrete and FRP reinforced concrete behavior," *Resuarch Leading to the Development of Design Guideline for the Use of FRP in Concrete Structure - 2nd Con Fiber Crete Young Researcher Conference*, Corfu, Greece, June 2002.

[3] Y. Yokono, S. Matsubara, S. Matsui, M. Kitajima, H. Yabushita, S. Utoyama, N. Wakita, "Air-coupled Ultrasonic Inspection Technique for FRP Structure," *Asia-Pacific Conference on NDT*, 2006.

[4] M. J. S. Lowe, D. N. Alleyne, P. Cawley, "Defect detection in pipes using guided wave," *Ultrasonics*, Vol. 36, Issues 1-5, pp. 147-154, Feb. 1998.

[5] H. Murata, T. Okuda, M. Hazama, "Nondestructive Infrastructure Measurement Using Microwave Guided-Mode Propagation and Reflection along Fiber-Reinforced Plastic Mortal Pipe Wall in Underground Pipeline," *2018 IEEE CAMA*, 57.2, September 2018, Vasteras, Sweden

28 GHz-Band Antenna-Coupled Electrode Electro-Optic Modulators for 5G Mobile Communication Systems and Antenna Measurement Systems.

Hiroto Yokohashi[1*], Sayaka Matsukawa[2], Yui Otagaki[3], Hidehisa Shiomi[4],

Masahiro Sato[5,] Yoshikazu Toba[5], Satoru Kurokawa[2], Hiroshi Murata[1].

[1]Graduate School of Engineering, Mie University, 1577 Kurima-machiya-Cho, Tsu-City, Mie, 514-8507 Japan.
[2]AIST, 1-1-1 Umezono, Tsukuba, Ibaraki, 305-8563 Japan.
[3]King's College London, London, WC2R 2LS, UK.
[4]Osaka University, 1-3 Machikaneyama, Toyonaka, Osaka, 560-8531 Japan.
[5]SEIKO GIKEN Co. Ltd. 296-1 Matsuhidai, Matsudo, Chiba, 270-2214 Japan.
*419m240@m.mie-u.ac.jp.

Abstract – Antenna-coupled electrode electro-optic (EO) modulators operating in the 28-GHz band were analyzed, designed and fabricated for the applications to the next generation (5G) mobile wireless communication systems and to the precise antenna measurement systems. By analyzing the antenna-coupled electrode in detail with the 3-D model of the EO-crystal-stacked substrate, the electric field enhancement factor of approximately 8000 times of the irradiated 28-GHz field can be obtained for the optical modulation, which enables us to have a compact wireless-optical signal converter without external power supply. The designed EO modulator was fabricated using a 50-µm-thick $LiNbO_3$ crystal film and a 250-µm-thick SiO_2 base substrate, its signal conversion characteristic from the 28-GHz band wireless to optical signals were demonstrated successfully in the experiment.

Keywords – Antenna Electrode, Modulator, 28-GHz, Radio-over-Fiber System, Gb/s Data Transmission.

1. Introduction

In recent years, wireless communication technology has been rapidly developed, and the applications of wireless communication is rapidly spreading beyond smartphones and mobile phones [1].

We have proposed and developed data transmission experiments using an antenna-coupled electrode electro-optic modulators that converts wireless signals directly into optical signals [2]. They are also applicable to the Radio-over-Fiber (RoF) system, which are useful for 5G.

In this report, the results on the 28-GHz band antenna-coupled electrode electro-optic modulator are presented. The measured frequency bandwidth of the fabricated device was about 1.5-GHz in the 28-GHz band, and 1.5 Gb/s data transmission experimented was succeeded using the fabricated devise.

2. Basic Structure

The structure of the 28-GHz band antenna-coupled electrode electro-optic modulators is shown in Fig. 1. The substrate has a structure in which an $LiNbO_3$ crystal thin film and a base low-dielectric-constant substrate SiO_2 glass are bonded to each other, and the optical waveguide and the antenna-coupled electrodes are formed on the back surface of the $LiNbO_3$. The antenna-coupled electrode has a configuration in which two micro-strip patch antennas and a standing-wave resonant electrode are coupled by feed lines. In addition, by arranging a plurality of antenna electrodes in an array along the optical waveguide, wireless-optical signal conversion can be cumulatively increased, and sharp directivity can be obtained [3].

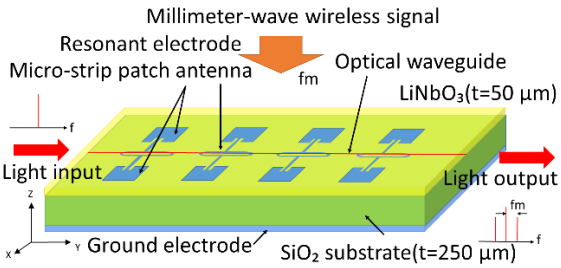

Figure 1. Basic Structure.

3. Simulation

A model was created using the three dimensional electromagnetic field simulator HFSS, and the model was analyzed under the condition irradiated with a 28-GHz band signal. The calculated surface electric field when a 28.7-GHz plane wave signal of the X-polarization is normally irradiated to the designed antenna-coupled electrode is shown in Fig. 2, where the observed plane was set slightly above from the standing-wave electrode surface of 0.01-μm. From the figure, it can be confirmed that a strong electric field of 8000-times of the irradiated 28.7-GHz signal is induced.

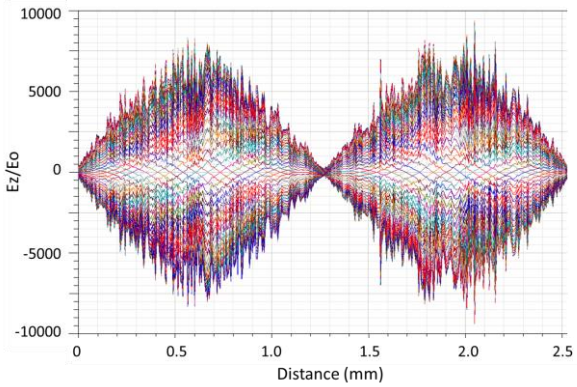

Figure 2. Surface Electric Field.

4. Prototype and Operating Experiment

We fabricated a 28-GHz band antenna-coupled electrode electro-optic modulator (4 elements) using z-cut $LiNbO_3$. Table 1 shows parameters of the designed modulator.

Fig. 3 shows the prototype antenna-coupled electrode electro-optic modulator. An evaluation experimental system of the antenna-coupled electrode electro-optic modulator is shown in Fig. 4. Fig. 5 shows the measured optical signal spectrum under the X-polarization irradiation. The obtained radio-to-optical signal conversion frequency dependence is shown in Fig. 6. The peaks were shown at 29.3-GHz and 30.2-GHz. In addition, the 3-dB frequency band was approximately 1.5-GHz.

Next, the obtained polarization dependence measurement results are shown in Fig. 7. The irradiation signal frequency was 29.3-GHz, which is a peak value. 0-degree corresponds to the X-polarization and 90-degree to the Y-polarization in Fig. 4. From the results, clear polarization dependence was confirmed.

Next, data transmission experiments were conducted by irradiating 29.3-GHz band radio signals intensity-modulated with a repetition frequency 0.5~1.5-GHz to the antenna-coupled electrode electro-optic modulator. The experiment system is shown in Fig. 8. The output light from the modulator was fed into a single mode fiber (SMF) having a length of 4-km and was converted in to an intensity modulated light. Then the converted light was detected by use of a high-speed photodiode and the detected electrical signal was evaluated.

Fig. 9 shows oscilloscope waveforms of the transmitted signals and received signals when a 1.2-Gb/s signal is irradiated, converted and light transmitted. Although attenuating amplitudes and some delays are observed, clear eye-patterns were confirmed, and Gb/s data transmission has been demonstrated.

Table 1. Parameters of the designed EO modulator.

Substrate Structure	
$LiNbO_3$ upper film thickness	50 μm
SiO_2 base substrate thickness	250 μm
Optical adhesive layer thickness	1.2 μm
SiO_2 buffer layer thickness	0.2 μm
Antenna-coupled electrode	
Square patch antenna length, L_a	1800 μm
Resonant electrode length, L_e	2528 μm
Feeding position, Δy	208 μm
Resonance electrode width, W	300 μm
Resonance electrode separation, S	30μm
Micro-strip line width, W_m	50 μm
Micro-strip line length, L_m	2565 μm

Figure 3. Fabricated EO modulator.

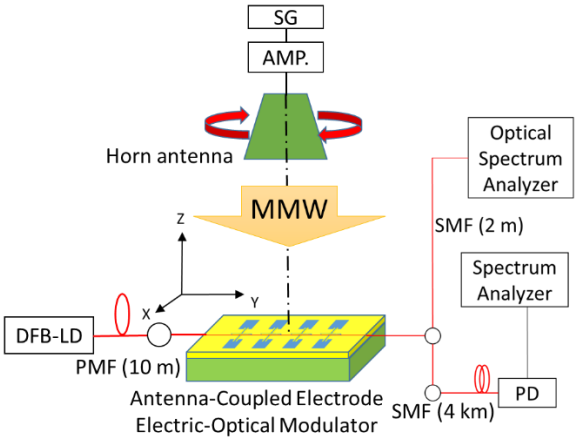

Figure 4. Experimental System.

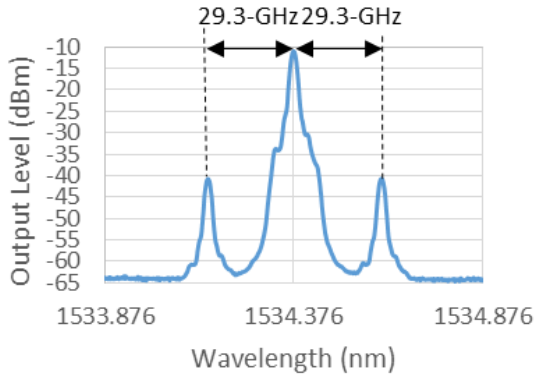

Figure 5. Optical Signal Spectrum.

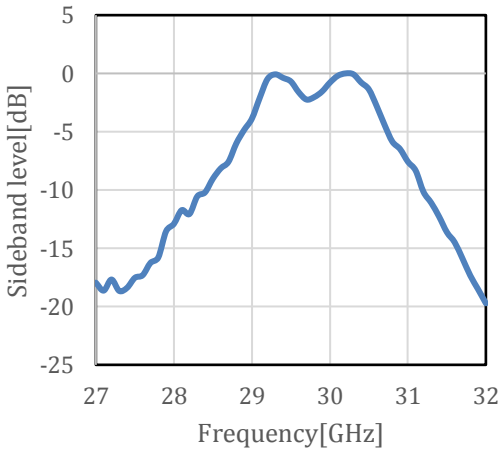

Figure 6. Frequency Dependence.

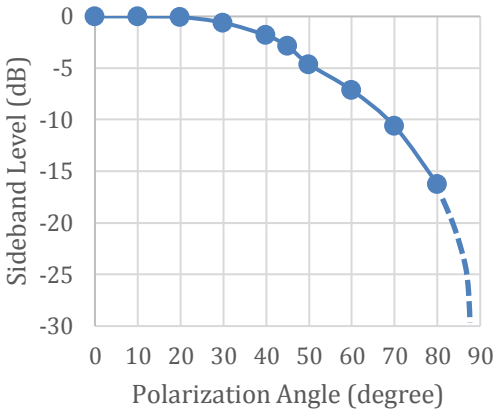

Figure 7. Polarization Dependence.

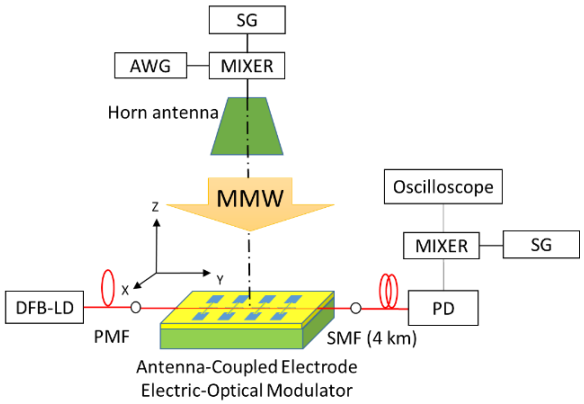

Figure 8. Data Transmission Experimental System.

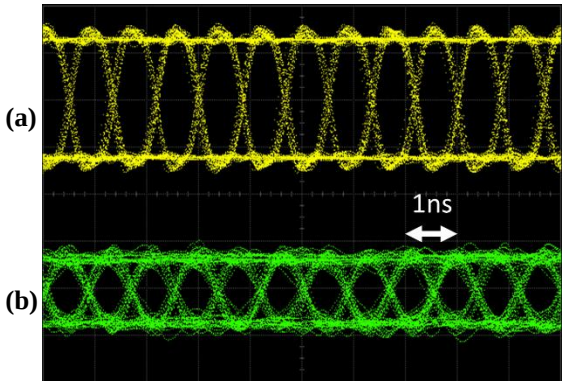

Figure 9. (a) Transmitted Signal and (b) Received Signal (1.2 Gb/s).

5. Conclusion

Experiments of the prototype 28-GHz band antenna-coupled electrode electro-optic modulators are reported. From the data transmission results, it was confirmed that ASK (On/Off Keying) data reception and optical signal conversion exceeding Gb/s were possible. If QAM signals are used,

data transmission of about 10 Gb/s can also be expected.

In the future, we plan to conduct application experiments to wireless signal links.

ACKNOWLEDGMENT

This work was supported in part by the SCOPE program, MIC, Japan.

References

[1] E. Dahlman, G. Mildh, S. Parkvall, J. Peisa, J. Sachs, Y. Selén, and J. Sköld, "5G Wireless Access: Requirements and realization," *IEEE Communications Magazine*, pp.42-47, December 2014.

[2] Hiroshi Murata, Ryota Miyanaka, and Yasuyuki Okamura :"Wireless space-division-multiplexed signal discrimination device using electro-optic modulator with antenna-coupled electrodes and polarization-reversed structures," *The International Journal of Microwaves and Wireless Technologies*, Vol.4, No.3, pp.399-405, 2012.

[3] H. Murata, Hiroto Yokohashi, Sayaka Matsukawa, Yui Otagaki, Hidehisa Shiomi, Masahiro Sato, Yoshikazu Toba, Satoru Kurokawa., "Antenna-Coupled Electrode Electro-Optic Modulator and 28 GHz-Band Wireless Signal Transfer over Fiber for 5G Mobile Systems," *OECC/PSC 2019*, WF1-5, July 2019, Fukuoka, Japan.

Electro-Optic Polymer Waveguide Devices for Continuous-Wave Terahertz Detection

Takahiro KAJI[1*], Isao MOROHASHI[2], Yukihiro TOMINARI[1], Yoh OGAWA[2], Norihiko SEKINE[2], Toshiki YAMADA[1], and Akira OTOMO[1]

Advanced ICT Research Institute, National Institute of Information and Communications Technology (NICT), [1]651-2492 Kobe and [2]184-8795 Koganei, Japan

*kaji@nict.go.jp

Abstract – We fabricated novel electro-optic (EO) polymer waveguide devices with gold antenna arrays for continuous-wave (CW) terahertz (THz) detection. We used a cyclo-olefin polymer (COP) with low dielectric constants and very small absorption losses in the THz region as a substrate. As a preliminary experiment for the THz wave detection, we fabricated push-pull Mach-Zehnder (MZ) modulators using EO polymer waveguides and planar gold electrodes and confirmed the low-frequency light modulation using the devices.

Keywords – electro-optic polymers; terahertz wave detection devices

1. Introduction

Communication technology using terahertz (THz) waves has received much attention for further speeding up and increasing capacity of wireless communication. The development of THz generation and detection devices based on photonics technology is important for realizing not only the devices operating in a broad THz range but also the THz-wave radio-over-fiber (RoF) system that converts THz signals to optical signals.

Organic electro-optic (EO) polymers [1-3] have large EO coefficients (> ~100 pm/V) and large figure-of-merit (FOM) values for THz wave generation and detection [4], compared with the other nonlinear optical (NLO) materials such as lithium niobate ($LiNbO_3$), zinc telluride (ZnTe), and organic DAST. The absorption coefficients of the EO polymers in the THz region are relatively small in the broad THz region [5] because the EO polymers do not have strong absorption due to crystal lattice vibration. In addition, the EO polymers have small dispersion of refractive index between optical frequencies and broad THz frequencies. Therefore, we can expect to realize the THz wave generation and detection devices with high efficiency and ultra-broad bandwidth operation using the EO polymers [6, 7].

In this study, we fabricated novel EO polymer waveguide devices with gold antenna arrays for continuous-wave (CW) THz detection. We used a cyclo-olefin polymer (COP) with low dielectric constants and very small absorption losses in the THz region as a substrate, enabling relatively large antenna size [8] with small absorption loss for increasing the detection efficiency.

2. Results

We designed the gold antennae of the detection device for the W-band (75-110 GHz) electromagnetic waves by electromagnetic simulation using finite-element method. Figure 1(a) shows schematic illustrations of the THz wave detection device. The gold antennae with a gap are placed on the upper cladding. The electric field is enhanced near the gap of the antennae by the irradiation of the THz wave, and the electric field with a vertical component [9] overlaps with the EO polymer waveguide. Then, the light propagating in the waveguide is modulated by the EO effect. Figure 1(b) shows microscopic images of the fabricated device. We fabricated the devices by the method of

transferring the poled EO polymer film to the substrate [7]. Our method can not only exclude the conductive clads and electrodes used for poling the EO polymer from the final devices but also enables to increase the degree of freedom in device design.

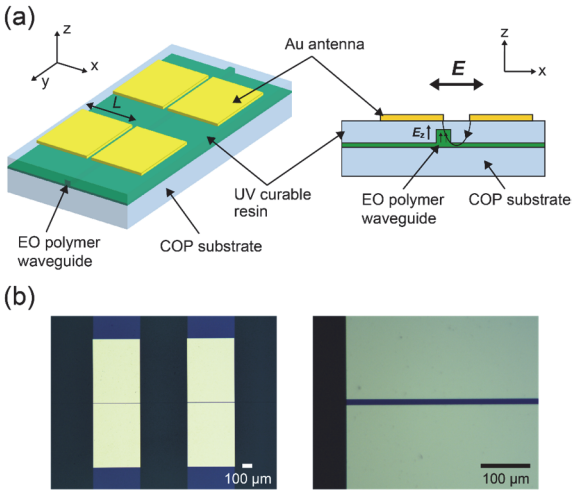

Figure 1. (a) Schematic illustrations and (b) microscopic images of a terahertz (THz) wave detection device using an electro-optic (EO) polymer waveguide and a gold antenna array.

As a preliminary experiment for THz wave detection, we fabricated push-pull Mach-Zehnder (MZ) modulators, which have a similar device configuration shown in Fig. 1, using EO polymer waveguides and planar gold electrodes. We confirmed the propagation of 1.55 μm light in the devices longer than 20 mm in length. Figure 2 shows the optical output signal from the fabricated modulator when a 1 kHz triangular wave voltage was applied to the device. The obtained optical modulation signal indicates that the fabricated device operates as a MZ modulator. From the voltage difference when the optical intensities were maximum and minimum, the $V_{\pi}L$ of the device was evaluated to be 14 V·cm.

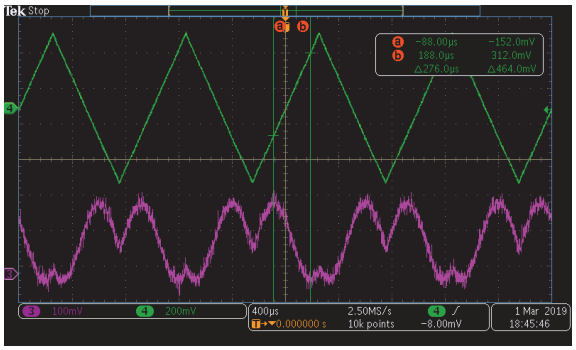

Figure 2. Modulated optical signal (purple) from the push-pull Mach-Zehnder (MZ) modulator using EO polymer waveguides and planar gold electrodes. A 1 kHz triangular wave voltage (green) was amplified 200 times and amplified to the device.

3. Summary

We designed and fabricated the novel CW THz detection devices using the EO polymer waveguides and gold antenna arrays. We also fabricated the push-pull MZ modulators consisting of the EO polymer waveguides and planar gold electrodes and confirmed the low-frequency light modulation using the devices.

4. Acknowledgment

This work was partially supported by Grants-in-Aid for Scientific Research (C) (18K04274) from the Ministry of Education, Culture, Sports, Science, and Technology (MEXT) of Japan.

References

[1] Dalton LR, Sullivan PA, Bale DH. Electric Field Poled Organic Electro-Optic Materials: State of the Art and Future Prospects. Chem. Rev. 2010; 110: 25–55.

[2] Yamada T, Aoki I, Miki H, Yamada C, Otomo A. Effect of Methoxy or Benzyloxy Groups Bound to an Amino-Benzene Donor Unit for Various Nonlinear Optical Chromophores as Studied by Hyper-Rayleigh Scattering. Mater. Chem. Phys. 2013; 139: 699–705.

[3] Yamada T, Miki H, Aoki I, Otomo A. Effect of Two Methoxy Groups Bound to an Amino-Benzene Donor Unit for Thienyl-di-Vinylene Bridged EO Chromophores. Opt. Mater. 2013; 35: 2194–2200.

[4] Zheng X, McLaughlin CV, Cunningham P, Hayden LM. Organic Broadband Terahertz Sources and Sensors. J. Nanoelectron. Optoelectron. 2007; 2: 1–19.

[5] Yamada T, Kaji T, Aoki I, Yamada C, Mizuno M, Saito S, Tominari Y, Tanaka S, Otomo A. Terahertz Time Domain and Far-Infrared Spectroscopies of Side-Chain Electro-Optic Polymers. Jpn. J. Appl. Phys. 2016; 55: 03DC11.

[6] Yamada T, Kaji T, Yamada C, Otomo A. Terahertz Wave Detection by the Stark Effect in Nonlinear Optical Polymers. Jpn. J. Appl. Phys. 2019; 58: 040901.

[7] Kaji T, Tominari Y, Yamada T, Saito S, Morohashi I, Otomo A. Terahertz-Wave Generation Devices Using Electro-Optic Polymer Slab Waveguides and Cyclo-Olefin Polymer Clads. Opt. Express. 2018; 26: 30466–30475.

[8] Wijayanto YN, Murata H, Okamura Y. Electrooptic Millimeter-Wave–Lightwave Signal Converters Suspended to Gap-Embedded Patch Antennas on Low-k Dielectric Materials. IEEE J. Sel. Top. Quantum Electron. 2013; 19, 3400709.

[9] Wijayanto YN, Murata H, Okamura Y. Wireless Microwave-Optical Signal Conversion in Quasi-Phase-Matching Electro-Optic Modulators Using Gap-Embedded Patch-Antennas. IEICE Trans. Electron. 2013; E96-C: 212–219.

Analysis of Polarization-Reversed Electro-Optic Modulator with Arbitrary Transfer Function and its Application to Pre-Equalization of Signal Distortion by Fiber Dispersion

Kenta Takaba[1*], Hiroshi Murata[1]

[1] Graduate School of Regional Innovation Studies, Mie University, Mie, Japan
*619M003@m.mie-u.ac.jp

Abstract –We have proposed a pre-equalizing electro-optic (EO) modulator utilizing the velocity mismatching between lightwave and electrical signal and the polarization reversal technique in order to overcome the fiber chromatic dispersion effect which is a problem in long-haul optical fiber transmission system. The inverse characteristic of the dispersion effect can be designed in the EO modulator by using the impulse response of the EO modulation with polarization-reversal structures, which can be tailored by tuning the polarization-reversed patterns. We calculated patterns to be implemented in the modulator using the Δ-Σ transformation.

Keywords – Pre-equalizing Electro-Optic Modulator, Polarization-Reversed Structures, Delta-Sigma Transformation

1. Introduction

A silica optical fiber is widely used for the long-haul telecommunication systems owing to its huge bandwidth (>100THz) and extremely low-loss (~0.2dB/km at 1.55nm). One drawback of the silica optical fiber is the dispersion effect, which causes phase distortion between signal components though the transmission. Therefore, it is important to realize a pre-equalization optical modulator with the reverse characteristic of the dispersion effect so that the phase relationship becomes to be required at the target transmission distance.[1].

In this paper, we discuss the transfer functions of the electro-optic (EO) modulator with polarization-reversed structures that gives the inverse characteristics of the dispersion effect, and the polarization reversal patterns to be given in the EO modulator by using the delta-sigma ($\Delta - \Sigma$) transformation.

2. Pre-equalizing EO modulator

2.1 Basic configuration

The basic structure of the EO modulator for the pre-equalization is shown in Fig.1. The optical waveguide is a Mach–Zehnder type optical waveguide to divide the lightwave into two parts and to give tailored real impulse responses with an optical phase difference of $\pi/2$, so that the modulation effects all the corresponding to the complex impulse responses.

For electrodes, the traveling-wave coplanar electrodes are used to tailor the impulse responses with the polarization-reversal structure to compensate for the dispersion effect.

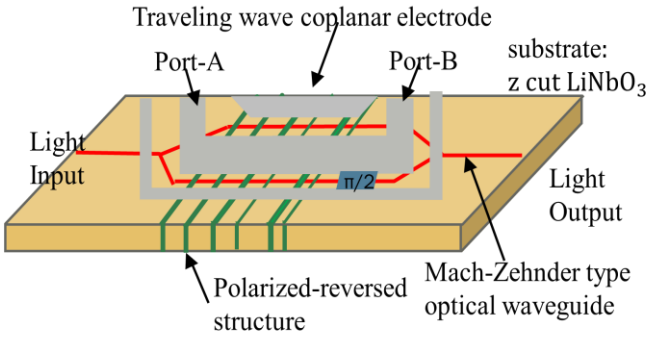

Figure 1. Basic structure of EO modulator using polarization.

2.2. Relationship between impulse response and polarization-reversed structure

2.2.1 Impulse response for dispersion compensation

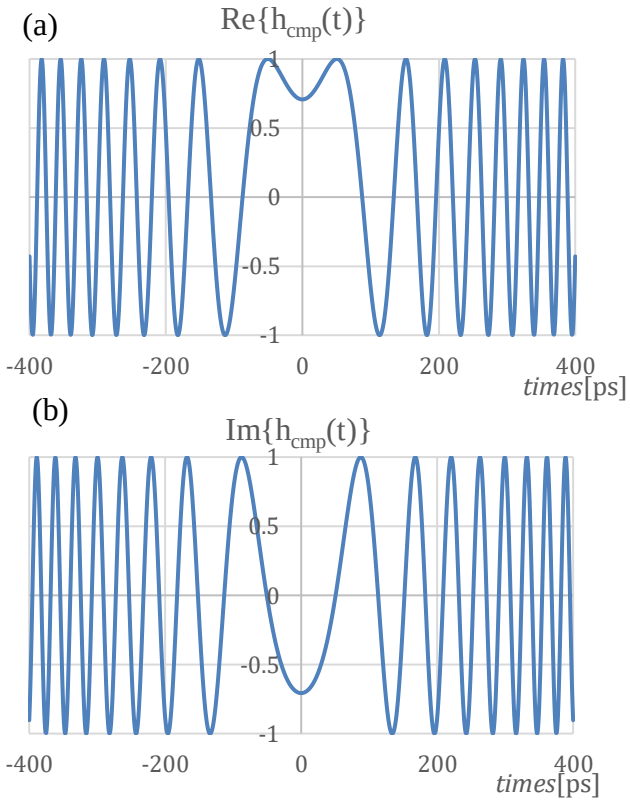

Figure 2. Complex impulse response of dispersion compensation. (a) Real part. (b) Imaginary part (Transmission distance L = 80 km).

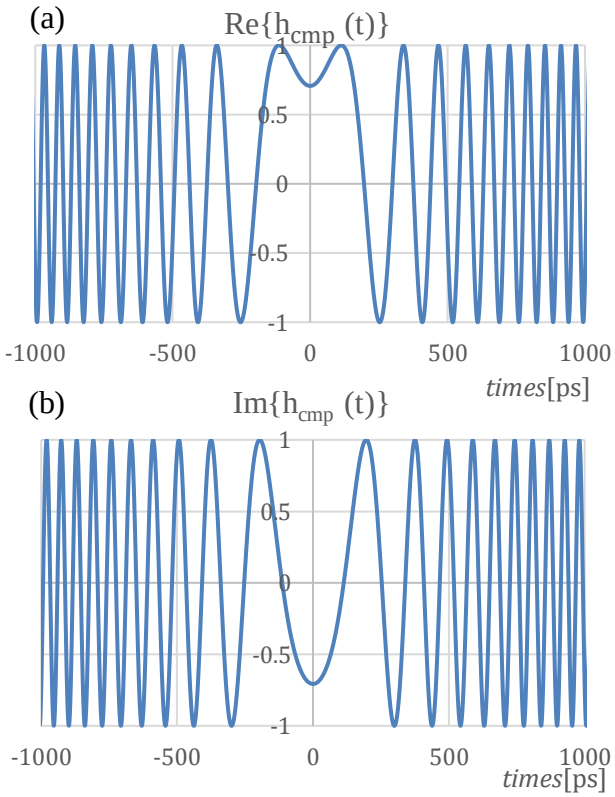

Figure 3. Complex impulse response of dispersion compensation. (a) Real part. (b) Imaginary part (L = 400 km) .

The transfer function of a single mode optical fiber with a length L can be expressed as following.

$$H(\omega) = \exp(j\beta(\omega)L) \quad (1)$$

The Taylor expansion of the propagation constant $\beta(\omega)$ is

$$\beta(\omega) = \beta_0(\omega) + (\omega - \omega_0)\beta_1 + \frac{1}{2}(\omega - \omega_0)^2\beta_2 + \cdots. \quad (2)$$

Since the main term contributing to the dispersion effect is the third term in Eq. (2), the transfer function related to the effect by the signal distortion is shown in Eq. (3).

$$H_{dis}(\omega) = \exp\left(\frac{1}{2}j\beta_2(\omega - \omega_0)^2 L\right) \quad (3)$$

Therefore, the complex impulse response to be provided for the compensator is given by Eqs. (4) and (5).[1]

$$H_{cmp}(\omega) = \frac{1}{H_{dis}(\omega)} = \exp\left(+\frac{1}{2}\mathrm{j}\beta_2(\omega - \omega_0)^2\mathrm{L}\right) \quad (4)$$

$$h_{cmp}(t) = \frac{1}{\sqrt{2\pi\beta_2 L}}\exp\{\mathrm{j}(\frac{\mathrm{t}^2}{2\beta_2 L} - \frac{\pi}{4})\} \quad (5)$$

2.2.2 Impulse response of traveling-wave EO modulator

In a standard traveling-wave EO modulator, it is important to match the propagation directions of the lightwave and the electrical signal and to match the both velocities. However, our EO modulator uses the configuration with velocity missmatching. A simplified model of a traveling wave EO modulator using polarization-reversed structures is shown in Fig.4.

Consider the case where an impulse signal is input to this traveling-wave EO modulator in the same direction with lightwave. Since the lightwave is usually faster than the electrical signal, the lightwave is modulated when it passes the impulse electrical signal. On the other hand, if the polarization-reversal structure is introduced, the sign of the optical phase modulation is reversed. Therefore the obtained impulse response is shown in Fig. 4 (a) and (b). The impulse response of the traveling-wave EO phase modulator using a polarization-reversed structures has a relationship corresponding to the polarization reversal patterns. The time width ΔT_1 of the impulse response is

proportional to the interaction length ΔL and the velocity difference between the lightwave and the electric signal, as shown in Eq. (6). Where n_m is the effective refractive index of the electrical signal, and n_g is the group refractive index of the lightwave.

$$\Delta T_1 = \Delta L \left| \frac{1}{v_m} - \frac{1}{v_g} \right| = \frac{\Delta L}{c} \left| n_m - n_g \right| \quad (6)$$

The time width for the compensation is proportional to the compensation using the velocity difference between the lightwave and the electrical signal as shown in Eq. (6). Therefore, in order to increase the time width corresponding to the compensable optical fiber length, it is effective that the electric signal is input from the opposite port to the lightwave. By using this configuration, the time width of the impulse response can be replaced as ΔT_2 [1].

$$\Delta T_2 = \Delta L \left| \frac{1}{v_m} + \frac{1}{v_g} \right| = \frac{\Delta L}{c} \left| n_m + n_g \right| \quad (7)$$

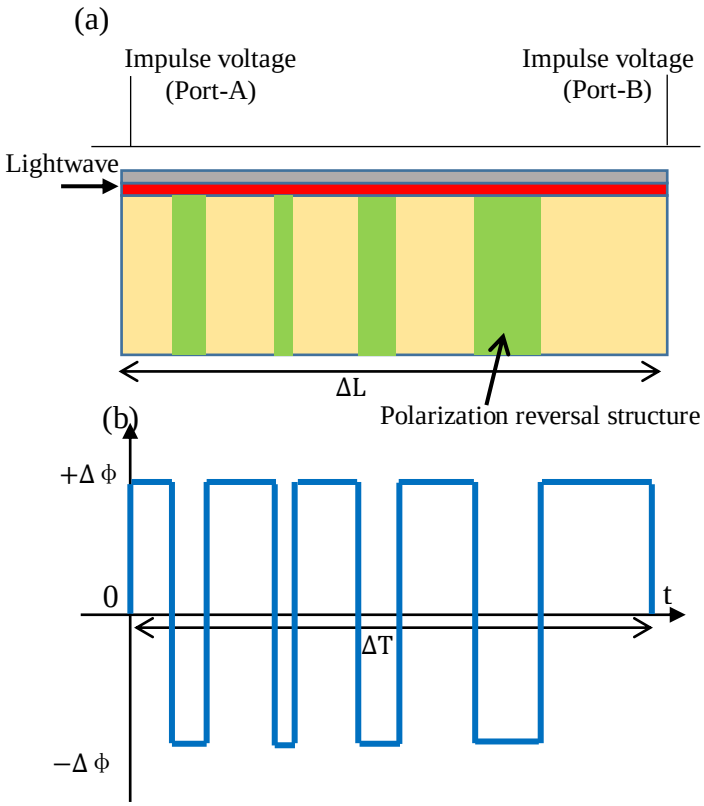

Figure 4. Traveling wave electro-optic modulator using polarization inversion structure. (a) Simple model. (b) Impulse response.

3. Design

3.1Transformation of impulse response using delta-sigma transformation

The polarization-reversed structures are designed using the impulse response for the dispersion compensation found in Section 2.2.1 and the relationship between the impulse response for the dispersion compensation and the polarization inversion pattern.

In order to obtain high-accuracy pre-equalizing characteristics, the polarization reversal patterns are designed using the Δ-Σ transformation technique. In this case, in addition to the 80 km transmission shown in Fig. 4, a simulation of 400 km transmission shown in Fig.5 was also conducted. In the analysis for the 80km transmission case of Fig. 5 the parameter Δ was set as 1ps, which corresponding to the shortest length of the polarization-reversed region of 150 μm by using Eq.(6) with n_m = 4 and n_g = 2. In the analysis for the 400km transmission case of Fig. 6, Δ was also set as 1ps, which is to be 50μm using for the shortest reversal region by using Eq. (7).Although it is necessary to add larger dispersion compensation, compensation is performed using the velocity difference between the lightwave and the electrical signal shown in Eq. (7).

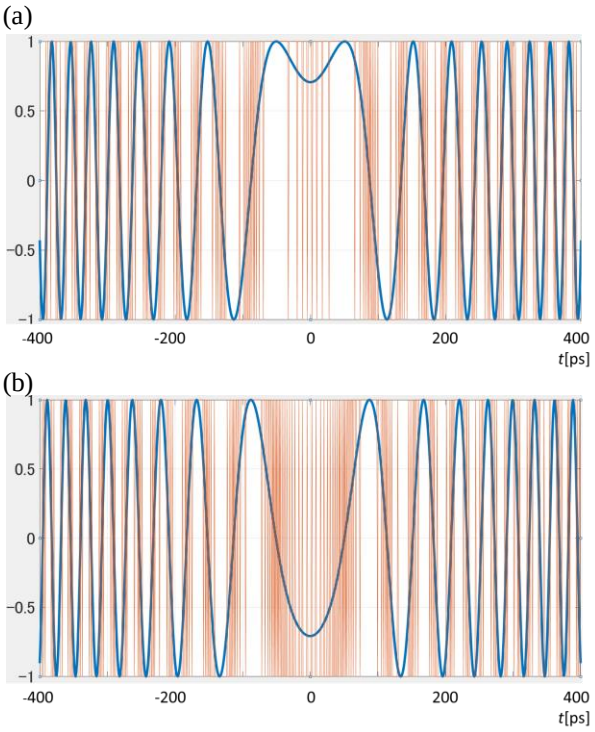

Figure 5. Designed polarization reversal pattern using Δ-Σ conversion. (a) Real part. (b) Imaginary part (L = 80 km).

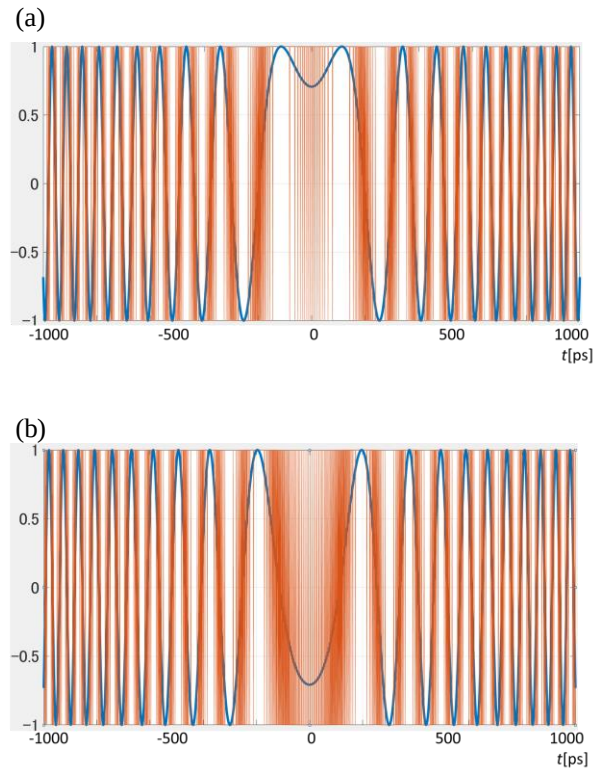

Figure 6. Designed polarization inversion patterns using Δ-Σ conversion. (a) Real part. (b) Imaginary part (L = 400km).

4. Conclusion

The design of the pre-equalization EO modulator are presented. With an appropriate window function, clear output responses are expected.

This work is for the synthesis of the transfer functions for the dispersion effect compensation using the polarization-reversed EO modulator. In this paper, simulation was conducted to compensate for the phase relationship distortion by the fiber dispersion. This technique, it can also be used for electric field measurement experiments using lightwaves. For example, phase distortion in measurement systems can be compensated for by use of our technique.

References

[1] Hiroshi Murata, Tomohiro Ohno, Takayuki Mitsubo, and Atsushi Sanada : "Pre-Equalizing Electro-Optic Modulator Utilizing Polarization-Reversed Structures of Ferro-Electric Crystal," IEICE Trans on Electronics, vol.E101-C, no.7, pp.581-585, 2018.

Visualization of a terahertz wave packet based on an electrooptic sensing for channel characterization

Hana Arisesa[1]and Shintaro Hisatake[2*]

[1]Department of Energy Engineering, Graduate School of Natural Science and Technology, Gifu University, 1-1 Yanagido, Gifu, 501-1193, Japan

[2]Department of Electrical, Electronic and Computer Engineering, Gifu University, 1-1 Yanagido, Gifu, 501-1193, Japan

*Corresponding author: hisatake@gifu-u.ac.jp

Abstract – We propose and demonstrate a system to investigate a terahertz channel by a visualization of a wave packet. The wave packet is modelled by summation of harmonic continuous waves at terahertz frequency range (120 GHz) and measured by using electrooptic sensor based on non-polarimetric self-heterodyne technique, assuming 10 Gbps data stream transmitted over terahertz propagation channels. We demonstrate not only the wave packet visualization but also the quantitative evaluation of the wave packet signal degradation within the propagation channel.

Keywords – terahertz wireless communication; wave packet; visualization; EO sensing;

1. Introduction

Terahertz (THz) technology as a candidate for the future wireless communication standard has been proposed in several decades ago, owing prominent characteristics compared to its competitors such as optical communication, infra-red technology and even the existing mature wireless communication technology at microwave band [1]. However, to be ready for the deployment, there still many aspects, requiring to be investigated. Due to its natural properties, THz wireless communication seems to be limited for short and medium distance, indoor application [2]. Several reports show that there will be two possible scenarios in indoor application, both line-of-sight (LoS) and non-line-of-sight (nLoS) [3, 4]. On the other hand, immersive THz wireless access environment consists of many objects and obstacles which can affect the THz wireless communication performance, such as chair, table, lamp, human, and even interference from other signal. Moreover, the THz frequency band suffers from high attenuation atmospheric absorption, free path loss and signal spreading. In addition, the dynamic phenomena in THz channel propagation such us multipath, reflection, roughness, and scattering will contribute to the THz wireless communication quality of service (QoS).

Several investigations on the short range, indoor THz wireless communication have been presented [5-7], using a different method such as ray tracing and direct measurement. In order to achieve desired capacity and data rates value, signal attenuation and scattering problem should be addressed in both LoS and nLoS scenario [5].

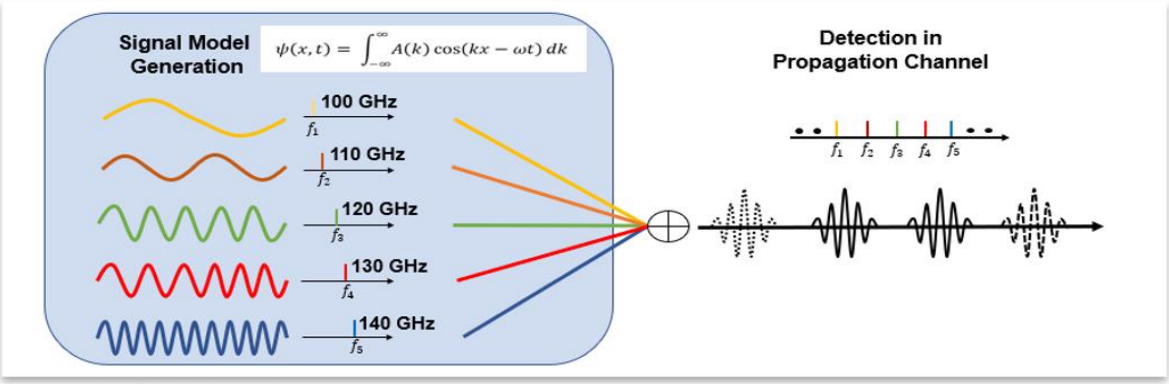

Figure 1. Principle system.

In this paper, we propose and demonstrate a measurement system to investigate THz channel propagation using electrooptic (EO) sensing technique [8]. Not only the wave packet visualization in the THz wave propagation channel, but also the quantitative evaluation of the wave packet signal intensity degradation within the propagation channel have been investigated.

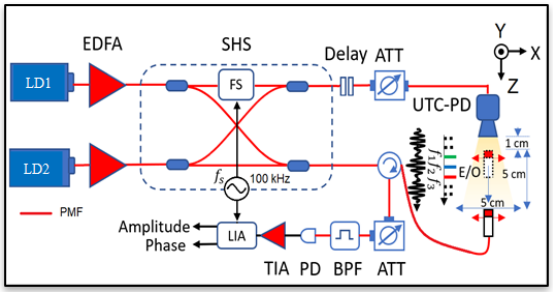

Figure 2. Setup measurement

2. Principle

Figure 1 shows the principle of the wave packet measurement based on the superposition of harmonic continuous frequency (CW). We generated five independent THz CW frequencies, radiated from horn antenna and summed them to form wave packet. In this experiment, the , centered was set to be 120 GHz. The repetition rate of the wave train was set to be 10 GHz. Each frequency is measured using our visualization system which is already applied to various applications [9- 11].

The superposition of harmonic CW frequency can be described by [12]

$$\psi(z,t) = A_n \cos(\omega_{av}t - k_{av}z) \frac{\sin(N/2(\delta_\omega t - \delta_k z))}{\sin(1/2(\delta_\omega t - \delta_k z))} \quad (1)$$

where $\psi(x,t)$ is the average frequency ($\frac{1}{2}(\omega_1 + \omega_5)$), k_{av} is the average wave number ($\frac{1}{2}(k_1 + k_5)$), δ_ω is the difference in angular frequency and δ_k is the difference of wave number between adjacent frequencies (in our experiment, δf =10 GHz). The component cos $(\omega_{av}t - k_{av}z)$ represents the high-frequency term as the carrier frequency of the wave packet. The

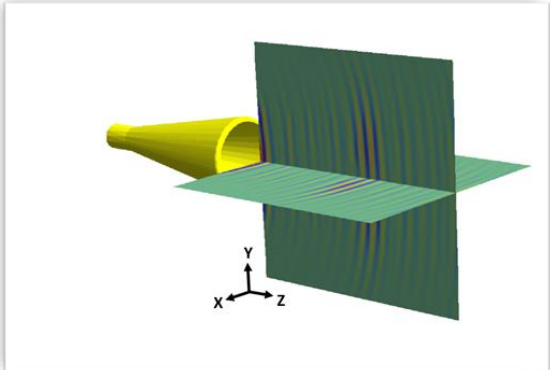

Figure 3. 3D wave packet visualization

remaining components show the low frequency term as the envelope of the wave packet.

3. Experiment and result

Figure 2 shows the experiment setup. THz CW frequency generated by photomixing using a uni-travelling-carrier diode (UTC-PD). Two laser diodes with the different frequency was set to be intended frequency, i.e 100 GHz, 110 GHz, 120 GHz, 130 GHz, and 140 GHz respectively, we visualized the THz CW frequency on the X-Z plane with area measurement 50 mm x 50 mm. Amplitude and phase of each THz CW frequency can be measured easily as shown in Fig. 3. The phase noise caused by the fluctuation of the laser can be reduced by setting the path difference between the RF and the LO arm using delay component. Amplitude and phase information can be used to form the THz real wave component by

$$\psi_1(x,z) = A_1(x,z) * cos(\Phi_1(x,z)) \quad (2)$$

where, $\psi(x,t)$ is a wave function with respect to time and space, $A_1(x,z)$ and $\Phi_1(x,z)$ are amplitude and phase distribution of the continuous wave for f_1 component respectively.

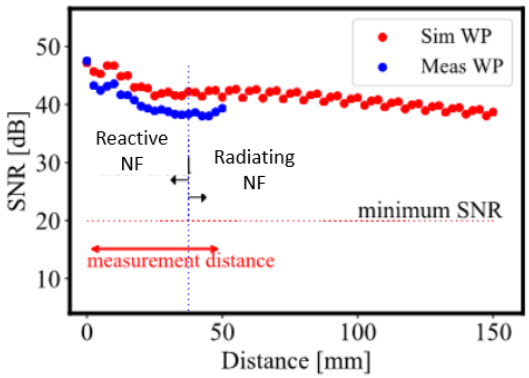

Figure 4. SNR degradation

We evaluated our system by measuring the SNR degradation of the wave packet along the propagation direction as shown in Fig. 4. The measurement area, Z axis direction, involved mostly in the near field region, the boundary for the reactive near file and the radiating near field at 35 mm. The SNR degradation of the measurement result, indicated with blue dots, compared to the SNR degradation of the simulation data, indicated with red dots. Here, we estimated SNR degradation for longer distance easily using the simulation.

The SNR degradation was calculated from based on both the experimental and the simulated data. In each measurement of CW frequency, we calculated SNR of each signal at initial point (starting point of the EO probe before performing area scanning) which is 10 mm in the center front the horn antenna. Having the SNR data on each frequency, we also calculated the total noise of the wave packet for investigation the SNR of the measured wave packet. Then, based on the measured data we can measure the travelling wave packet along the scanning area. The maximum wave packet signal was calculated by the highest amplitude of the wave packet. With the noise total of wave packet as previously calculated, the SNR degradation of the wave packet can be investigated. Meanwhile, the wave packet simulation also performed using numerical software up to the distance 150 mm. Due to lacking the noise data in the simulation result. We assume that noise wave packet simulation is same as noise wave packet at the measurement. The difference between SNR measured and simulated data about 3 dB, this may be caused in the noise averaging of the wave packet signal. In the reactive near field region, it is shown that the SNR decreased very fast and then declined steadily at the radiating near field region toward. The minimum SNR to be regarded as good measurement using our system is 20 dB. Thus, we can conclude that wave packet measurement can be extended into longer distance.

4. Conclusion

We demonstrated and propose a system to investigate THz channel propagation using wave visualization technique. It investigates the degradation of wave packet transmission on THz short range channel propagation. The system performed using electro-optic sensor based in self-heterodyne system. The degradation of SNR calculated by measuring the amplitude of the travelling wave packet on the measurement area. We validate the measurement data with simulation data from numerical software, and the SNR difference about 3 dB due to mismatch of the noise calculation. Although we demonstrated in short range distance and LoS scenario, its possible to extend this for further scenario and others THz channel phenomena.

References

[1] Elayan H, Amin O, Shubair RM, Alouini M-S. Terahertz communication: The opportunities of wireless technology beyond 5G. 2018 International Conference on Advanced Communication Technologies and Networking (CommNet). 2018.

[2] Moldovan A, Kisseleff S, Akyildiz I.F, and Gerstacker W.H. Data Rate Maximization for Terahertz Communication Systems using Finite Alphabets. IEEE ICC 2016 - Wireless Communications Symposium Data, 2016; pp. 388-392

[3] J. Ma, R. Shrestha, L. Moeller, and D. M. Mittleman. Invited Article: Channel performance for indoor and outdoor terahertz wireless links, APL Photonics, 3(5), 2018; p. 051601.

[4] Anamaria Moldovan, Michael A. Ruder, Ian F. Akyildiz, and Wolfgang H. Gerstacker. LOS and NLOS Channel Modeling for Terahertz Wireless Communication with Scattered Rays. Globecom 2014 Workshop - Mobile Communications in Higher Frequency Bands

[5] V. Petrov, J. Kokkoniemi, D. Moltchanov, J. Lehtomäki, Y. Koucheryavy, and M. Juntti, "Last Meter Indoor Terahertz Wireless Access: Performance Insights and Implementation Roadmap."

[6] I. F. Akyildiz, C. Han, and S. Nie, "Combating the Distance Problem in the Millimeter Wave and Terahertz Frequency Bands," IEEE Communication Magazine, 2018.

[7] Y. Choi, "Performances and Feasibility of THz Indoor Communication for Multi-Gigabit Transmission," 2013.

[8] S. Hisatake and T. Nagatsuma, Nonpolarimetric Technique for Homodyne-Type Electrooptic Field Detection, Appl. Phys. Express 5, 012701, 2012.

[9] S. Hisatake, J. Y. Kim, K. Ajito, and T. Nagatsuma, Precise Phase Measurement of Continuous Terahertz-wave Based on Balanced Self-heterodyne Technique and its Application to Phase-contrast Imaging. J. Light. Technol. 32, 3683, 2014.

[10] H. H. N. Pham, S. Hisatake, I. V. Minin, O. V. Minin, and T. Nagatsuma, Exploit Terajet Generated from Dielectric Cuboid to Enhance Spatial Resolution of THz Imaging System, JSAP-OSA Joint Symposia 2017 Abstracts, Optical Society of America 2017.

[11] Shintaro Hisatake et al, Visualization of frequency-modulated electric field based on photonic frequency tracking in asynchronous electro-optic measurement system 2018 Appl. Phys. Express 11 046601.

[12] H. Arisesa and S. Hisatake, Experimental investigation of wave-packet propagation in terahertz frequency region, Applied Physics Letters, Vol. 12, No.19, 2019.

Interference Voltage Measurement Set-up for Beam-Type WPT Using an Electro-Optic Converter for Active Implantable Medical Device EMI Assessment

Suzune ITO †, Jintao SUN †, Takashi HIKAGE †, Junji HIAGASHIYAMA ‡, and Teruo ONISHI ‡

† Graduate School of Information Science and Technology, Hokkaido University
Kita14, Nishi9, Kita-ku, Sapporo, Hokkaido, 060-0814 Japan
‡ NTT DOCOMO, INC.
3-6 Hikarinooka, Yokosuka-shi, Kanagawa, 239-8536 Japan
E-mail: hikage@wtemc.ist.hokudai.ac.jp

Abstract – In order to estimate electromagnetic interference (EMI) characteristics on active implantable medical device (AIMD: implantable cardiac pacemaker / implantable cardioverter defibrillator), we developed novel measurement set-up for interference voltage of AIMD using an direct modulated Electrical to Optical (EO) converter embedded in a pacemaker mock-up that had connected actual pacemaker leads. Then interference voltage measurements in RF frequency band for beam type wireless power transfer (RF-WPT) were conducted using the measurement set-up.

Keywords – Active implantable medical device EMI; Electro to optic conversion; Wireless power transfer

1. Introduction

Wireless devices such as mobile phones, RFIDs, and wireless power transfer (WPT) systems are essential devices to realize the ubiquitous and universal network society. These devices emit electromagnetic fields (EMF) that could potentially cause electromagnetic interference (EMI) for other electromagnetic devices.

The EMI on active implantable medical devices (AIMDs) such as implantable-cardiac pacemakers and cardioverter defibrillators (ICDs) is one of the most important issues needing investigations [1-4]. This is because the number of AIMD users is increasing every year due to the aging of the population.

In this paper, we develop an interference voltage sensor for AIMD-EMI assessment by using direct modulated Electrical to Optical (EO) converter. Furthermore, measurements of interference voltage of a pacemaker in RF frequency band for beam type wireless power transfer (RF-WPT) using the measurement set-up are demonstrated.

2. Interference voltage sensor using an Electro-Optic converter for AIMD-EMI assessment

EMI impacts pacemakers/ICDs when the sensing circuit of the pacemakers receives a signal similar to “an electrocardiogram signal” or “noise,” and the signals’ strength is higher than the sensing threshold level of the pacemaker/ICD. The induced voltage on internal circuit of the pacemaker/ICD by the received external signal is defined as “interference voltage”. If the interference voltage exceeds the pacemaker's/ICD’s sensing threshold level, it may occur malfunction. In order to assess the pacemaker/ICD EMI from RF/EMF emitters, human torso phantom (Figure 1) has been used [4]. The torso phantom is comprised of a saline tank and electrodes. The saline tank is constructed from acrylic panels and is filled with a saline solution, with the density of 1.8 g/l NaCl concentration. Pacemaker is placed in the saline during the EMI assessment test in order to operate properly as is implanted in human body.

It is very difficult to obtain actual induced interference voltage on the internal circuit inside the pacemaker’s enclosure (CAN) by measurement. Here, we develop a novel interference voltage sensor by installing small-sized EO converter [5, 6] in the pacemaker CAN with a perfect waterproof structure. Figure 1 shows configuration of the developed interference voltage sensor. This sensor can be connected an actual pacemaker lead in uni-polar mode and can measure induced voltage without disturbing electromagnetic fields because I/O signal of the sensor are made through optical fiber. The input impedance of the sensor is 50 Ω, and the minimum sensitivity is approximately -80 dBm. Actually, this sensor can be used in frequency range from 100 kHz to 6 GHz.

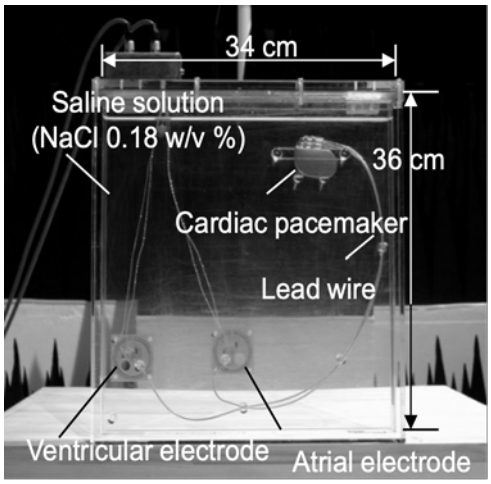

Figure 1 Torso phantom for AIMD-EMI assessment.

3. Measurement of interference voltage due to a cellular base-station antenna

In one example, we measured interference voltage due to RF-WPT base-station emitting 900 MHz band RF wave using the developed sensor placed into the torso-phantom. Figures 3 and 4 show constructed measurement-setup and measured distance dependence of interference voltage, respectively. The interference voltages were measured when the RF-WPT operating at 915 MHz both in vertical and horizontal polarization under near-field exposure condition. Measured results confirmed the developed sensor can obtain interference voltage precisely.

4. Conclusions

Novel interference voltage sensor for AIMD-EMI assessment was developed by applying direct modulated EO converter and constructed a measurement set-up. This is first report that demonstrates measurements of interference voltage in RF-WPT frequency band. In the future, the developed set-up can be applied for other wireless systems.

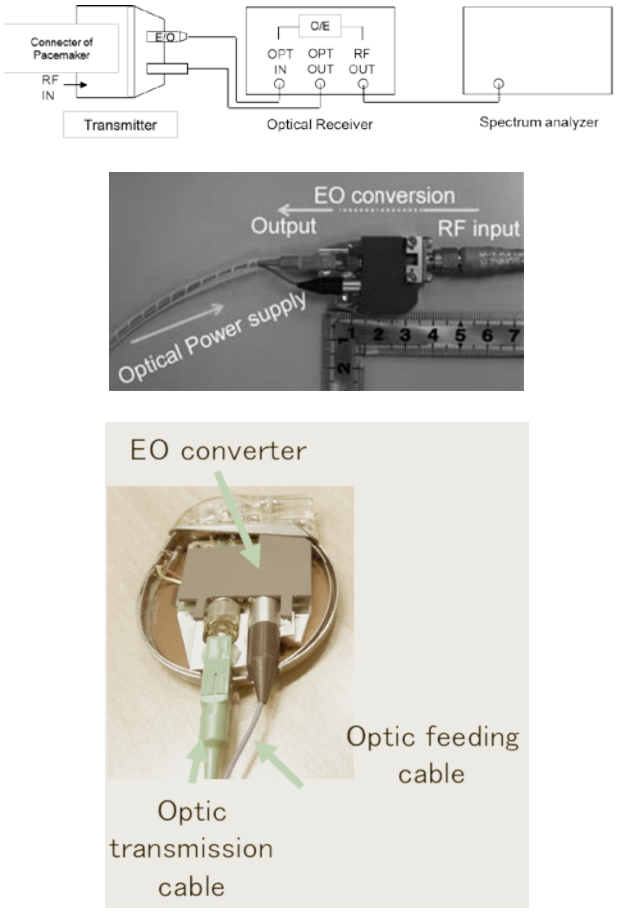

Figure 2 Electrical to Optical (EO) converter and developed interference voltage sensor.

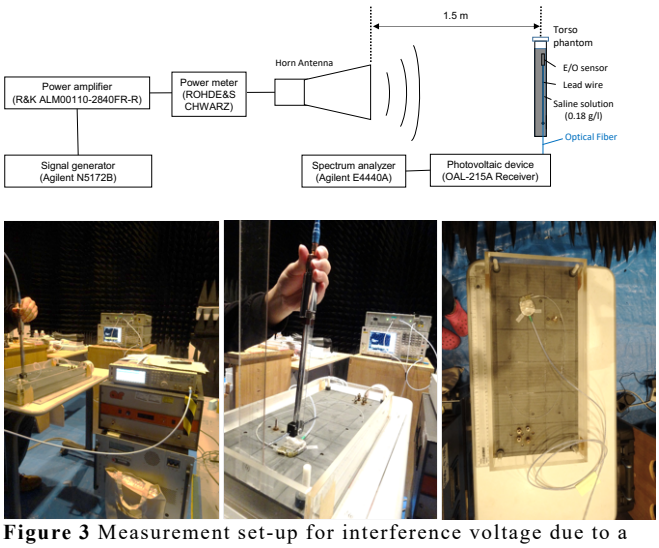

Figure 3 Measurement set-up for interference voltage due to a RF frequency band for beam type wireless power transfer (RF-WPT).

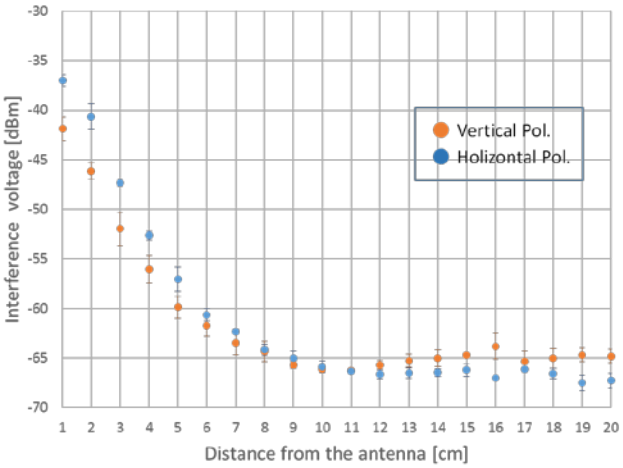

Figure 4 Measured distance dependence of interference voltage at RF-WPT frequency (915 MHz)

Acknowledgement

This work was partially supported by Grant-in-Aid for Japan Society for the Promotion of Science (JSPS) KAKENHI Grant Number JP 19K04504.

References

[1] W. Irnich, L. Batz, R. Muller and R. Tobisch, “Electromagnetic interference of pacemakers by mobile phones,” J. Pacing and Clinical Electrophysiology, vol. 19, no. 10, pp.1431-1446, Oct. 1996.

[2] D. L. Hayes, P. J. Wang, D. W. Reynolds, M. Estes III, J. L. Griffith, R. A. Steffens, G. L. Carlo, G. K. Findlay and C. M. Johnson, “Interference with cardiac pacemakers by cellular telephones,” New Engl. J. Med., vol. 336, no. 21, pp. 1473-1479, May 1997.

[3] T. Toyoshima, M. Tsumura, T. Nojima and Y. Tarusawa, “Electromagnetic interference of implantable cardiac pacemakers by portable telephones,” Japanese J. Cardiac Pacing and Electro-physiology, vol. 12, no.5, pp. 488-497, 1996.

[4] “Guidelines on the use of radio communications equipment for implanted medical devices,” Ministry of Internal Affairs and Communication of Japan, Aug. 2005.

[5] T. ONISHI, S. ISHIHARA, and J. HIGASHIYAMA,” Electromagnetic Field Measurement Using the Directly Modulated Electrical to Optical Conversion,” IEICE Tech. report, PEM2014-15, Feb. 2015. (In Japanese)

[6] Naoki TANAKA, Takashi HIKAGE, Toshio NOJIMA, Takahiro IYAMA, Junji HIAGASHIYAMA, and Teruo ONISHI,” Novel Interference Voltage Sensor Using an Electro-Optic Converter for Active Implantable Medical Devices EMI Assessment,” proc. of First PEM International Workshop in Kyoto, FCA-8, pp.1-2, Nov. 2015.

Measurement of Microwave Field Distribution Propagating along FRPM Pipe-Wall Using Electro-Optic Sensor for Non-Destructive Inspection

Yoshihiro NISHIMURA[1], Kosuke YOSHIDA[1], Sayaka MATSUKAWA[1,2], Tadahiro OKUDA[3], Masaya HAZAMA[3], Satoru KUROKAWA[2], and Hiroshi MURATA[1*]

[1] Graduate School of Engineering, Mie University. Tsu-City, Mie 514-8507 Japan.
[2]National Institute of Advanced Industrial Science and Technology. Tsukuba, Ibaraki 305-8563 Japan.
[3]Kurimoto Limited. Higashi-Ohmi, Shiga 527-0108 Japan.
*murata@elec.mie-u.ac.jp

Abstract – We have proposed and developed a new non-destructive inspection method for buried fiber-reinforced plastic mortal (FRPM) pipelines utilizing microwave guided modes propagating along the FRPM pipe-wall. In this paper, we report detailed measurement results of the change in the microwave field distributions caused by a foreign object located at the other side of the wall. By utilizing a small invasive electro-optic sensor, clear field distribution change according to object materials are identified.

Keywords – microwave; electro-optic sensor; guided-mode; nondestructive inspection

1. Introduction

A microwave (MW)/millimeter-wave (MMW) sensor using electro-optic (EO) effect, which is usually called as and EO sensor, is suitable for invasive electro-magnetic field sensing in MW/MMW frequency ranges, since it can be composed of non-metal or minute metal elements and can be operated without external power supply. In addition, measured signals can be transferred by use of not a metal cable but an invasive optical fiber cable. Therefore, almost ideal field measurement of high accuracy with little invasiveness are obtainable by use of an EO sensor; this is important in many MW/MMW field measurement applications [1], [2].

A fiberglass-reinforced plastic mortar (FRPM) pipe has high mechanical strength and high chemical corrosion resistance as well as being lightweight compared to a metal or mortal pipe. Therefore, a FRPM pipe is widely used in many application fields such as protecting tubes for electric power/optical fiber cables, sewer pipes and agricultural water pipes. Especially, the total length of the FRPM pipelines used for agricultural water supply is approximately 40,000 km in Japan. Therefore, an easy-to-use nondestructive inspection method for FRPM pipelines is required for regular testing and maintenance.

There are several candidates for the inspection method for FRPM pipelines: magnetic resonance imaging (MRI), X-ray and ultrasonic waves [3], [4]. However, these methods are unsuitable for inspection of long and underground FRPM pipelines, since they require rather large and specific measurement machines. Therefore, there is no effective inspection method for long FRPM pipelines yet, as far as we know.

We have found that FRPM is a dielectric material with relatively small loss in the MW frequency range of 1~10 GHz and that an underground FRPM pipe can be a cylindrical-shaped dielectric waveguide for MW with a relatively low propagation loss [5]. By utilizing these interesting characteristics, we have proposed a new inspection method for FRPM pipelines [6], [7]; the MW guided-modes are excited by use of appropriate antennas installed at the connection joint in the pipeline, and the transmission characteristics of the MW guided-modes are to be measured by use of

an EO sensor or a small probe precisely. If a defect, crack or foreign object is in/on the FRPM pipe wall of a buried pipeline, the MW guided-mode propagation is disturbed, which leads to MW scattering into inner/outer spaces or coupling between guided-modes.

In this paper, we report detailed measurement results of the MW guided-mode field distributions along the FRPM pipe-wall surface when a foreign object is located on the other surface of the pipe wall. By use of an invasive EO sensor, evanescent field changes can be measured precisely. We found that the MW evanescent field on the surface of the FRPM is disturbed by a foreign object and that the disturbed profiles were dependent on the object material.

2. Experimental Set-up

The experimental set-up is shown in Fig. 1 (a). The FRPM pipe used in the experiment was 1,000 mm long, 18 mm thick, and with an inner diameter of 250 mm. Microwave signals in the frequency range from 2.2 to 3.0 GHz were supplied from a network analyzer to a dipole antenna (commercially available sleeve dipole antenna of 50 mm long), and were coupled to the TE_{10} guided-mode propagating along the FRPM pipe wall.

On the surface of the inner wall of the FRPM pipe, a small object (typically 40 mm x 40 mm, 450 mm apart from the end of the pipe) was attached as a foreign object as shown in Fig. 1 (b), which disturbs the TE_{10} guide-mode propagation since the evanescent field of the guided-mode was overlapped with the object. The wave-guiding phenomena is based on a MW standing-wave resonance in the cross section. Therefore, the disturbance of the resonance condition of the MW guided-mode caused by the object on the inner surface can be observed from the other surface of the FRPM pipe (the outer surface) if we can measure the outer surface MW field with an invasive measurement technique. Then, we adopted an invasive EO sensor (SEIKO GIKEN Co. Ltd. CS-1210) and scanned it on the outer surface of the FRPM pipe along the *x*- and *y*-directions to measure the disturbance effect by the attached object.

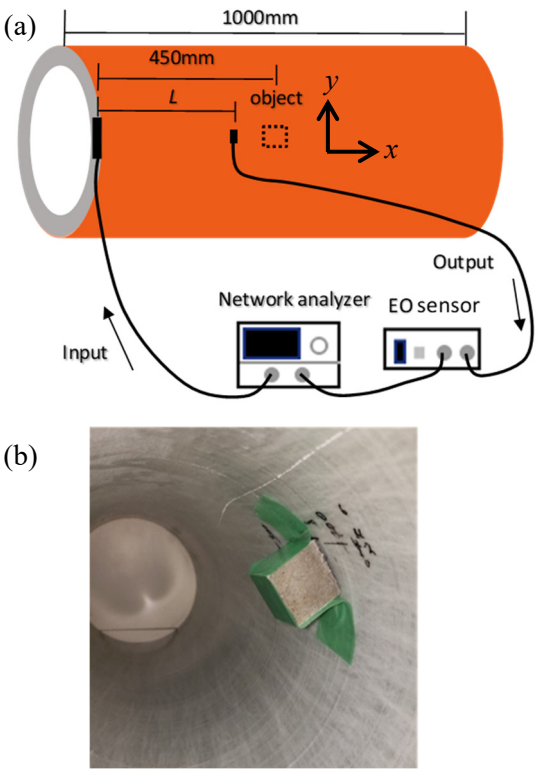

Figure 1. (a) Experimental set-up. (b) A photograph of the FRPM pipe inner surface attached with a foreign object (concrete block).

3. Measured Results

Figure 2 shows typical examples of the two-dimensional MW intensity distributions measured by use of the EO sensor on the outer surface. Clear differences in the MW intensity distribution according to the object materials (metal, concrete, and Teflon) were observed.

The slight decay of the MW intensity along the *x*-direction in the case of no object (Fig. 2 (a)) indicates the propagation loss of the TE_{10} guided-mode.

In the case of the metal (Al) plate of 40 mm x 40 mm, the MW reflection by the metal plate can be identified, and the MW intensity was rather decreased after the metal plate, as shown in Fig. 2 (b).

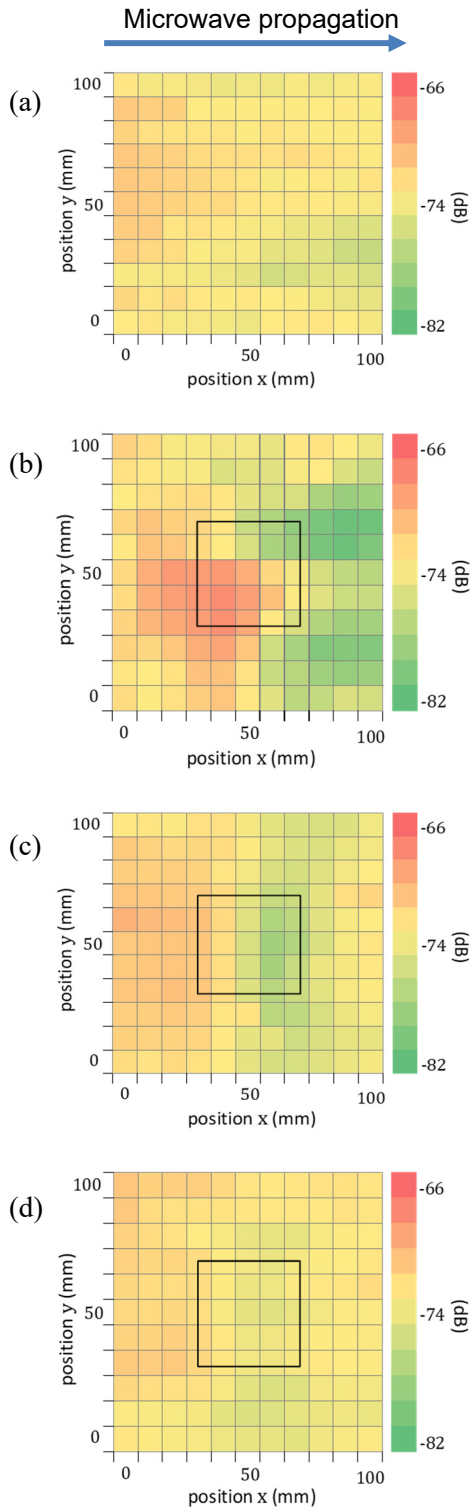

Figure 2. Measured MW intensity distributions on the outer surface measured by use of the EO sensor.
(a) No object. (b) 40mm x40mm metal (Al) plate. (c) 40mmx40mm concrete block. (d) 40mmx40mm Teflon block. The black square lines indicate the position of the objects.

In the case of the concrete block of 40 mm x 40 mm, the MW intensity was distorted as shown in Fig. 2 (c). However, the distortion by the concrete was smaller than the metal case.

In the case of the Teflon block of 40 mm x 40 mm, the MW distortion was still smaller than the concrete as shown in Fig. 2 (d), which is due to the small dielectric constant value of Teflon ($\varepsilon_r \sim 2$) compared to the concrete ($\varepsilon_r \sim 5$).

Figure 3 shows the detailed comparison of the measured MW intensity distributions of the 4-cases (no object, metal, concrete, and Teflon) along the line of $y = 50$ mm in Fig. 2. The MW reflection can be identified clearly for the metal case, while the dielectric block cases (concrete and Teflon) show the field decay by the dielectric blocks, but the field intensities were recovered after passing the block. These results are due to the transitory enhancement of the MW field confinement effect to the inner region by the attached dielectric blocks between $x = 30$ mm and $x = 70$ mm. However, passing through the block-attached region, the MW field confinement effect returned to the initial condition and the MW field distributions went back to the initial TE_{10} mode profile again.

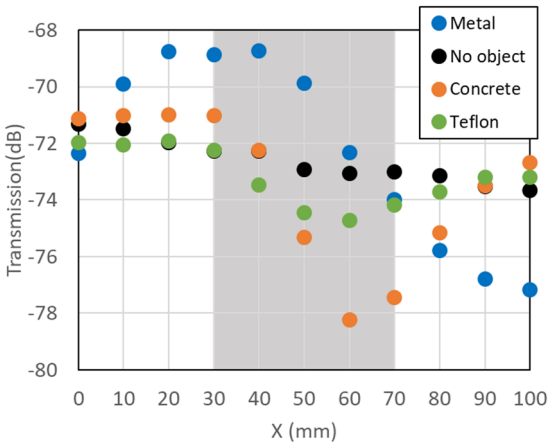

Figure 3. Comparison of the MW intensity changes along the line of $y = 50$ mm. The objects (metal, concrete, and Teflon) were located at the position from $x = 30$ mm to 70 mm (gray colored region).

4. Conclusios

We also measured the MW intensity distributions by changing the size of the attached object with the same way, and obtained appropriate results corresponding to the size of the object.

These results are useful for the nondestructive inspection/diagnosis using MW guided-modes for underground FRPM pipelines in frequency and time domains.

The results shown in Figs. 3 and 4 are the measured MW field intensities. Other important information can be obtained by use of the change in the phase of MW electric field. Especially, for dielectric object cases, phase change information can be a powerful technique to identify object materials and its size, although precise phase measurement might be not so easy in the actual underground pipeline cases.

References

[1] T H. Togo, S. Mochizuki, and N. Kukutsu. "Optical fiber electric field sensor for antenna measurement," *NTT Technical Review*, **vol.7**, no.3, March 2009.

[2] H. Togo, N. Shimizu, and T. Nagatsuma, "Tip-on-fiber Electro-optic Probe for Near-field Measurement," *NTT Technical Review*, **vol.4**, no.1, Jan. 2006.

[3] E. Marfisi, C. J. Burgoyne, L. D. Hall, and M. H. G. Amin, "Use of the MRI technique to study concrete and FRP reinforced concrete behavior," Research Leading to the Development of Design Guideline for the Use of FRP in Concrete Structure – *2nd ConFiberCrete Young Researcher Conference*, Corfu, Greece, June 2002.

[4] M. J. S. Lowe, D. N. Alleyne, P. Cawley, "Defect detection in pipes using guided waves," *Ultasonics*, vol. 36, pp. 147-154, 1998.

[5] F. Ueno, H. Murata, T. Okuda, M. Hazama, and Y. Okamura, "New Nondestructive Measurement for Fiberglass-Reinforced Plastic Mortar Pipes Using Microwave and Photonic Techniques," *MWP/APMP 2014*, TuED-2, Sapporo, Japan, Oct. 2014

[6] Y. Azuma, F. Ueno, H. Murata, Y. Okamura, T. Okuda, and M. Hazama, "Precise Measurement of Microwave Evanescent Fields along Fiberglass-Reinforced Plastic Mortar Pipe Using Electro-Optic Sensor for Nondestructive Inspection," *OECC/PS 2016*, WA2-73, July, 2016.

[7] H. Murata, T. Okuda and M. Hazama, "Nondestructive Infrastructure Measurement Using Microwave Guided-Mode Propagation and Reflection along Fiber-Reinforced Plastic Mortal Pipe Wall in Underground Pipeline," *2018 IEEE Conference on Antenna Measurements and Applications (2018 IEEE CAMA),* 57.2, September 2018, Vasteras, Sweden.

Heterodyne Detection of THz Waves by Electro-Optic Sampling Using a Modulator-Based Optical Comb Source Toward Frequency Stabilization of THz Sources

Isao MOROHASHI*, Norihiko SEKINE, Akifumi KASAMATSU and Iwao HOSAKO
National Institute of Information and Communications Technology, 184-8795 Tokyo, Japan
*Corresponding author: morohashi@nict.go.jp

Abstract – Heterodyne detection of continuous terahertz (THz) waves by electro-optic (EO) sampling using a Mach-Zehnder-modulator-based flat comb generator (MZ-FCG) was reported. The proposed THz frequency measurement system has high accuracy in frequency due to that of the MZ-FCG. For phase-locking of THz sources, detection of THz waves from the Gunn oscillator under a free-running condition has been demonstrated.

Keywords – terahertz wave; electro-optic sampling; optical comb

1. Introduction

Terahertz (THz) wave sources emitting radiations with high frequency precision are important for applications such as wireless communications and high-resolution gas sensing. Although a conventional method of measuring the THz frequency is to use frequency mixers, it needs to individually prepare mixer devices covering the frequency bands of interest due to the limited bandwidth of the mixers. On the other hand, electro-optic (EO) sampling, photonics-based THz detection schemes, is generally used to measure the temporal profile of THz pulses using optical short pulses. Recently, it has been demonstrated frequency measurement of continuous THz waves by the EO sampling method using optical combs [1]. This method is based on optical heterodyne, where optical combs are used as the local oscillator and an EO crystal acts as the mixer. In this method, the frequency accuracy strongly depends on that of the comb source, so that the frequency stability in the comb source is important. A Mach-Zehnder-modulator-based flat comb generator (MZ-FCG) can easily generate optical combs with a high accuracy in the mode spacing, in contrast to mode-locked lasers which need to be stabilized the mode spacing by phase locked loops [2]. By using the MZ-FCG, highly accurate THz frequency measurement has been carried out. In this paper, we report on detection of continuous THz waves by EO sampling using the MZ-FCG toward frequency stabilization of THz sources.

2. Experiments

Figure 1 shows the experimental setup. Optical combs with a 10 GHz spacing and a 300 GHz bandwidth generated by the MZ-FCG were mixed with THz waves on an EO

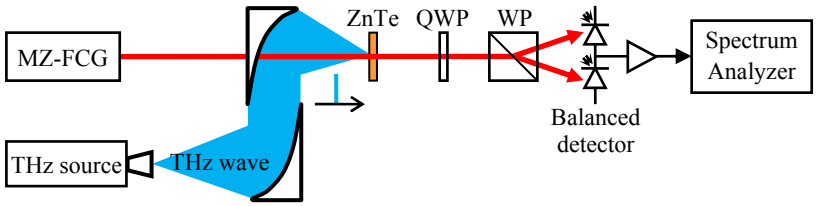

Figure 1. The experimental setup for heterodyne detection of THz waves. For the THz source, a Gunn oscillator and a frequency multiplier were used. QWP: quarter-wave plate, WP: Wollaston prism.

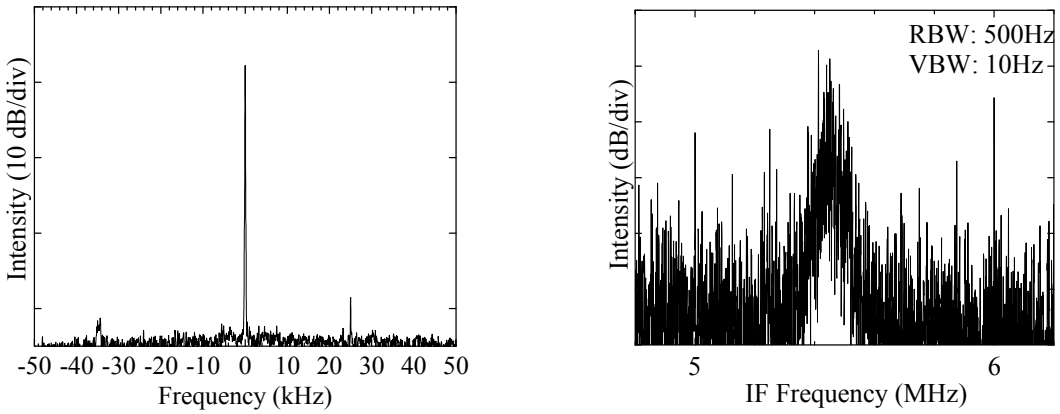

Figure 2. Spectra of THz waves emitted from (a) the frequency multiplier and (b) the Gunn oscillator under a free-running condition.

crystal (ZnTe). In this measurement we used two types of THz source sources: One is a frequency multiplier to evaluate the performance of the heterodyne detection system; the other is a Gunn oscillator operating at 104 GHz for frequency stabilization. By detecting the optical comb passed through the EO crystal using a balanced photodetector and a spectrum analyzer (SA), spectra of THz waves are observed. Figure 2 shows spectra of detected THz waves. Figure 2(a) shows a spectrum of a THz wave emitted from the frequency multiplier. A very sharp line was observed, in which the linewidth was less than 1 Hz. This result implies that our system has high accuracy in frequency caused by that of the MZ-FCG. Figure 2(b) shows a spectrum of a THz wave radiation from the Gunn oscillator under a free-running condition. The linewidth was few kHz and the signal-to-noise ratio (SNR) reduced by about 30 dB compared with the frequency-locked condition. In order to use this signal for phase-locking of the Gunn oscillator, SNR is required to exceed 10 dB. One possible way to improve the SNR is to use second harmonic generation of the optical comb. The detection sensitivity in the case using the 800 nm range is at least 10 times higher than that using the 1550 nm range.

3. Conclusions

Heterodyne detection of CW-THz waves by EO sampling using the MZ-FCG was reported. The proposed THz frequency measurement system has high accuracy in frequency due to that of the MZ-FCG. For phase-locking of THz sources, detection of THz waves from the Gunn oscillator under a free-running condition has been demonstrated.

Acknowledgements

This research is partly supported by JSPS KAKENHI Grant Number JP17K05092.

References

[1] Morohashi I, Katayama I, Kirigaya M, Irimajiri Y, Sekine N, Hosako I. High precision frequency measurement of terahertz waves using optical combs from a Mach–Zehnder-modulator-based flat comb generator. Opt. Lett. 2019; 44(3): 487–490.

[2] Morohashi I, Sakamoto T, Sekine N, Kasamatsu A, Hosako I. Ultrashort optical pulse source using Mach–Zehnder-modulator-based flat comb generator. Nano Commun. Netw. 2016; 10: 79–84.

Port extender for vector network analyzer using bi-directional optical transceiver up to 20 GHz

Satoru KUROKAWA*, Masanobu, HIROSE, Michitaka AMEYA and Sayaka MATSUKAWA
National metrology institute of Japan, National Institute of Advanced Industrial Science and Technology,
Tsukuba, Ibaraki, Japan
satoru-kurokawa@aist.go.jp

Abstract – We developed a port extender for vector network analyzer (VNA) using optical fiber link transceiver. Our developed system consists of zero-biased electro absorption optical modulator, photo-biased photo diode, single-mode optical fiber and microwave directional coupler. Our developed system can measure S-parameters in full 2-port calibration of VNA up to 20 GHz. In this paper, we show frequency performance of the system and reflection coefficient (S_{11}) measurement results of double ridged guide horn antenna from 1 to 20 GHz.

Keywords – antenna measurement; optical fiber link, photodiode, electro absorption intensity modulator

1. Introduction

We have already developed a microwave receiving system using an optical reflection type zero-biased optical absorption modulator (EAM), a super luminescent diode (SLD) and a photo biased photo diode (PD) [1][2]. To evaluate reflection coefficient of an antenna under test (AUT), we have already developed a port extender for VNA from 20 to 40 GHz [3] that mainly for 5th generation mobile communication high frequency band [4]. For evaluating antenna parameters for low frequency 5th generation mobile communication, we newly developed a port extender for VNA from 1 to 20 GHz. At first, we explain our port extender for VNA. Then, we explain the frequency performance of the system and a reflection coefficient (S_{11}) for double ridged guide horn antenna (DRGH) [5].

2. Outline of our proposed system

A. *System configulation*

Our proposed system consists of microwave directional coupler 87301D [6] of keysight Inc., two optical fiber link modules [3] with vector network analyzer. Our optical fiber link module as a receiving module consists of zero biased optical reflection type electro absorptive intensity modulator (EAM), single mode optical fiber, a uni-traveling carrier photo photodiode (UTC-PD) [7] with two ZVA-430GX microwave amplifiers of Mini-circuits Inc. [8]. Our optical fiber link module as a transmitting module consists of a photo biased photodiode (PD) with two ZVA-430GX microwave amplifiers and EAM. EAM for the transmitting module connects to the source output port 2 of VNA. UTC-PD with microwave amplifiers for receiving module connects to B-channel of port 2 of VNA. Our using EAM and photo biased PD can use for microwave measurement without thermo-electric cooler (TEC) and DC bias. In the case of using our proposed module for port 2 and a coaxial cable for port 1, the system can measure S-parameters for device under test (DUT) in full 2-port calibration of VNA. Fig. 1 shows outline of the system with VNA. Fig. 2 shows frequency response of the optical fiber link module. [EA - PD] in Fig. 2 indicates a measured frequency response using EAM alone and PD alone. [EA - PD+ZVA430GX] indicates show a measured frequency response using EAM alone and PD with two ZVA430GX microwave amplifiers.

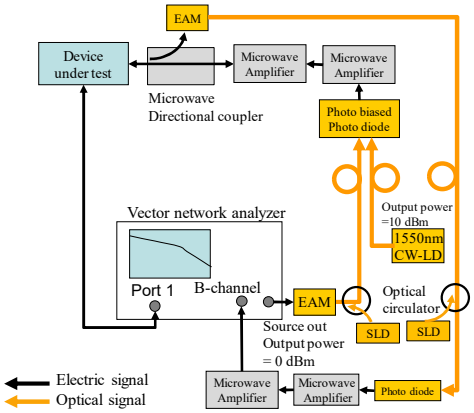

Fig. 1 Our developed port extender of VNA

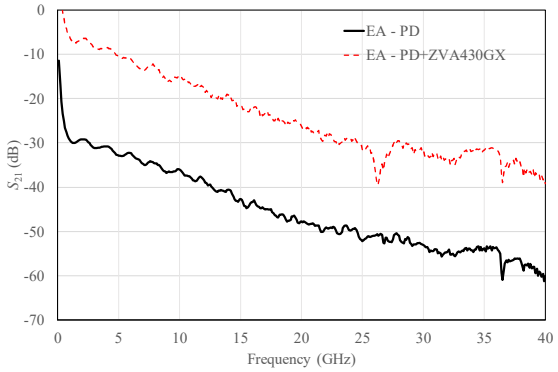

Fig. 2 Frequency response of our developed port extender of VNA

B. Frequency characteristics of the system

For evaluating dynamic range of the system, we show measured results of *S*-parameters for step attenuator 84905M of keysight Inc. [9] with a 10 dB fixed attenuator for input port and output port of step attenuator. Our using *S*-parameters measurement setup consists of a 30 cm coaxial cable for port1, our developed port extender of VNA for port 2. Using this setup, we can measure transmission coefficients (S_{21} and S_{12}) and refection coefficients (S_{11} and S_{22}) of DUT in full 2-port calibration of VNA. Fig. 3 shows a dynamic range measurement setup for the system. Fig. 4, 5, 6 and 7 show measurement results of S_{11}s, S_{21}s, S_{12}s and S_{22}s, respectively. Measured S_{21}s show transmission coefficient and dynamic range of the system that for the optical fiber link receiving modules of port extender and transmitting coaxial cable with VNA. Measured S_{12}s show transmission coefficient and dynamic of the system that for the receiving coaxial cable and optical fiber link transmitting modules of port extender with VNA. [x dB] indicates attenuation level for the step attenuator. Fig. 5 shows the fact that our system with VNA has more than 50 dB dynamic range for the receiving module of the port extender in the frequency range from 1 to 20 GHz. Fig. 6 shows the fact that our system with VNA has more than 70 dB dynamic for the transmitting module of the port extender from 1 to 20 GHz. Fig. 4 and 7 show the fact that our system with VNA can measure reflection coefficients of DUT from 1 to 20 GHz. Fig. 8 and 9 show estimated linearity of S_{21} and S_{12} for the system with VNA. Fig. 8 shows the fact that the system for receiving optical fiber link of port extender with VNA has less than 0.35 dB deviation for 50 dB attenuation and less than 0.1 dB deviation for 40 dB in the frequency range from 1 to 20 GHz. Fig. 9 shows the fact that the system with VNA has less than 0.15 dB deviation for 50 dB attenuation and less than 0.05 dB deviation for 40 dB attenuation in the frequency range from 1 to 20 GHz. We show the fact that our proposed system can measure s-parameters of DUT in the frequency range from 1 GHz to 20 GHz with less than 0.35 dB deviation and 50 dB dynamic range.

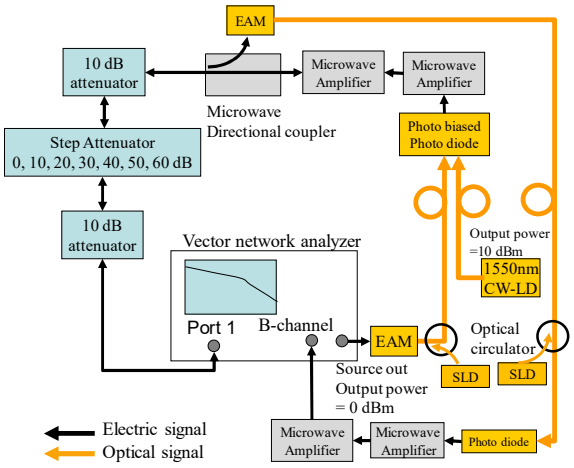

Fig. 3 Dynamic range measurement setup

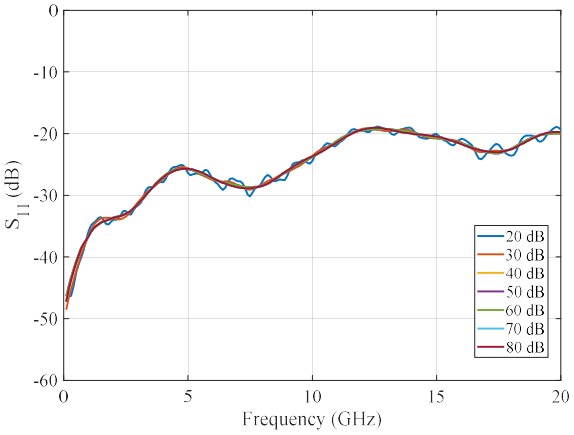

Fig. 4 Measured S_{11} magnitude for Step attenuator with 10 dB fixed attenuators

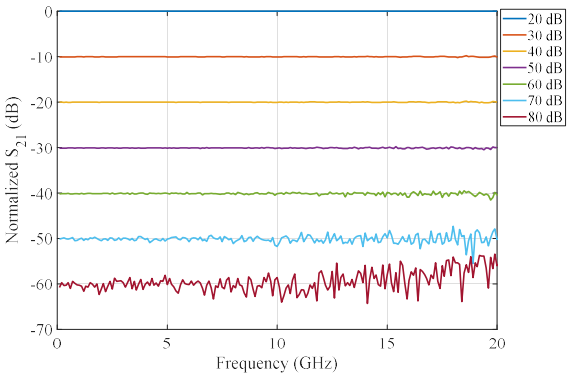

Fig. 5 Dynamic range of S_{21} magnitude

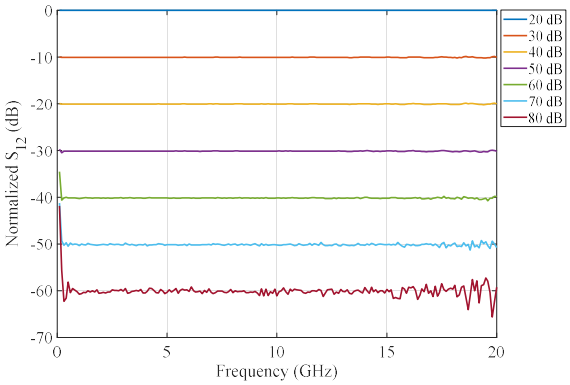

Fig. 6 Dynamic range of S_{12} magnitude

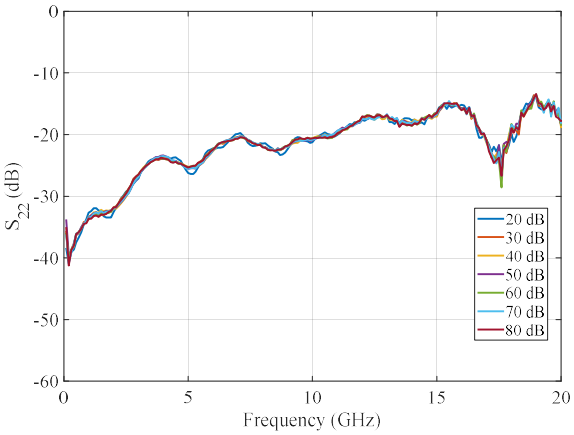

Fig. 7 Measured S_{22} magnitude for Step attenuator with 10 dB fixed attenuators

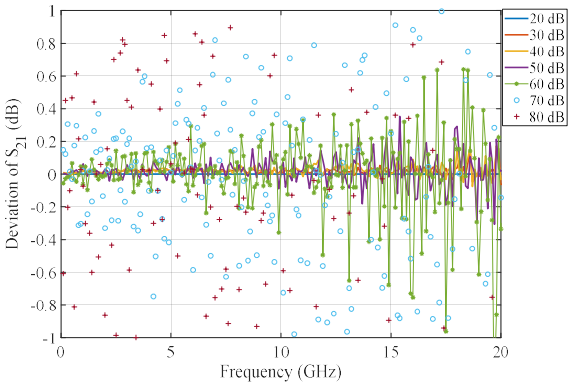

Fig. 8 Linearity of S_{21} magnitude

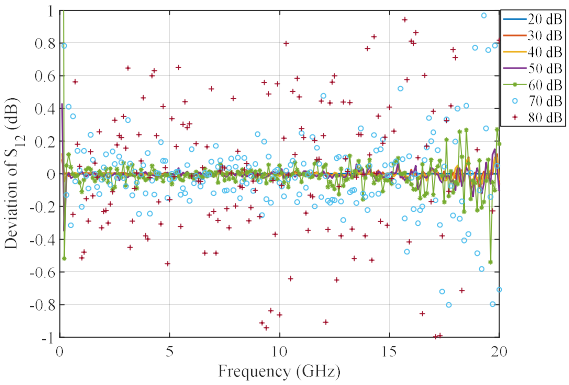

Fig. 9 Linearity of S_{12} magnitude

3. Reflection coefficient measurement for double ridged guide horn antenna

To validate our developed port extender, we demonstrate the reflection coefficient (S_{11}) measurement for a 3115 double ridged guide horn antenna of ETS-Lindgren Inc. as an antenna under test (AUT).

Fig. 10 shows the measurement setup for S_{11} measurement using the port extender with VNA. Fig. 11 and 12 show the measured results of S_{11} magnitude and S_{11} phase for the antenna using our system and using 30 cm coaxial cable as a receiving cable in 1-port open-short-load calibration, respectively. Measured S_{11} magnitude and S_{11} phase for the antenna have good agreement in the frequency range from 1 to 20 GHz. These results show the fact that our developed port extender with VNA can measure refection coefficient of antennas.

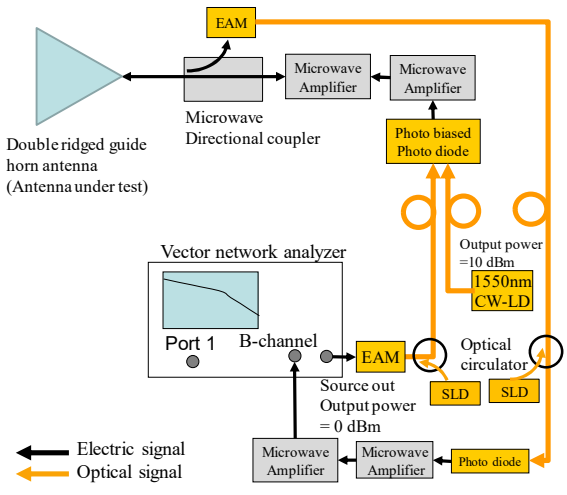

Fig. 10 Measurement setup for reflection coefficient measurement

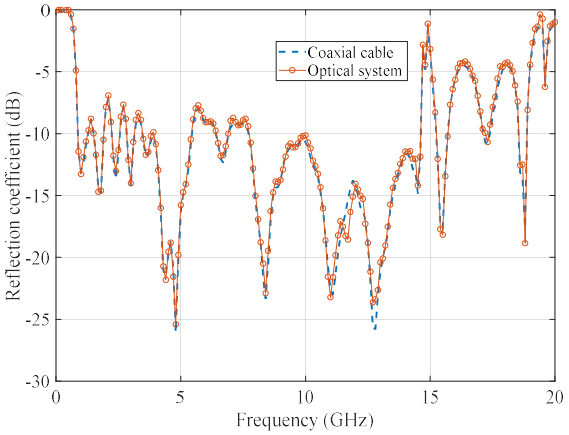

Fig. 11 Measured S_{11} magnitude of DRGH

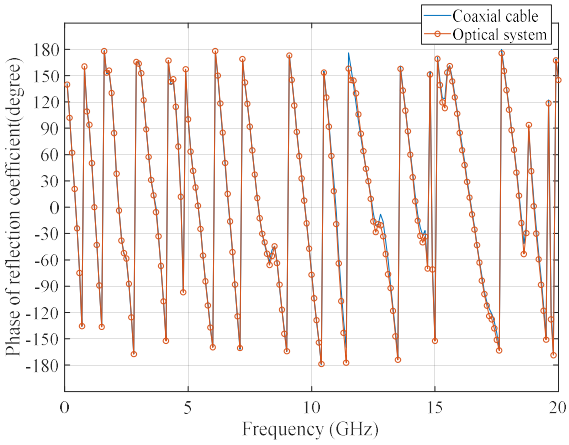

Fig. 12 Measured S_{11} phase of DRGH

4. Conclusion

We have proposed the optical fiber link port extender for VNA. Our proposed system can measure reflection coefficient and transmission coefficient of the antenna under test. Our proposed optical fiber link system can measure antenna characteristics in the frequency range from 1 to 20 GHz.

Further, we demonstrate the antenna reflection coefficient measurement for double ridged guide horn antenna using our proposed system. We compare the measurement results with using our proposed optical system and using conventional coaxial cable system. We show the fact that our proposed system can measure reflection coefficient with good agreement for coaxial cable system from 1 to 20 GHz.

References

[1] S. Kurokawa, M. Hirose, “Microwave Receiving System for Antenna Measurement Using Optical Devices up to 40 GHz,” in Proc. of EuMW2017, Oct. 2017.

[2] S. Kurokawa, M. Hirose, “Microwave Receiving System Using Electro-Absorption Optical Modulator for Broadband Horn Antenna Calibration,” in Proc. of IEEE 2017CAMA, Oct. 2017.

[3] S. Kurokawa, M. Hirose, “Antenna Reflection Coefficient Measurement Using Bi-Directional Optical Fiber Link Transceiver up to 40 GHz,” in Proc. of EuCAP2018, March 2018.

[4] Leading towards Next Generation "5G" Mobile Services. Federal Communications Commission, https://www.fcc.gov/news-events/blog/2015/08/03/leading-towards-next-generation-5g-mobile-services.

[5] Double-Ridged Guide Antenna, ETS-lindgren Inc., http://www.ets-lindgren.com/3115

[6] Keysight Technologies, ``Technical overview of 87300B,C,D and 87301B,C,D,E Directional couplers,''Published in USA, January 7, 2019, 5091-6188E.pdf.

[7] T. Ishibashi, N. Shimizu, S. Kodama, H. Ito, T. Nagatsuma, and T. Furuta, Tech.. Dig. Ultrafast Electron. And Optoelectron, pp.166-169 (1997).

[8] Flat gain wideband amplifier ZVA-403GX+, Mini circuits Inc. https://www.minicircuits.com/pdfs/ZVA-403GX+.pdf

[9] Keysight Technologies, ``Product Overview 84904/5/8M Programmable Step Attenuators for Microwave and RF Manufacturing Test Systems'', Published in USA, December 2, 2017, 5988-2475EN.pdf

Wavelength Conversion between Terahertz wave and Infrared for frequency measurement

Shin'ichiro HAYASHI[1*], Seigo OHNO[2], and Norihiko SEKINE[1]
[1]Terahertz Technology Research Center, National Institute of Information and Communications Technology, 184-8794 Tokyo, Japan
[2]Department of Physics, Tohoku University, 980-8578 Sendai, Japan
*Corresponding author: hayashi@nict.go.jp

Abstract – We propose a wavelength conversation between terahertz wave and infrared using a nonlinear $LiNbO_3$ crystal for frequency measurement in the terahertz region. Nonlinear wavelength conversion techniques based on frequency stabilized infrared beams allow the spectra in the terahertz region to be determine their frequency. These are very promising for extending applied research into the terahertz region, and we expect that these will open up new research fields such as wireless information communications in the terahertz region.

Keywords – terahertz wave; wavelength conversion; nonlinear optics

1. Introduction

For more than twenty years, there has been remarkable growth in the field of terahertz frequency science and engineering, which has become a vibrant, international, cross-disciplinary research activity [1]. Wavelength conversion in nonlinear optical materials is an effective method for generating (down-conversion) and detecting (up-conversion) terahertz waves owing to the high conversion efficiency, wide tunability, bandwidth, and room temperature operation. The large figure of merit of lithium niobate ($LiNbO_3$) makes this well-known nonlinear crystal ideal for such an application; terahertz wave parametric wavelength conversion (between infrared and terahertz wave) is realized by stimulated polariton scattering via transverse optical phonons [2].

In this study, we propose a wavelength conversion between terahertz wave and infrared using a nonlinear magnesium oxide (MgO) doped $LiNbO_3$ crystal. The energy of one pumping photon split into two photons, a terahertz wave and a signal wave. When detecting the terahertz wave, mixing the terahertz wave with the intense pumping beam at the input region of the crystal, up-converted signal photons are created in difference-frequency mixing. Then, by injecting the terahertz wave satisfying non-collinear phase matching condition, the up-converted signal was seeded and parametrically amplified by the nonlinear MgO:$LiNbO_3$ optical parametric amplifier [3].

2. Experiment

In our experimental apparatus, shown in figure 1, the frequency of input terahertz wave is measured by the frequency up-conversion to the signal infrared beam with a frequency stabilized infrared beam. The frequency stabilized infrared beam is generated by the injection seeded optical parametric generator (is-OPG) pumped by a pulsed single-mode Nd:YAG laser based master oscillator and power amplifiers (MOPA) system. The seeding beam (continuous wave and narrow linewidth) passed through an optical fiber is locked to 1.55 μm as traceable to the national standard. The energy and intensity of frequency stabilized pumping beam were increased more than 10 mJ/pulse and 1 GW/cm^2. We used a 65-mm-long nonlinear MgO doped $LiNbO_3$ crystal with a high-resistivity Silicon prism as an efficient input coupler for the terahertz waves. The input terahertz wave is focused onto the MgO:$LiNbO_3$ crystal. The incident angle between the terahertz wave and the pumping beam satisfies the non-collinear phase-matching conditions in the MgO:$LiNbO_3$ crystal.

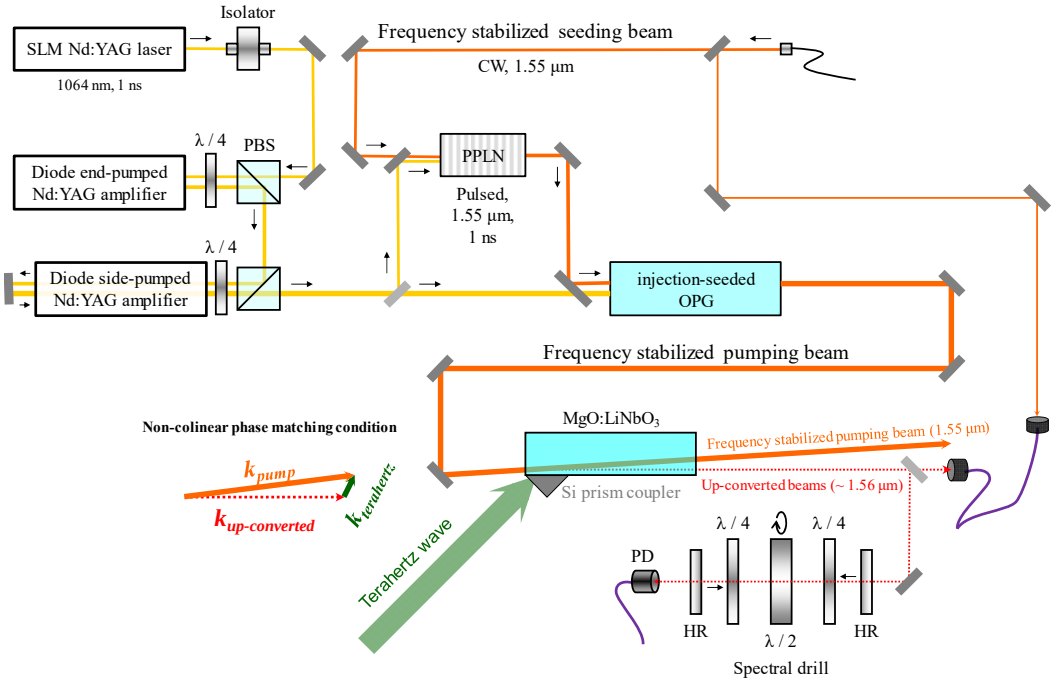

Figure 1. Experimental apparatus for frequency measurement of terahertz wave based on wavelength conversion.

Mixing the terahertz wave with the intense frequency stabilized pumping beam creates seeded up-converted (corresponding to the difference-frequency between the pumping beam and the terahertz wave) signals, which are parametrically amplified by the MgO:$LiNbO_3$ optical parametric amplifier. The up-converted signal is measured through a spectral drill [4]. The frequency of input terahertz wave is observed as intensity error signal.

Acknowledgement

The authors would like to thank Prof. Miyamoto of Chiba University and Dr. Saito of NICT for fruitful discussions. This work was partially supported by JSPS KAKENHI Grant Number 18H01908, 18K04967, and Tohoku University - NICT Matching.

References

[1] E. Linfield, "Terahertz applications - A source of fresh hope," Nat. Photon., vol. 1, pp. 257 – 258, 2007.

[2] M. A. Piestrup, R. N. Fleming, and R. H. Pantell, "Continuously tunable submillimeter wave source," Appl. Phys. Lett., vol. 26, pp. 418 – 421, 1975.

[3] S. Hayashi, K. Nawata, T. Taira, J. Shikata, K. Kawase, and H. Minamide, "Ultrabright continuously tunable terahertz-wave generation at room temperature," Scientific Reports, vol. 4, pp. 5045, 2014.

[4] S. Ohno, "Spectral drill: a geometrical phase shifter within a Fabry-Pérot cavity," OSA continium, vol. 1, pp. 136-143 2018.

Calibration of an Optical Electric-Field Probe at Frequencies Below 30 MHz Using a Shortened Monopole Antenna

Jerdvisanop CHAKAROTHAI*, Katsumi FUJII, Kanako WAKE, and Soichi WATANABE
National Institute of Information and Communications Technology
4-2-1, Nukui-Kitamachi, Koganei, Tokyo, 184-8795 Japan
*Corresponding author: jerd@nict.go.jp

Abstract – There is an increasing use of devices using electromagnetic fields at intermediate frequencies (300 Hz – 10 MHz) such as wireless power transfer (WPT) systems. In order to check their compliance against international standards to assure electromagnetic (EM) emission and human exposure levels, accurate measurements of EM field in the vicinity of the systems are required. In this study, we develop a calibration system for electric-field probes using a shortened monopole antenna as a standard field source, calibrate optical electric-field probes and compare their results with those obtained by using the TEM-cell method. Differences in the calibration factor derived by two different method of the standard field method and TEM-cell method was less than 2 dB for a frequency range from 10 kHz to 5 MHz.

Keywords – Monopole antenna; standard E-field method; optical E-field probe; probe calibration

1. Introduction

Recently, there are many devices using electromagnetic (EM) waves in the intermediate frequency range (300 Hz – 10 MHz) such as induction heating and wireless power transfer (WPT) systems. These devices are more and more frequently used at the place close to human body. Especially, WPT systems apply much higher power (up to few hundred kilowatts) than conventional communication devices and strong EM near-fields are created in the vicinity. Therefore, it is mandatory to make sure that these devices are compliant to the EMF limits prescribed in the international guidelines [1, 2]. In the guideline, basic restrictions are determined by specific absorption rate (SAR) in regard of thermal effect for frequencies above 100 kHz and induced electric field in regard of stimulus effect for those under 10 MHz. However, these physical quantities are difficult to measure in practice. Instead, reference levels of electric/magnetic fields are used for compliance and, thus, measurement of EM fields must be done accurately.

In order to measure electric fields, a well-calibrated probe must be used to obtain accurate results. For an E-field probe, there are many calibration methods such as transverse electromagnetic (TEM) cell method or parallel plate [3]. However, there are some drawbacks in applying these calibration methods. For example, in a TEM cell, not only electric field is created but also magnetic field. Placing a probe in a limited space inside the TEM cell can disturb EM field distribution which may increase uncertainty in the calibration. In addition, the space inside the TEM cell or parallel plate limits size of the probe to be calibrated.

In this paper, we use a shortened monopole antenna in the calibration of E-field probe in order to address the problem described above. We construct a calibration system and calibrate commercially available optical E-field probe.

2. Calibration Using Standard Field Method

Standard field method uses a certain EM field produced by an antenna in the calibration of a probe which is placed in a region where the EM field distribution is theoretically calculated. By measuring power flowing into the antenna, we can determine the electric field strength at a specific point from the theory. If a measured voltage at a probe terminal is denoted as V_i, then we can calculate the calibration factor as the following equation:

$$F_i = \frac{E_i}{V_i} \tag{1}$$

where the subscript i indicates one of three axes in orthogonal orientations. In case of rectangular coordinate system, $i = \{ x, y, z \}$.

Fig. 1 shows configuration of the calibration system using a shortened monopole antenna. A monopole antenna whose length l of the monopole element is much shorter than the wavelength is placed on a large metal ground plane. If we assume that the current distribution on the monopole is a piecewise sinusoidal waveform, an electric field strength at an observation point $O(\rho, z)$ can be calculated using antenna input power P_{in} as

$$|E_z(\rho,z)| \approx \frac{30\lambda}{\pi l}\left|\frac{1}{r_1}+\frac{1}{r_2} - \frac{2}{r_0}\right| \frac{\sqrt{Z_0 P_{in}}}{|Z_0+Z_a|}, \tag{2}$$

$$\left|E_\rho(\rho,z)\right| \approx \frac{30\lambda}{\pi\rho l}\left|\frac{z-l}{r_1}+\frac{z+l}{r_2} - \frac{2z}{r_0}\right| \frac{\sqrt{Z_0 P_{in}}}{|Z_0+Z_a|}, \tag{3}$$

where

$$r_0 = \sqrt{\rho^2+z^2}, r_1 = \sqrt{\rho^2+(z-l)^2},$$
$$r_2 = \sqrt{\rho^2+(z+l)^2}, \rho = \sqrt{x^2+y^2},$$

Z_0 is the intrinsic impedance of transmission line and Z_a (= R_a + j X_a) indicates input impedance of the antenna. When the element length is much small compared to the wavelength, the antenna input impedance can be approximated as [4]

$$Z_a \approx 10(kl)^2 - j\frac{60}{kl}\left(\ln\frac{l}{a}-1\right). \tag{4}$$

In order to match the radiation resistance of the monopole antenna, the effective length of the antenna is determined as

$$l_a \approx \frac{\lambda}{\pi}\tan\left(\frac{\pi l}{\lambda}\right) \tag{5}$$

and, from [6]-[8], the resistance value is represented in the term of $\tan(\pi l/\lambda)$ as

$$R_a \approx 40\left\{\frac{1-\cos kl}{\sin kl}\right\}^2 = 40\tan^2\left(\frac{kl}{2}\right) \tag{6}$$

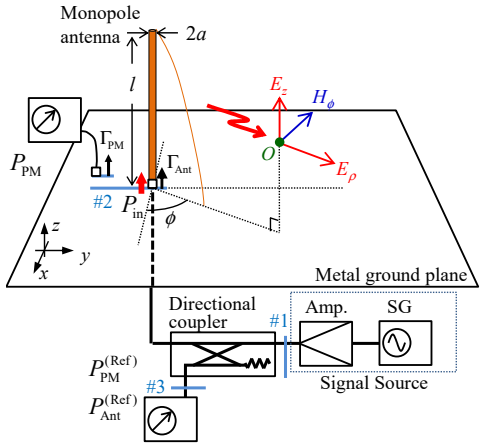

Figure 1. Standard electric-field method using shortened monopole antenna.

while (kl / tan kl) is added to the imaginary part to adjust the resonance frequency of the actual monopole antenna as

$$X_a \approx -\frac{60}{kl}\left(\ln\frac{l}{a}-1\right)\frac{kl}{\tan(kl)} = -\frac{60}{\tan(kl)}\left(\ln\frac{l}{a}-1\right). \tag{7}$$

Note that, theoretically, $|E_\phi(\rho,z)| = 0$, $|H_\rho(\rho,z)| = |H_z(\rho,z)| = 0$. In addition, when the antenna length is much smaller than wavelength, $|H_\phi(\rho,z)| = 0$. Therefore, magnetic field at the region close to the monopole antenna is small. Different from a TEM cell or parallel plate which will produce also magnetic field with a magnitude of $(120\pi)^{-1}$ times of electric field strength, the monopole antenna can provide nearly pure electric field distribution. If the antenna incident power is constant, the E-field created from the monopole antenna is also constant and independent on frequency. Using the electromotive force (EMF) method, when P_{in} = 1 W, we found that E_ρ and E_z are both constant for $l < 0.025\lambda$. For $l < 0.05\lambda$, an error in E-field strength using (2) and (3) is less than 5% [5].

For electric field distribution created by a shortened monopole antenna, there exists only E_z since E_ρ is nearly zero at the place close to the ground plane. As distance from the ground plane increases, E_ρ increases and become larger than E_z. If there exists a region where E_z is zero, then we can calibrate an E-field probe by using only E_ρ

component. From [5], we found that when the height is approximately $z = 0.6\lambda \sim 0.7\lambda$, E_z is almost zero. Therefore, we can calibrate a probe at this position.

3. Experimental Results

Firstly, we have constructed a calibration system using a shorted monopole antenna having a height of 2.5 m as shown in Fig. 1. The system includes signal generator (Keysight, 5080A), 50-dB amplifier (Bonn Elektronik), attenuator (Narda, 769-10), dual-directional coupler (Wellatone, C6422-10), power meter (Agilent, E4413A) and power sensor (Agilent, E9304A).

As described in the previous section, there exists a region that E_z is nearly zero and negligible compared to magnitude of E_ρ. Fig. 2 shows E_r distribution at the region close to monopole antenna (x = 0.2 – 1 m) at a frequency f = 100 kHz. From the result, we found that magnitude of E_z becomes minimum at a height of z = 1.4 – 1.65 m. The magnitude of E_ρ is larger 72 times of E_z and, hence, we can place a probe to be calibrated in this region.

Fig. 3 shows the calibration of a three-axis optical E-field probe (Seikogiken, SH-03EX) which is placed at x = 0.5 m, z = 1.6 m, where E_z is almost zero. In order to calibrate the probe, one of three receiving elements in the probe is aligned parallel to the ρ axis (or x-axis in the figure). The E-field probe is connected to optical controller (Seikogiken, C5-A11-1). Receiving optical signal is converted into electric signal and the received voltage is then measured at the 50 Ω terminator. Antenna incident power P_{inc} is set to 1 W. E-field strength is approximately 5.2 V/m for P_{inc} = 1 W.

Fig. 4 shows the result of calibration factor derived by using the standard field method with a shortened monopole antenna in a frequency range between 10 kHz and 10 MHz. Calibration factor determined by that using TEM cell is also shown in Fig. 4 as a solid black line. It is indicated that the calibration factors almost identical to each other except at the frequency higher than 3

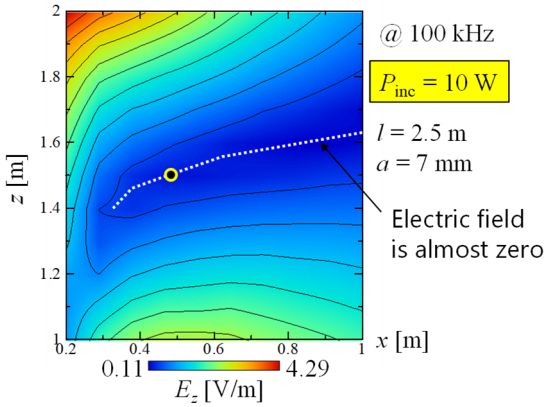

Figure 2. Electric field E_z distribution in a region close to the shortened monopole antenna.

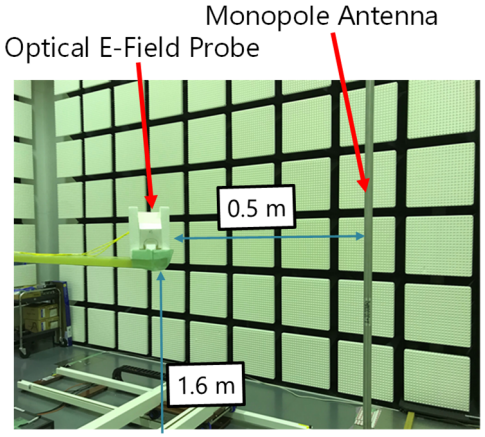

Figure 3. Calibration location of a three-axis optical E-field probe.

MHz where the calibration factor starts to deviate from the TEM-cell results. The reason is that magnitude of E-field deviates from that derived by theory when frequency increases

Fig. 5 indicates the error in calibration factor derived by using monopole antenna, compared with those of the TEM cell. Both results agree well each other and, hence, the validation of our method has been demonstrated. It was found that the error is less than 2 dB when f < 5 MHz and less than 1 dB when f < 3 MHz.

4. Conclusion

In this paper, we have constructed a calibration system for an optical E-field probe by using a shortened monopole antenna. It has been shown that there is a region where only ρ-component E-field exists while magnitude of E_z is nearly zero.

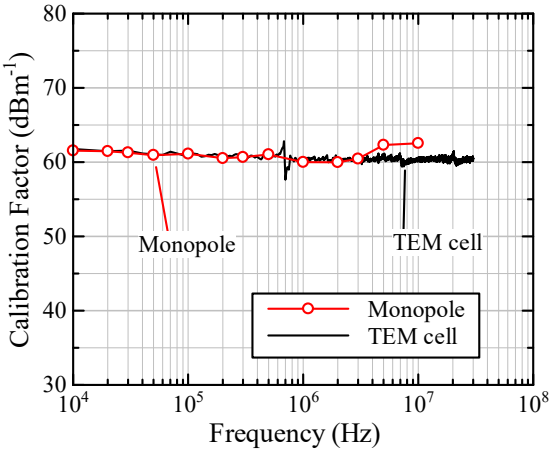

Figure 4. Calibration factor of a three-axis optical E-field probe (SH-03EX) combined with a controller (C5-A11-1).

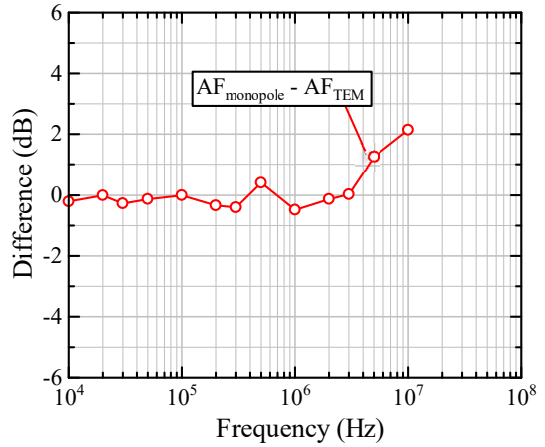

Figure 5. Difference in calibration factor derived by the proposed method and that by using TEM cell.

Magnetic near-field is apparent to be negligible and has no effect to the calibration results. A calibration was performed on a three-axis optical E-field probe (SH-03EX) and it was demonstrated that differences in the calibration factor derived by two different method of the standard field method using the monopole antenna and that using the TEM cell was less than 2 dB when $f < 5$ MHz and less than 1 dB when $f < 3$ MHz.

Acknowledgements

This study was supported by the Ministry of Internal Affairs and Communications, Japan. The authors would like to thank Dr. Ifong Wu (NICT) for measurement and calibration of a probe using TEM cell.

References

[1] ICNIRP, "Guidelines for limiting exposure to time-varying electric, magnetic, and electromagnetic fields (up to 300 GHz). International Commission on Non-Ionizing Radiation Protection," Health Phys, vol. 74, pp. 494-522, Apr 1998.

[2] ICNIRP, "Guidelines for limiting exposure to time-varying electric and magnetic fields (1 Hz to 100 kHz)," Health Phys, vol. 99, pp. 818-36, Dec 2010.

[3] IEEE, "IEEE Standard for Calibration of Electromagnetic Field Sensors and Probes, Excluding Antennas, from 9 kHz to 40 GHz," IEEE Std 1309-2005 (Revision of IEEE Std 1309-1996), pp. 1-115, 2005.

[4] S. Adachi, Electromagnetic Wave Engineering, Corona, 1983.

[5] Y. Iwatani, K. Fujii, K. Wake, J. Chakarothai, S. Watanabe, R. Suga, O. Hashimoto, "Preliminary Study on a Calibration System for E-field Probes using a Shortened Monopole Antenna," IEICE Technical Report, vol. 117, pp. 83-88, 2018.

[6] IEC/CISPR 16-1-6 Ed. 1:2017(b), Specification for radio disturbance and immunity measuring apparatus and method – Part 1-6: Radio disturbance and immunity measuring apparatus – EMC antenna calibration, p27, 2017.

[7] D. A. Knight, et al., "Comparison of calibration methods for monopole antennas, with some analysis of the capacitance substitution method," NPL Report, DEM-EM 005, p.4, 2004.

[8] K. Fujii, "An approximate equation of the input impedance for shortened monopole antenna," Proceeding of IEICE Society Conference, B-4-4, 2018.

Phase-Conjugated Signal Processing for Opto-Electronic Signal Measurements

Takahide SAKAMOTO[1*]
[1]Department of Electrical Engineering and Computer Science, Tokyo Metropolitan University,
6-6 Asahi-ga-oka, Hino, Tokyo, Japan, 191-0065

*Corresponding author: tsaka@tmu.ac.jp

Abstract – This paper presents phase-conjugated signal processing that is useful for remote signal sensing and measurements via. optical fiber links. For higher sensitivity and/or longer reach distance in the remote detection via. optical fiber links, it is important to increase optical signal power launched to optical fibers as high as possible. Optical signal transmission with high signal intensity, however, causes nonlinear waveform distortion due to fiber nonlinearity. In this paper, we investigate an opto-electronic signal processing technique that can effectively mitigate nonlinear waveform distortion in fiber links. Different from other approaches, the technique for fiber nonlinearity mitigation simply adopts opto-electric devices, like modulators and photodiodes, without relying on additional processing based on nonlinear optics, digital signals processing, and so on.

Keywords – phase-conjugated signal processing; optical remote sensing; fiber nonlinearity mitigation; optical modulation; optical detection

1. Introduction

Signal transfer and detection via. optical fiber links is a powerful way to remotely capture electric or optical signals. Digital or analog optical signals can be transmitted over fibers from/to remote places. By using microwave-photonic approaches, even high-frequency electrical signals, like millimeter or tera-hertz waves can be remotely transferred from/to remote places and efficiently detected.

For high-efficiency signal transfer and detection, we should increase optical power of the signals input to fiber links as high as possible. One issue is that such a high-power operation highly induces nonlinear signal distortion [1]. Self-phase modulation (SPM), cross-phase modulation (XPM), four-wave mixing (FWM) and stimulated Brillouin scattering (SBS) are dominantly observed in fibers and they cause nonlinear signal distortion. Among the nonlinear effects, FWM can be avoided when we use standard single-mode fibers (SMFs) as transmission lines and SBS can be suppressed with coherence control techniques. SPM and XPM are remained issues, which distort single- and multiple-wavelength signals, respectively. These days, fiber nonlinearity compensation is highly investigated, mostly focusing on signal equalization using digital signal processing. A good example is a back-propagation method, which enables cancellation of nonlinear signal distortion; however, it relies on heavy signal processing. Another direction is signal processing based on optical phase conjugation, which was firstly demonstrated by using optical conjugated signals generated by four-wave mixing in a fiber [2]. Phase-conjugated twin signal transmission has also been demonstrated [3], where phase conjugated twin signals are transmitted together for fiber nonlinearity cancellation. The former approach needs nonlinear fiber optics, the latter one requires digital signal processing for phase conjugation, respectively.

In this paper, we investigate opto-electronic signal processing for optical phase conjugation, introducing our work, called conjugated radio-over-fiber (C-RoF) system [4]. Through dual-sideband (DSB) modulation and detection, in the approach, optical phase conjugated signal processing is

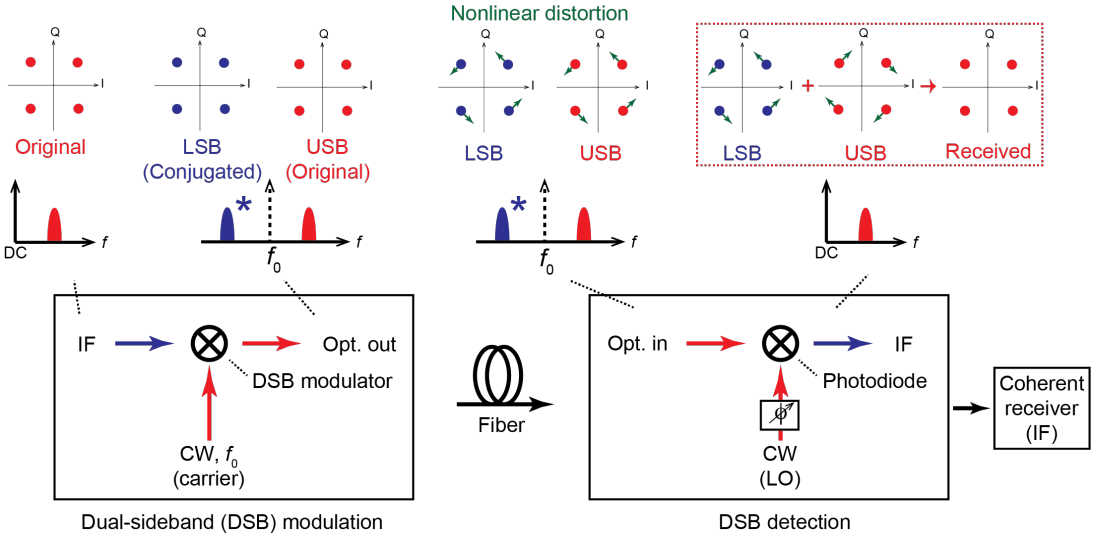

Figure 1. Principles of DSB processing for fiber nonlinearity mitigation

achieved and nonlinear signal distortion due to SPM and XPM is mitigated, without relying on heavy signal processing based on either DSP or nonlinear fiber optics.

2. Phase conjugated signal processing for fiber nonlinearity mitigation

Here, we discuss phase-conjugated signal processing based on dual-sideband modulation and detection, focusing on the technology called C-RoF [4]. We investigate fiber nonlinearity mitigation for SMF transmission of PSK signals.

Fig. 1 shows principle of C-RoF system based on dual-sideband modulation and detection. In the technology, a dual-sideband (DSB) modulated light is used to carry RF signals over optical fiber link, where the upper-sideband (USB) and lower-sideband (LSB) components of the modulated light both are transmitted over the fiber and SPM and XPM induced in the fiber cause nonlinear signal phase shifts. One thing is that both sideband components experience the same amount of nonlinear phase shift. Since the LSB component is phase conjugated against USB one, the nonlinear distortion will equivalently have the opposite sign against the distortion experienced by USB component. To receive C-RoF signals and achieve cancellation of such nonlinear distortion, their USB and LSB components are simultaneously down-converted in the dual-sideband detection. Through the down-conversion process, the sideband components are coherently superposed; the nonlinear signal distortions due to SPM and XPM are mitigated because the nonlinear distortions on USB and LSB components are cancelled each other.

Fig. 2 shows calculated constellations of QPSK signals transmitted over conventional RoF system. Detailed conditions are summarized in Appendix below. Plot (a) is the case for conventional RoF transmission, which is based on single-sideband up- and down-conversion. Plot (b) shows constellations of QPSK signal transmitted with C-RoF technique mentioned above.

The fiber nonlinearity mitigation is for fiber-optic transmission of digitally modulated signals; however, it would be useful for more general situation for transferring/detecting signals in remote places. The scheme will be advantageous especially in the situation, where the fiber links are unrepeated, *i.e.* no optical amplifiers are installed as repeaters. For example, the technology would improve sensitivity and reach distance of cost-sensitive fiber sensor networks with numbers of sensing elements.

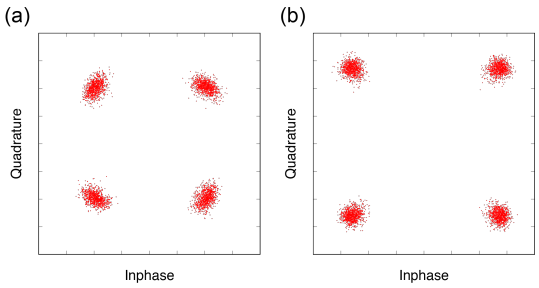

Figure 2. Received QPSK signals (calculated); (a) carried with SSB-RoF (conventional); (b) C-RoF

3. Conclusions

In this paper, we have investigated phase-conjugated signal processing based on dual-sideband modulation and detection. It has been shown that fiber nonlinearity can be mitigated by using the technique, which will be useful for remotely transferring/detecting signals over optical fiber links.

Appendix

Here, we summarize the conditions for the simulation mentioned above. The numerical simulation focuses on 1-Gbaud QPSK C-RoF signals. For DSB modulation, a push-pull Mach-Zehnder modulator (MZM) biased at the null point is used. With the modulator, 22.3-GHz subcarrier is data-modulated in the QPSK format at 1 Gbaud. The RoF signal is transmitted over standard single-mode fiber (SMF); fiber length (L) = 10 km; propagation loss (α) = 0.2 dB/km; nonlinearity coefficient (γ) = 2.6 $W^{-1}km^{-1}$; group-velocity dispersion (β_2) = -16 ps^2/km; launched power to the fiber (P) = 50 mW. The IF signal obtained with the dual-sideband detection is received with an PSK receiver based on digital signal processing for carrier-phase estimation to recover IQ data streams. OSNR (at 0.1 nm) of the generated C-RoF signal is set at 20 dB for the analysis.

References

[1] G.P.Agrawal, "Nonlinear Fiber Optics." Academic Press, 1995.

[2] S. Watanabe, M. Shirasaki, J. Lightwave Technol. 14, 243-248 (1996).

[3] X. Liu et al, Nature Photon. 7, 560-568 (2013)

[4] T. Sakamoto et al, Microwave Photonics 2014 (MWP2014), WD-6 (2014).